Investigation of Delayed Crack Propagation Associated with Hydrogen Effect in a Thin Sheet of Single-Crystalline BCC Iron-Based Alloy

ヒュン, タン, トウーン

Investigation of Delayed Crack Propagation Associated with Hydrogen Effect in a Thin Sheet of Single-Crystalline BCC Iron-Based Alloy

A dissertation submitted to

Graduate School of Engineering, Kyushu University, Japan

for the degree of Doctor of Philosophy in Hydrogen Energy System

Presented by

HUYNH THANH THUONG

August 2020

Contents

List of abbreviations

HE	Hydrogen embrittlement
HAC	Hydrogen-assisted cracking
HEDE	Hydrogen-enhanced decohesion
HELP	Hydrogen-enhanced localized plasticity
AIDE	Hydrogen-induced dislocation emission
CTOA	Crack tip opening angle
COD	Crack opening displacement
BCC	Body-centered cubic
FCC	Face-centered cubic
HCP	Hexagonal close-packed
SEM	Scanning electron microscope
TEM	Transmission electron microscopy
ECCI	Electron channeling contrast imaging
EBSD	Electron backscattering diffraction
GROD	Grain reference orientation deviation
KAM	Kernel average misorientation
IPF	Inverse pole figure
EDM	Electrical discharge machining
AFM	Atomic force microscopy

Nomenclature

τ_{nd}	Shear stress
σ	Applied tensile stress
σ_Y	Yielding strength
σ_{max}	Maximum stress
σ_{yy}	Normal stress in *y* direction
σ_h	Hydrostatic stress
θ	Angle between the tensile direction and the vector normal to the glide plane
γ	Angle between the tensile direction and the glide direction
K	Stress intensity factor
m	Schmid's factor
a	Crack length
$\mathrm{d}a/\mathrm{d}t$	Crack growth rate
P	Load
R	Stress ratio
r_p	Plastic zone size
C_H	Hydrogen concentration
B	The specimen thickness

CHAPTER 1. Introduction

1.1 Research background

1.1.1 Hydrogen in steels

Mechanical properties of metallic materials are typically degraded by hydrogen, and this phenomenon is the so-called Hydrogen Embrittlement (HE). HE can lower the strength and toughness of metallic alloys, such as those of iron [1], aluminum [2], tungsten [3], titanium [4] tantalum [5] niobium [6], nickel [7], molybdenum [8], zirconium [9], and uranium [10]. This can lead to unexpected failure in metallic structures. Hence, HE has been a serious problem for the design of structural materials in various industries, such as battleships, aircraft, nuclear reactors, etc. HE has been studied for many decades; however, researchers have yet to fully understand its nature despite several theories that have been proposed. Absolutely, further study of hydrogen behavior in metallic materials is required to establish principles for materials design and usage against hydrogen problems.

1.1.2 Hydrogen embrittlement mechanisms

Despite extensive study, the mechanisms of HE have remained unclear. Several candidate mechanisms have evolved, each of which is supported by experimental observations and simulations. When hydride phases are not involved, the most likely mechanisms of HE in steel have been proposed as follows.

1.1.2.1 Hydrogen-enhanced decohesion (HEDE)

The decohesion theory was first proposed by Pfeil [11], who suggested that hydrogen decreased cohesion across the cleavage planes and grain boundary. Thereafter, it was developed by Troiano [12], Oriani [13], and the others [14-18]. They suggested that hydrogen weakens the interatomic bonds so that tensile separation of atoms occurred in preference to slip.

Moreover, the activity of dislocation may accompany decohesion, and may lead to locally increase stresses at decohesion sites; however, dislocation activity should be fairly limited in order to maintain a sharp crack tip. The decohesion site is speculated that it occurs at the region of high concentration of hydrogen; such as at the sharp crack tip due to adsorbed hydrogen, several tens of nanometers ahead of the crack tip where dislocation emission creases maximum tensile stress, region of maximum hydrostatic stress, or particle-matrix interfaces ahead of cracks [19]. On the other hand, very high stresses are probably required to produce sufficiently high hydrogen concentrations in interstitial lattice sites ahead of crack tips to dominate decohesion. Such stresses can be reached a critical value to produce decohesion due to strain-gradient hardening [14, 15]. Also, decohesion could occur at grain boundaries ahead of the crack tip due to hydrogen trapped at specific sites, in which hydrogen caused bond weakening.

1.1.2.2 Hydrogen-enhanced localized plasticity (HELP)

HELP was first suggested by Beachem [20], who indicated that solute hydrogen facilitated the movement of dislocations. Subsequently, this mechanism was

promoted by Birnbaum [21], Sofronis [22], and Robertson [23]. They proposed that solute hydrogen accumulates locally in regions near crack tips, where the hydrostatic stress acts and within the entry of hydrogen at the crack tip. Deformation was localized in these regions due to the ability of hydrogen that promotes dislocation motion.

Crack growth associated with HELP is envisaged to occur by micro-void coalescence process. Still, the distribution of microvoid is more localized than that which would arise in an inert environment. Hence, fracture behavior promoted by HELP is associated with ductile rather than brittle fracture. Also, intergranular, transgranular, and/or quasi-cleavage fracture may be activated depending on microstructure, crack-tip stress intensity, and hydrogen concentration [20].

1.1.2.3 Absorption-induced dislocation emission (AIDE)

Lynch proposed the AIDE mechanism [24] and subsequently developed [25-27]. AIDE mechanism is briefly summarized as follows: (i) adsorbed hydrogen at the crack tip surfaces weaken interatomic bonds of atoms over several atomic distances, this combined with high stress at the crack tip facilitates dislocation nucleation from the crack tip. This nucleation stage involves the simultaneous formation of a dislocation core and surface step by shearing the interatomic bonds; (ii) subsequently, nucleated dislocations can readily move away from the crack tip under applied stress.

However, in the AIDE model, crack growth from the crack tip under sustained or monotonically increasing applied loads not only involves dislocation emission but also is contributed by nucleation and growth of microvoids and/or nano-voids ahead of crack tips. Regarding nucleation and growth of voids, the stresses required for

dislocation emission are sufficiently high to facilitates general dislocation activities ahead of the crack tip. Hence, voids can nucleate and grow at the second-phase particles, interaction between slip bands, or other sites within the plastic zone ahead of the crack tip. When crack growth by dislocation emission at the crack tip associated with void nucleation and growth ahead of the crack tip, the coalescence of cracks with voids occurs at lower strains, and shallower dimples are produced on fracture surfaces. Void generation contributes to causing further cack growth; however, the crack growth primarily occurs by dislocation emission (alternate slips) from the crack tip. Also, the growth and coalescence of voids ahead of the crack tip serve to resharpen the crack tip and result in a small cack-tip-opening angle (CTOA).

1.1.3 Slip characteristics of single crystal

Single crystals play a considerable role in presenting a clearer picture of a material's intrinsic properties. Scientists want to reduce many variables as possible to understand a material's properties. A primary way to do this is to begin with a single crystal that has free boundary effects. Notably, in order to best understand mechanisms of hydrogen embrittlement, using metallic single-crystalline materials is a priority. However, in single-crystalline materials, the physical and mechanical properties often differ with orientation, and it is hence anisotropic.

When a single crystal is subjected to tensile stress, it is deformed. If shear stress reaches a critical value, which is the so-called critical resolved shear stress, plastic deformation by slips will occur. Slips occur on well-defined parallel crystal planes, and sections of a single crystal slide relative to one another, which results in changing the geometry, as shown in Fig 1.1(a). Slip always occurs on a particular

crystallographic plane *(slip plane)*; slip always takes place along consistent directions within slip planes *(slip directions)*, as shown in Fig. 1.1(b). These are crystallographic planes and directions that are characteristic of the crystal structure. The shear stress can be expressed as [28].

$$\tau_{\mathrm{nd}} = \sigma . \cos\theta . \cos\gamma \qquad (1.1)$$

Where, τ_{nd} is shear stress (the subscripts n and d refer to the slip plane normal and the direction of slip, respectively), σ is applied tensile stress, θ is an angle between the tensile direction and the vector normal to the glide plane, and θ is an angle between the tensile direction and the glide direction. The value of $\cos\theta . \cos\gamma$ is typically termed the Schimd factor (m). Depending on the type of lattice of materials, such as face-centered cubic (FCC), body-centered cubic (BCC), and hexagonal close-packed crystal (HCP), different slip systems are present. Specifically, slip occurs on close-packed planes and in close-packed directions. The close-packed planes contain the highest number of atoms per area, while close-packed directions are the crystallographic directions with the shortest distance between atoms. A slip plane and a slip direction constitute a slip system in single-crystalline materials. Slip planes and directions for several common crystals are summarized as follows [28]:

In FCC structure, which is also common among the metals, and is shown Fig. 1.2(a). The slip plane is $\{111\}$ types, and the slip direction is of type $\langle 110 \rangle$. Given the permutations of the slip plane types and slip direction types, FCC crystals have 12 slip systems.

In BCC structure, which is exhibited by many metals, and is shown in Fig. 1.2(b). BCC structure can contain up to 48 slip systems. There are six slip planes of type $\{110\}$; each of them has two types of $\langle 111\rangle$ directions. Total slips of type $\{110\}\langle 111\rangle$ contain 12 slip systems. There are 12 types of $\{112\}$ planes and 24 types of (123) planes, in which each of them has one type of $\langle 111\rangle$ direction. Total slips of type $\{112\}\langle 111\rangle$ and $\{123\}\langle 111\rangle$ contain 36 slip systems.

In the HCP structure, which is also common in metals. It is more complex than the cubic structures but can be described very simply concerning the stacking sequence. The cell structure of the HCP crystal is shown in Fig. 1.2(c). It is much more limited slip systems than those of BCC and FCC crystal structures. HCP crystal structures usually allow slip on the densely packed basal $\{0001\}$ planes along with the $[11\bar{2}0]$ directions, which are the so-called Basal slips. Also, the other slip systems in HCP are Pyramidal slips $\{0001\}\langle 11\bar{2}3\rangle$ and Prismatic slips $\{10\bar{1}0\}\langle 11\bar{2}0\rangle$ [29].

1.1.4 Ductile crack propagation

In the ductile crack propagation, crack propagation is associated with micro-void initiation, growth, and coalescence. When a steel structure contained a crack is subjected to the load, stresses, and strains around the crack tip become sufficient to nucleate voids. Voids grow as the crack blunts, and these voids coalescence each other and connect to the main crack. These processes repeated and result in crack propagation. Fig. 1.3 schematically illustrates these processes, which are nucleation of micro-voids, void growth, and coalescence. Regarding void nucleation, a void can form around a second-phase particle [30] or inclusions [31] when stresses are sufficient

to break the interfacial bonds between the particle and the matrix. On the other hand, void nucleation by stress has been reported [32, 33], or the other studies [34, 35] presented that void nucleated by dislocation-particle interactions. Once voids nucleate, one proposed that voids can grow by both further plastic strain and a high-stress triaxiality around the crack tip [36]. Subsequently, voids coalescence and connect to the main crack. In finite element analysis [37], the strain is singularity near the blunting crack tip, while the peak of crack tip stress presents approximately twice of the crack-tip opening displacement, as shown in Fig. 1.4.

Ductile crack propagation represented by void growth and coalescence typically absorbs more energy and results in stable crack propagation. When crack propagation associated with void growth and coalescence, the crack exhibits tunneling effects. In detail, the crack propagates faster in the central regions, while it lags behind near the side regions. The stress tri-axiality varies across the thickness direction, in which higher stress tri-axiality acts in the specimen interior and leads to propagating crack faster. Near the side surface, due to lower stress tri-axiality, the maximum shear stress lies on a plane at 45° to the tensile direction and the thickness direction. It produces a shear fracture on a plane that accommodates the maximum shear stress, as shown in Fig. 1.5 [36]. In Fig. 1.5, the appearance of a flat fracture surface at the central region is due to the high-stress tri-axiality; however, a closer observation reveals a complex structure. For instance, in a cracked specimen subjected to a Mode I loading, plane strain predominates in the specimen interior, and the maximum plastic strain occurs at 45º from the crack plane, as shown in Fig. 1.6(a). On the other hand, in order to accommodate a flat fracture surface and to reconcile the mechanical

competition at the crack tip, the crack propagates in a zigzag pattern, as shown in Fig. 1.6(b) [36], and as an evidence of zigzag pattern shown in Fig. 1.7 [37].

1.1.5 Distribution of hydrogen at the crack tip

In HE, one of the crucial aspects is that there exists a transport stage of hydrogen to the sites where degradation occurs. Many studies about this issue have been performed; the results are shown as follows.

Hydrogen distribution around a crack tip was initially proposed by Trotriano and coworkers [38]. They suggested that long-range diffusion and of hydrogen to the triaxial stress field developed ahead of a stressed crack. Hydrogen was then concentrated in the highest triaxial stress field, and this concentration was developed by the stress-induced segregation that leaded void formation [39] or reduction of the cohesive strength of the material bond [40]. In the later, Doig et al. [41] and Yokobori et al. [42] developed a model for hydrogen-induced cracking at notches with assuming a perfectly elastic-plastic material and suggested that hydrogen concentrated at the field of highest hydrostatic stress ahead of the crack tip. These concepts were based on stress assisted diffusion and were analyzed in small scale yielding.

Moreover, Gerberich et al. [43] proposed a model simulated dislocation emission from the crack tip to calculate the crack tip stress redistribution. They showed that dislocation emission not only shields the crack tip but also reduces the local maximum stress to slightly below the theoretical fracture stress and move the site of maximum stress triaxiality to closer to the crack tip. Consequently, hydrogen hence concentrates on the site of newly maximum stress tri-axiality. Recently, Paneda et al.

[44] used a new model that is hardening due to geometrically necessary dislocations by means of strain gradient plasticity to simulate the hydrogen diffusion to the fracture process zone. They also suggested that the maximum stress tri-axiality acts ahead of the crack tip, and hydrogen then accumulates to this site of maximum stress tri-axiality.

On the other hand, in conjunction with large deformation elastic-plastic behavior in the vicinity of a blunting crack tip, Softonic et al. [45] showed that hydrogen accumulates mainly in traps near the crack surface during plastic straining. The hydrogen concentration at regular interstitial lattice sites was only mildly elevated at the peak of hydrostatic stress ahead of the crack tip. The high concentrated hydrogen fields were determined predominantly by the plastic strain, which generated traps site. Hence, the role of stress tri-axiality in determining the hydrogen accumulation site was not as important as the role of crack tip plastic strain.

The above studies relate to lattice diffusion toward the crack tip. However, in the absorption of hydrogen at the crack tip surfaces, Lynch et al. [46] suggested that adsorbed hydrogen at the crack tip surfaces plays a major role for HE. In detail, the absorbed hydrogen weakens interatomic bonds of atoms over several atomic distances, this combined with the crack tip stress facilitates dislocation nucleation from the crack tip. The nucleated dislocations can readily move away from the crack tip under applied stress. This hypothesis was known as the AIDE mechanism.

1.1.6 Hydrogen embrittlement in single-crystalline Fe-Si alloy

1.1.6.1 Single-crystalline iron-silicon alloy

In order to investigate the mechanism of crack growth in an air environment or crack growth associated with HE, single-crystalline alloys are typically preferred due to it exhibits free from the potential effect of the grain boundary and non-hydride formation. Especially, the single-crystalline Fe-Si alloys are widely used due to it has the properties that necessary to serve various research purposes, such as brittle-ductile transition [47], and deformation twin [48]. Also, this material has been used to study the mechanisms of stable crack propagation associated with HE [49], delayed crack propagation [50-52], and hydrogen effect on slip behavior during the fatigue crack growth [53, 54].

Owing to this material is a single crystal, the physical and mechanical properties often differ with orientation, and it is hence anisotropic. The fracture toughness is varied with different crystal orientations. The crystal structure of Fe-Si alloy is BCC; it thus exhibits ductile properties due to it has a number of slip systems. In detail, the results of the studies [55-57] of slip planes in this material are reported that slip occurs on several types of $\{110\}\langle 111\rangle$, $\{112\}\langle 111\rangle$, and $\{123\}\langle 111\rangle$ slips. However, the ductility of this material depends on the content of silicon [58, 59]. Depend on tested conditions, environments, temperature, etc., different active slip systems that contributed to crack propagation were reported. Specifically, HE is due to cleavage fracture along a $\{100\}$ plane [60], HE cracks were initiated on $\{110\}$ slip plane, and the orientation of cracks initiated from inner defects was also on $\{110\}$ slip planes using a smooth specimen [61]. Moreover, the single-crystalline Fe-3%Si alloy

exhibits high strength and ductility; hence it is widely used to conduct tests to investigate delayed crack propagation [16, 50, 51] and hydrogen effect on slip behavior around the fatigue crack tip [62].

1.1.6.2 Hydrogen embrittlement in single-crystalline Fe-Si alloy

In the early 1980s, the crack propagation associated with hydrogen embrittlement was carried out in Fe-2.6%Si single crystal [63]. The authors reported that plasticity might be responsible for the stable quasi-brittle crack propagation. Also, Fe-2.6%Si single crystal was used to exam the crack tip opening angle (CTOA) during the stable crack growth as a function of hydrogen pressure, temperature, and rate. CTOA was used to characterize hydrogen embrittlement [64]. The results showed that CTOA depended on the temperature and rate, in which CTOA decreases with decreasing rate at low temperature, CTOA increases with decreasing rate at high temperature. The other studies [25, 65, 66] revealed that HE at a crack tip could promote the multiplication of dislocations and nucleation of a critical cleavage crack. Moreover, HE in Fe-3%Si single crystal under Mode II loading was studied, the results suggested that hydrogen-induced cleavage fracture can occur. Also, the normalized threshold stress intensity factor for HE during dynamic charging has a minimum value when the tensile loading axis is along the [001] or [110] direction, but a maximum value when the tensile loading axis is near [111].

In the later, Gerberich et al. [50, 51, 67, 68] conducted the HE in Fe-3%Si single crystal under sustained load that the remote stress far below the yielding strength. Discontinuous brittle crack growth was observed, and during crack growth left striation on the fracture surface. This brittle crack growth was detected by acoustic

emission. Furthermore, they proposed a model of subcritical crack growth, which is shown in Fig. 1.8. The brittle crack growth was described as follows: (1) A stress field with maximum stress at about 20nm ahead of the crack tip is formed by the interaction between the crack tip, the applied stress, and dislocations; (2) hydrogen diffused to the maximum tri-axial stress field ahead of the crack tip; (3) when the hydrogen concentration reaches a critical value, micro-crack is nucleated at hydrogen-enriched regions; (4) the micro-crack connects to the main crack and leads to crack growth. These four processes repeat, resulting in discontinuous crack growth. Another study of these authors [69] investigated the crack tip strain distribution under plane stress and planes train conditions, which is shown in Fig. 1.9. They suggested that the discontinuous crack growth available in local sub-structure feature was contributed by the high potential of plasticity. Also, strong plane stress versus plane strain effects for stable crack growth associated with HE.

Recently, Hajilou et al. [70] used an in situ electrochemical set-ups in combination with a nano-indentation system to perform bending tests on single and bi-crystalline Fe–3%Si alloy micro-cantilevers electrochemically charged with hydrogen. HE crack growth was by triggering crack initiation and propagation at the notch where stress concentration is existing. A transition from transgranular fracture to intergranular fracture mechanism that highly depends on the position of the stress concentration relative to the grain boundary was also reported.

1.2 Objectives

Understand material failure mechanisms is a field of great interest for industrial and engineering applications. Most metallic materials always contain geometric discontinuities, which are crack-like defects. However, cracks may initiate early in service life. The crack then propagates and reaches a critical length for satisfying unstable fracture, which leads to sudden failure in steel structures. Furthermore, material failure mechanisms associated with HE are the most concern for material engineering. Especially, under the sustained load that the remote stress is well below the yielding strength, the crack is supposed that it does not propagate in the air environment [51]. However, the crack will propagate in a hydrogen environment [17, 51, 67, 68]. This shows a strong effect of HE, and this type of fracture is typically termed as a delayed fracture. On the other hand, most of the previous studies, particularly those related to experiment analyses, were conducted with specimens which are relatively large thickness. In fracture mechanics research, due to highly constrain in a thickness direction of thick specimens, plane strain conditions exist in the specimen interior and ahead of the crack tip. Significantly reducing the specimen thickness can decrease the stress tri-axiality ahead of the crack tip, then results in the increases of crack tip plastic strain, and crack growth resistance hence increases as well [36]. Also, HE process is typically predominated under plane strain conditions where the highest stress tri-axiality exhibits ahead of the crack tip [50, 71]. Hence, significant reducing specimen thickness thereby reduces the amount of hydrogen enrichment near the crack tip, which results in the increase in HE resistance. Takahashi et al. [52] conducted a delayed crack propagation using a relatively thin sheet of single-

crystalline Fe-Si alloy and found that despite significantly reducing the constraint in the thickness direction, the crack growth mode in a thin specimen was the same as in that of thick specimens. Especially, some particularly new findings were reported: (1) the crack opening displacement (COD) 200 μm behind the crack tip and the unit distance of crack advancement are independent of both the crack length and the crack propagation rate, (2) the crack tip plastic zone size linearly increases with the crack length, (3) the crack propagation rate monotonically increases with the crack tip plastic zone. These findings suggested that the plastic deformation around the crack tip affects the rate-limiting process. Again, this shows a strong effect of HE. Hence, understand well the delayed crack propagation mechanisms are not only a challenge but also a motivation of researchers.

On the other hand, common metallic materials are polycrystalline structure. Thus, grain boundary causes some difficulties in order to clarify the crack propagation mechanism. Related to HE, in some metallic materials, the formation of hydride is also an obstacle to investigating HE mechanism. Hence, using a single-crystalline Fe-Si alloy is suitable, in which this material has a relatively high yield strength and exhibits free from the potential effect of grain boundary as well as hydride formation.

Consequently, the key objective of the present dissertation is to investigate characteristics of crack propagation in a hydrogen environment under the sustained load and in an air environment under monotonic load using a thin specimen of single-crystalline Fe-Si alloy based on practical issues in order to contribute to further understand the crack propagation and the nature of HE.

1.3 Thesis outline

This work included five chapters. The order of chapters is streamlined in order to clarify the objectives as well as the results of this research. The dissertation is structured as follows:

In Chapter 1, a general introduction is described. Several mechanisms of HE have been reviewed, and ductile crack propagation has been described. Also, characteristic and the use of single-crystalline materials was briefly discussed. Distribution of hydrogen at the crack tip and hydrogen sources were also pointed out. Finally, the motivations and goals of this work have been exposed.

In Chapter 2, characteristics of ductile crack propagation of a center-cracked tension specimen in a hydrogen environment are investigated. A center-cracked specimen is subjected to sustained load in a hydrogen atmosphere at room temperature. Hydrogen-induced delayed crack propagation is observed. Crack propagates discontinuously accompany extensive plasticity. The results show that the crack tip plastic deformation associated with the effect of hydrogen during the crack propagation leaves three adjacent regions where different plastic strain gradients and dislocation densities are observed. A model demonstrated the mechanism of hydrogen-induced crack propagation is proposed. These findings revealed the effects of plastic deformation and hydrogen-dislocations interaction around the crack tip on the rate-limiting process of hydrogen-induced delayed crack propagation in thin specimens.

In Chapter 3, effects of hydrogen on macroscopic and microscopic features of crack propagation are investigated. The center-cracked specimens are tested under

a sustained load in a hydrogen environment while under continuous stretching in an air environment. A comparison between these features is made to elucidate the role of hydrogen on the hydrogen-induced delayed crack propagation. The results show that despite significantly reducing the specimen thickness, the crack growth mode of a thin specimen is the same as that in thick specimens. The crack propagation accompanies extensive plasticity. Surprisingly, the crack propagation process was identical irrespective of test environments and consists of three stages: (1) crack tip blunting by dislocation emission from the crack tip; (2) void/shear crack initiation ahead of the crack tip; (3) sub-crack initiation and opening process. The similarity was also observed in the deformation microstructures beneath the fracture surface. Both microstructures were composed of three distinct layers characterized by plastic strain gradients and dislocation densities. However, the characteristics of plastic strain and strain gradient in these regions are different. Three layers were significantly affected by the environment, in which AIDE and HELP mechanisms are believed to be relevant. Also, reverse plastic strain in the regions behind the fracture surface due to unloading was observed, which contributes to not only enlarge CTOA but also blunt the crack tip.

In Chapter 4, as mentioned above, the crack propagation is discontinuous and leaves striation on the fracture surfaces in both air and hydrogen. This chapter investigates the characterization of striations and slips traces of specimens presented in the above two Chapters. Besides, a crack tip plastic deformation at a stationary crack and short crack propagation are investigated by ECCI and EBSD. SEM fractography is also aided. The possible mechanism of discontinuous crack propagation, as well as constant striation spacing, is discussed. The results explicitly revealed that the

microscopic mechanism of hydrogen-induced delayed crack propagation is one of the probable mechanisms for ductile crack propagation in the present crystal orientation and material. Striation is formed by extensive slips emitted from the crack tip, which are mainly contribution of specific $(1\bar{1}2)[\bar{1}11]$ and $(\bar{1}12)[\bar{1}1\bar{1}]$ slip systems. Discontinuous crack propagation is mainly caused by the interaction of the crack and $(1\bar{1}2)[\bar{1}11]$ and $(\bar{1}12)[\bar{1}1\bar{1}]$ slip bands/dislocation cells formed ahead of the crack tip. These slip bands/dislocation cells are characterized that the spacing between them is constant and independent of crack length. Hence, striation spacing is obviously the same as that of slip bands ahead of the crack tip.

In chapter 5, conclusions and future work are presented.

1.4 List of published paper during Ph.D. period

[1]. Thanh Thuong Huynh, Motomichi Koyama, Yoshimasa Takahashi, Shigeru Hamada, Kaneaki Tsuzaki, Hiroshi Noguchi, *Plastic deformation sequence and strain gradient characteristics of hydrogen-induced delayed crack propagation in single-crystalline Fe–Si alloy*, Scripta Materialia 178 (2020) 99-103.

1.5 Figures

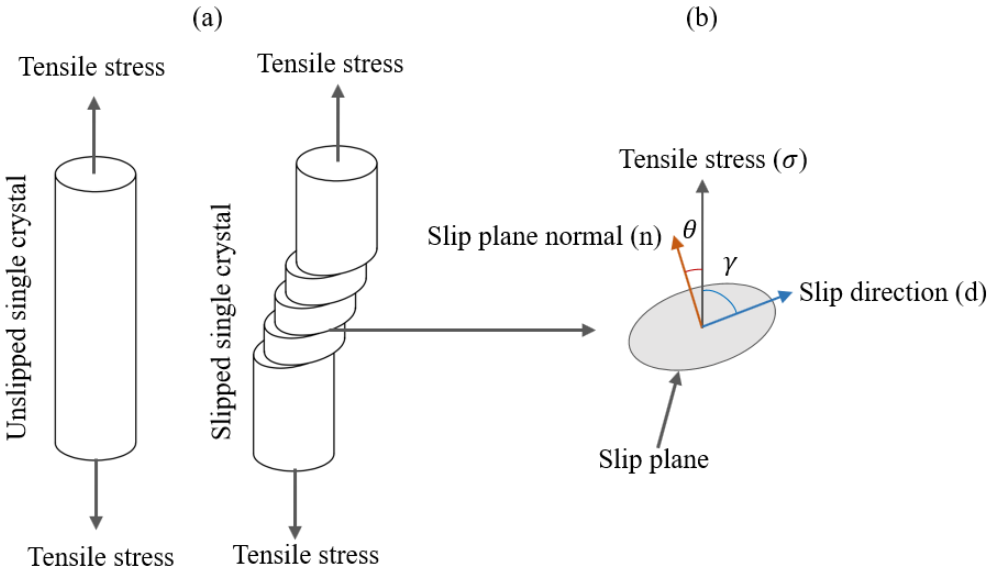

Fig. 1. 1. (a) Slip by shear between parallel planes of atoms; (b) Slip plane and slip direction

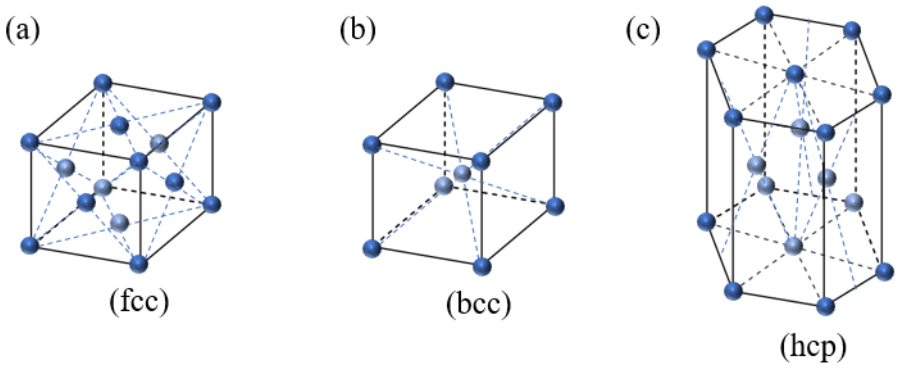

Fig. 1. 2. Several common crystals, (a) face-centered cubic, (b) body-centered cubic, (c) hexagonal close-packed crystal

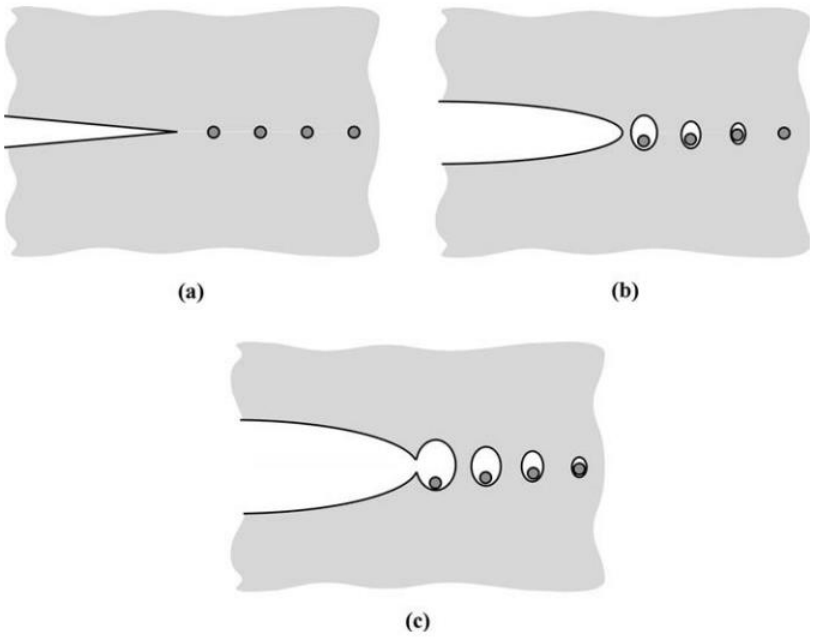

Fig. 1. 3. Mechanism of ductile crack propagation, (a) nucleation of micro-voids, (b) void growth, (c) void coalescence, and connect to main crack [36].

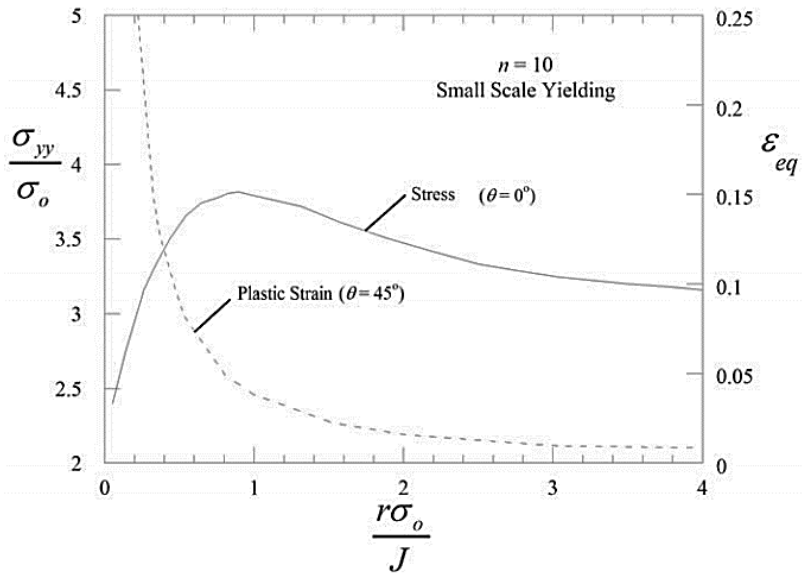

Fig. 1. 4. Stress and strain ahead of a blunted crack tip, determined by finite element analysis [37].

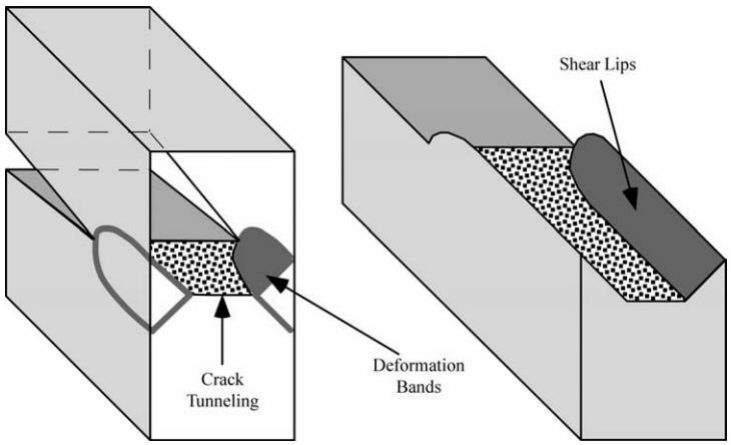

Fig. 1. 5. Ductile crack propagation of an edge crack. Shear fracture accommodates the maximum shear stress near the side surface [36].

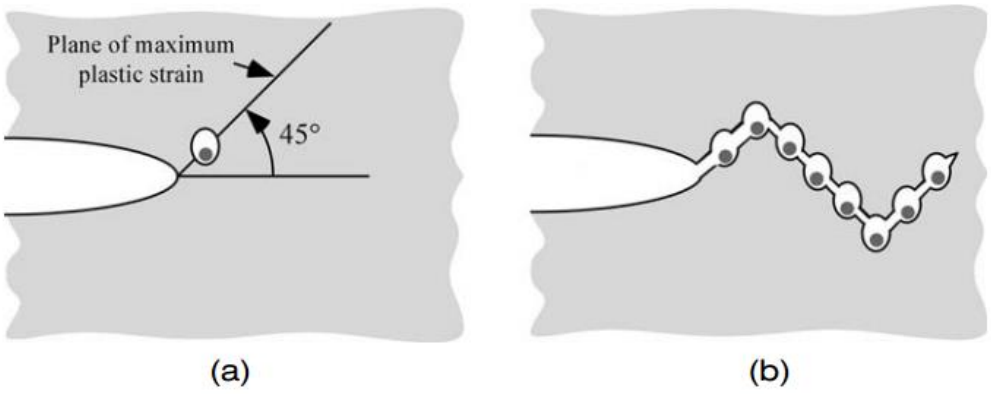

Fig. 1. 6. (a) Plane of maximum plastic strain under plane strain conditions, (b) Ductile crack propagation in zigzag pattern in plane strain conditions [36].

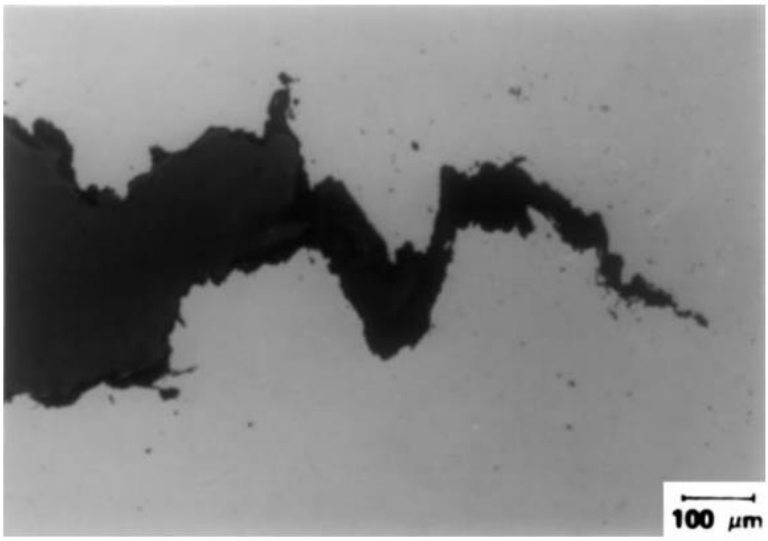

Fig. 1. 7. Optical micrograph of ductile crack propagation in an A 710 high-strength low-alloy steel showing a zigzag pattern [36].

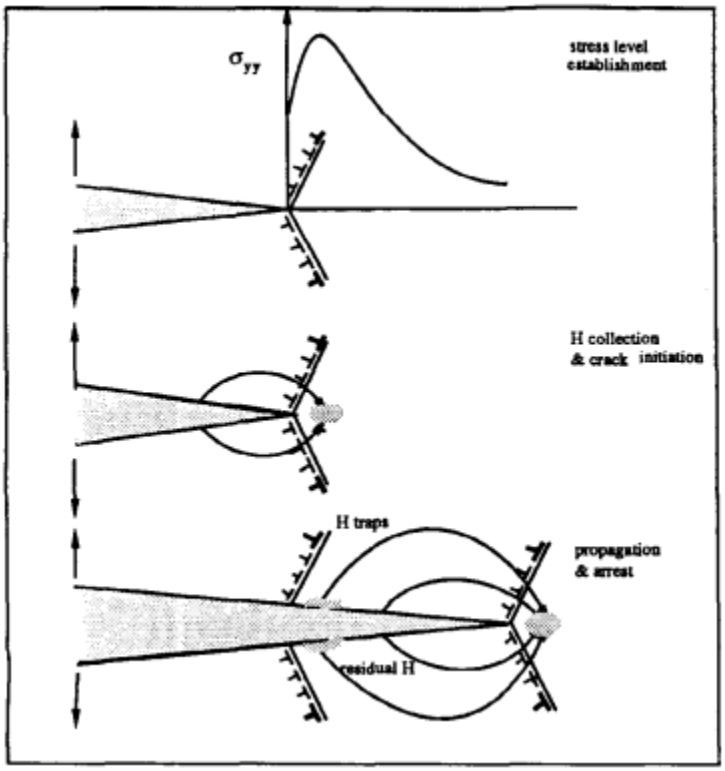

Fig. 1. 8. Schematic of hypothesized HE event sequence in Fe-3%Si single crystals [51].

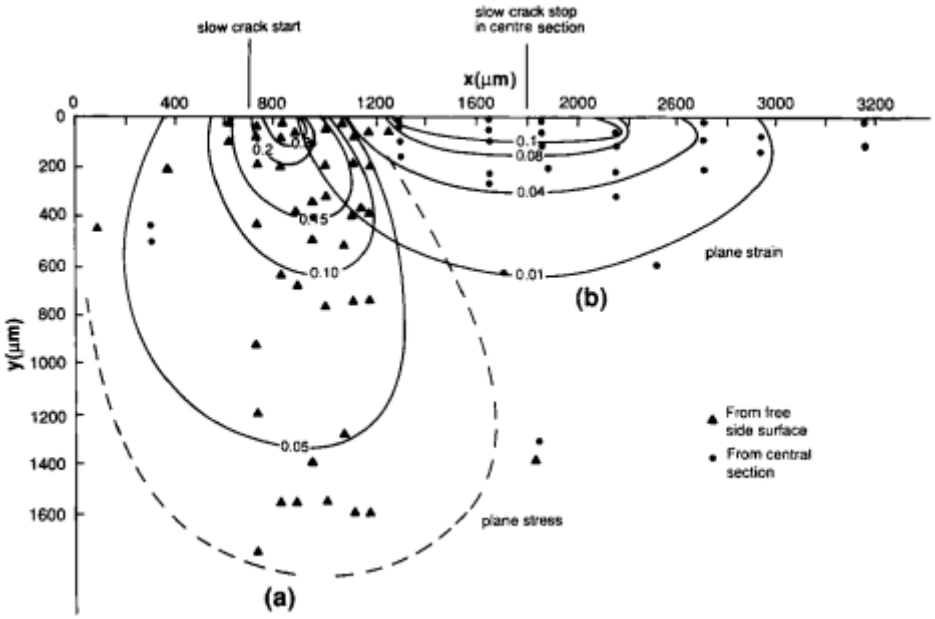

Fig. 1. 9. Strain distribution about a stable crack growth. (a) Strain distribution at the free side surface. (b) Strain distribution at the mid-section [69].

CHAPTER 2. Dislocation Observation in Delayed Crack Propagation in Hydrogen Environment

2.1 Introduction

Metals are susceptible to delayed fracture under a constant load associated with hydrogen effects, which can lead to unexpected failure. To avoid this, structural design should consider the time-dependent stress/strain state of metallic materials. However, before quantitative structural design can be attained to avoid it, we must first clarify the underlying mechanism of delayed fracture. The key to understanding the delayed fracture mechanism is in the effect of diffusible hydrogen on the plastic deformation near a crack tip.

The macroscopic behavior of hydrogen-assisted cracking (HAC) for instance the effect of diffusible hydrogen on the plastic deformation near a crack tip has been investigated previously. Several models have been proposed to understand HAC. In the kinetic model, hydrogen diffusion and accumulation dominate the HAC process [41, 49, 51]. Another model suggests that the specific dislocation structure at the crack tip is the defining factor [72-74]. However, all of the previous studies were performed with thick specimens; thus, HAC would have occurred predominantly under plane strain conditions [50, 71]. Reducing the specimen thickness can decrease the stress tri-axiality ahead of the crack tip, and thereby not only increase local plastic strain but

also reduce the amount of hydrogen enrichment near the crack tip, which affects on the HAC process.

Takahashi et al. [52] performed hydrogen-assisted delayed crack propagation in a thin sheet of the single-crystalline Fe-Si alloy and found that in spite of significantly reducing the constraint in the thickness direction the crack growth mode in a thin specimen was the same as in that of thick specimens. Especially, some particularly new findings were reported: (1) the crack opening displacement (COD) 200 μm behind the crack tip, and the unit distance of crack advancement are independent of both the crack length and the crack propagation rate (da/dt), (2) the crack tip plastic zone size linearly increases with the crack length, (3) log (da/dt) linearly increases with the crack tip plastic zone. These findings suggested that the plastic deformation around the crack tip affects the rate-limiting process. Therefore, modeling the HAC process in thin sheet specimens is necessary. However, before the HAC process can be modeled, the microscopic features of HAC in thin sheet specimens need to be analyzed in detail. Hence, in this study, the microscopic aspects of hydrogen-induced delayed crack propagation will be investigated. In particular, the plastic deformation sequence, strain gradient, and characteristic of dislocations underneath the fracture surface in the thin sheet of the single-crystalline Fe-3wt%Si alloy are focused.

2.2 Experimental procedure

To investigate fractography, slip traces on the specimen side surfaces, dislocation structure, and plastic strain distribution underneath the fracture surfaces,

this study analyses of a broken specimen in hydrogen, which was presented by Takahashi et al. [52], were performed again. However, the experiment procedures are briefly summarized as follows. The examined material was a sheet of a single-crystalline Fe-3wt%Si alloy with a (110) surface and gauge dimensions of 90 × 30 × 0.18 mm. The yield strength (σ_Y) of this material in the [001] direction was measured as 290 MPa. A through-notch was introduced along the $[\bar{1}10]$ direction at the center of the specimen. A fatigue pre-crack with a length of $2a$ = 2270 μm then was introduced on the (001) plane from the notch root. The specimen geometry and crystallographic orientation are shown in Fig. 2.1. The specimen was subjected to a sustained load of P = 1339 N under a hydrogen atmosphere (580 kPa) at room temperature by using an electro-hydraulic testing machine. The crack length was observed by a CCD microscope through a chamber window.

The topologies of the fracture surface and side of the specimen were observed by field emission scanning electron microscopy (SEM) at an accelerating voltage of 15 kV. Subsequently, the dislocation structures near the specimen surface and in the middle of the specimen thickness were investigated by electron channeling contrast imaging (ECCI) at an accelerating voltage of 30 kV. Finally, the plastic strain distribution in the middle of the specimen thickness was analyzed by electron backscattering diffraction (EBSD) measurements at 15 kV with the beam step size of 50 nm. For the EBSD and ECCI characterizations, the sample was mounted in resin, and the specimen surface was mechanically ground with silicon carbide grinding paper P1500 and P4000 followed by mechanical polishing with 9 μm and 3 μm

monocrystalline diamond suspension. Finally, mechanical polishing was performed using 50 nm colloidal silica.

Furthermore, under the sustained load, the crack is supposed that it does not propagate in the air environment. Evidentially, Gerberich et al. [50] performed a sustained load in laboratory air (70% humidity air) for 3 days using a disk-shaped compact tension specimen (the specimen thickness was 1.6 mm) of a single-crystalline Fe-3wt.%Si alloy in which the orientation of the crack plane and the crack growth direction were the same as the present specimen. The crack initiation was in the center of the specimen due to the effects of hydrogen generated from the humid air. The initiation of the crack took much longer time at the center of the specimen and did not extend unless adding more load into it. Hence, in this study, the sustained load test in air environment was not performed to compare against the case of a hydrogen environment.

2.3 Results

2.3.1 Fractography investigation

Fig. 2.2(a) shows an overview of a secondary electron (SE) image of the whole fracture surface (fracture surfaces on the left-hand side of the notch). The thickness of the region near the fracture surface is thinner along the crack propagation path. It is supposed that, during the crack propagation, the zones near the crack tip side surfaces are predominately under plane stress, necking (out-of-plane shear deformation) hence occurs ahead of the crack tip because of the absence of the thickness constraint. In parallel with this, a linear increase in the size of the crack tip plastic zone with the

crack length was observed [52]. Fig. 2.2(b) demonstrates the presence of striation pattern; they were observed across the entire fracture surface. The striation pattern has a convex shape toward the crack propagation direction, as indicated by the red dashed line. This indicates that the crack front propagated preferentially in the center of the specimen compared to at the sides. Furthermore, the clear striation formation shown in Fig. 2.2(c) indicates occurrence of in-plane plastic shear deformation at the crack tip during crack propagation [49, 72]. These facts indicate that the crack tip deformation first occurred in the center of the specimen under plane strain conditions; subsequently, the in-plane shear plastic deformation gradually propagated toward the side surfaces. Moreover, SE images of the fracture surfaces in high magnification levels show the facets between striations, as shown in Fig. 2.3. The facets seem to be not flat and has an appearance of a mottled contrast. Regarding previous studies that performed not only TEM to investigate dislocations beneath the fracture but also atomic force microscopy (AFM) along with high-resolution SEM to investigate the quasi-brittle fracture surfaces of HE in ferrite iron [75] and Fe-Si alloy [49], the mottled contrast indicates the appearance of either dimples [75] or slips (the ductile shear crack caused by the interaction between fine slips promoted by hydrogen) [49].

Notably, the specimen side surface (Fig. 2.2(d) and (e)) also shows surface reliefs (slip lines), which indicates the occurrence of out-of-plane plastic shear deformation, and have been observed previously [72, 73, 76]. Three types of surface reliefs were observed on the specimen side surfaces. The first type was relatively straight slip lines that were activated by {112} slips, and was completely connected to the striation lines on the fracture surface. The {112} slip lines were curved towards

about 45˚ to the crack propagation direction in regions away from the fracture surface, which is indicated as the second type. The third type was curved slip lines that are not associated with the striation formation; they are inclined over 90˚ from the crack propagation direction. The three slip formations are discussed in detail as follows. The first and second types of slip lines corresponds to out-of-plane shear, which relates to the crystallographic requirements of {112} slips. With the present crystallographic orientation condition, only {112} systems allow in-plane shear that contributes to crack propagation. However, {112} slips also requires out-of-plane shear. Therefore, propagation of the crack tip deformation in the specimen interior creates the surface reliefs on the specimen side surfaces. Since the specimen sides are predominantly under plane stress conditions [77, 78], the slip lines gradually inclined to 45˚ to the crack propagation direction further from the crack plane. The third type of out-of-plane shear cannot be explained by the crack tip deformation under plane strain conditions, because dislocation emission or associated deformation cannot dominate slip along the planes inclined over 90˚ to the crack propagation direction. Instead, the third type of slip can be explained by deformation in regions far from the crack front, near the specimen side surface. The occurrence of the plane-stress-condition-dominated deformation is consistent with a previous report [52], that indicated the occurrence of necking at the crack tip by out-of-plane-shear type {112} slips. Hence, the deformation sequence associated with the hydrogen-induced delayed crack propagation is divided into two cases: (1) near-in-plane plastic shear propagating from interior to the side surfaces in the vicinity of the crack tip/plane, and (2) out-of-plane plastic shear propagating from the side surfaces to the interior in a region slightly further from the side crack tip/plane.

2.3.2 Dislocation distribution observation

Fig. 2.4(a) shows the fracture surface in the region (as indicated in Fig. 2.2(a)) used for the following ECCI. First note the ECC image near the specimen surface, shown in Fig. 2.4(b). In this image, the surface orientation is optimized to Bragg's condition in the lower left-hand corner. The bright contrast in the other regions is caused by plastic strain evolution, owing to the orientation gradient associated with the presence of dislocations. The plastic deformation is composed of three regions, denoted as Regions A, B, and C, where different contrasts are observed. The contrast changes from dark to bright from Region A to B, then from bright to dark again from Region B to C. Furthermore, while the width of Region A increases with increasing crack length, but the width of Region B was almost constant. In Fig. 2.4(b), three types of line pattern were observed, that correspond to the slip lines observed in Fig. 2.2(e). These patterns signify the low and high dislocation regions, as shown in Fig. 2.4(c). Specifically, the bright contrast is attributed to dislocation microstructure evolution, and dark contrast is due to relatively low dislocation density. However, the dark line pattern corresponds to the slip lines, which indicates a "highly deformed" region. This indicates that the dark lines corresponding to the slip lines are caused by dislocation emission to the side surfaces. Moreover, this also supports the occurrence of out-of-shear deformation. Region C was not observed in the middle of the specimen thickness, as shown in Fig. 2.4(d), which suggests that the change in contrast from Region B to C in Fig. 2.4(b) is probably due to dislocation emission to the side surfaces or fracture surface at the corner of two surfaces. Since the corner of the two surfaces is strongly affected by the image force, the dislocation emission would have occurred

preferentially. Furthermore, the line pattern associated with dislocation emission was not observed in the middle of the specimen, instead, dislocation cells with a cell size of about 1 μm were observed as shown in Fig. 2.4(e). This indicates that dislocation movement does not freely in the specimen interior, and dislocations on multiple slip systems are interacted each other. Furthermore, the dislocation density decreased with increasing the distance from the fracture surface, as shown in Fig. 2.4(c), which results in two different characteristic regions, similar to Regions A and B in the section near the specimen side surface. Hence, the presence of two types of plastic zone is intrinsic, irrespective of the position within the specimen. More specifically, it is speculated that Region A corresponds to the plastic zone, observed as a necked region in the previous study [52]. The size of the necked plastic zone increased with increasing crack length; namely, this plastic zone was dominated by out-of-plane deformation propagating from the side surface to the interior. On one hand, the deformation microstructure near the fracture surface must stem from the crack propagation, which requires in-plane deformation under plane strain conditions. Therefore, Region B would be associated with plane-strain-condition-controlled deformation that propagates from the interior to the side surface. In this regard, it is needed to discuss how the plane-strain-condition-controlled deformation provides a constant plastic zone, such as that in Region B.

2.3.3 Plastic strain investigation

Fig. 2.5 shows a set of EBSD analyses in the region highlighted in Fig. 2.4(d). Interestingly, the grain reference orientation deviation (GROD), which correlates to plastic strain [79-81], indicates that the magnitude of the plastic strain gradient in Region B is much lower than that in Region A, except for extremely near the fracture

surface (Region C). Note that Region C corresponds to the white band (the band is about 2 μm in width) on the top of Fig. 2.4(b) and (d), which is the region immediately beneath the fracture surface. The validity of the orientation information near the fracture surface requires further assessment because the edge of the surface has various types of edge effects during EBSD and ECCI analyses. Coupled with the discussion for Fig. 2.4, Region B has higher plastic strain but lower magnitude of plastic strain gradient compared with those of Region A. In fact, the size of Region B in Fig. 2.5(c) corresponds to that of Region B in Fig. 2.4; therefore, this peculiar strain gradient might be correlated to a reason for the constant plastic zone size of Region B in Fig. 2.4.

2.4 Discussion

Based on microscopic observations of the crack tip behaviour and fracture surface, and in particular considering the dislocation patterns in Fig. 2.4 and the peculiar strain gradient in Fig. 2.5(c), the complex plastic zone structure around the crack is schematically summarized in Fig. 2.6(a). The three regions are clearly indicated: Region C, in the vicinity of the fracture surface, has extremely high plastic strain; Region B has a high strain level associated with a high dislocation density, and remains a constant width despite the increasing crack length; and Region A has a relatively low strain level, and linearly increases in the width size with the crack length. Also, a model that demonstrates the crack propagation, the effect of hydrogen on the plastic deformation at the crack tip, and the formation mechanism of Regions A, B, and C is proposed. The proposed model is presented schematically in Fig. 2.6(b). The model is divided into three stages, which are described in detail below.

Stage (I) indicates the crack blunting process. As shown in (I-1), a plastic zone (the dotted region) forms around the crack tip, which is considered as Region A, and its size linearly increases with the crack length [82]. Simultaneously, a hydrostatic stress field forms ahead of the crack tip, and hydrogen then accumulates in the hydrostatic stress field [41, 42], as an ellipse-shaped fine dotted region ahead of the crack tip. Adsorbed hydrogen also enhances the dislocation emission from the crack tip [46, 83], in which dislocations alternatively emit into two directions ($[\bar{1}11]$ and $[\bar{1}1\bar{1}]$), as shown in Fig. 2.6(c). As a result, the crack tip is opened by alternating slips, and the maximum stress field appears ahead of the crack tip [72, 84], as shown in (I-2).

Stage (II) indicates damage (the voids/shear cracks) initiation process. Hydrogen diffuses to and concentrates at the maximum stress field [73], as shown in (II-3). Dislocation multiplication associated with hydrogen effects plays a vital role in the maximum stress field. Namely, dislocations on multiple slips interact with each other that causes vacancy formation [75, 85-87]; vacancies then accumulate, which leads to forming nano-voids [75]. On the other hand, hydrogen can enhance localized slips in the maximum stress field, which caused localized-shear crack (the shear crack caused by the interaction between fine slips) [49]. Consequently, it is considered that voids form or shear crack occurs ahead of the crack tip, as shown in (II-4).

Stage (III) indicates the sub-crack initiation and opening process. Sub-crack initiates by the growth and coalescence of voids or shear crack. The sub-crack then connects to the main crack due to necking or shearing, as shown in (III-5). Subsequently, the unloading occurs in the regions surrounding the newly cracked

surfaces [88, 89]. The unloading causes the material in the unloading regions to reload plastically in the reverse sense, which contributes to form the lower magnitude of the plastic strain gradient in Region B compared to that of Region A. Simultaneously, the crack tip is opened by the crack tip plastic deformation, and Region B is formed, as shown in (III-6). Besides, a numerical investigation and three-dimensional modeling of crack growth under steady-state and quasi-static conditions was performed [90, 91], the results revealed that the material behind the crack tip undergoes further yielding due to the tensile stress (σ_{xx}) in the x-direction (the crack propagation direction [$\bar{1}10$]). Particularly, σ_{xx} reached a yielding strength of the material and plastic strain increase in the x-direction, which caused the decreasing plastic strain in y-direction (loading direction [001]) due to the Poisson effect. This is the final process as a cycle of this hydrogen-related process. Moreover, the region in the vicinity of the fracture surface, where voids/shear cracks initiated, is considered as Region C.

Furthermore, the COD and the striation spacing are constant and independent of the crack propagation rate and the crack length [52]. These facts implied that the time necessary for Stage (I) and Stage (III) is not rate-limiting. According to the characteristics of Regions A, B, and C, it is speculated that not only the stress-driven diffusion but also the role of dislocations such as dislocation transport [92] probably accelerated the accumulation of hydrogen to the crack tip. In combination with the constant striation spacing and monotonic increase of the crack propagation rate with the plastic zone size, it is postulated that the time necessary for Stage (II) is rate-limiting, which is the time necessary for gathering hydrogen at the maximum stress field.

2.5 Conclusions

In summary, the microscopic features of hydrogen-induced delayed crack propagation in a thin sheet of single-crystalline Fe-3wt%Si alloy were investigated. The key findings are as follows:

- The crack propagates discontinuously accompany extensive plastic deformation.
- The crack tip plastic deformation associated with the effect of hydrogen during the crack propagation leaves three adjacent regions where different plastic strain gradients and dislocation densities are observed.
- The results revealed the effects of plastic deformation and hydrogen-dislocations interaction around the crack tip on the rate-limiting process of hydrogen-induced delayed crack propagation in thin specimens.
- Considerable necking was observed in the present thin specimen; however, the necking (out-of-plane shear deformation) has no significant effect on the in-plane shear deformation. Hence, in-plane shear deformation in a thin specimen is the same as that in thick specimens, which results in the same crack growth mode in thin and thick specimens.

2.6 Figures

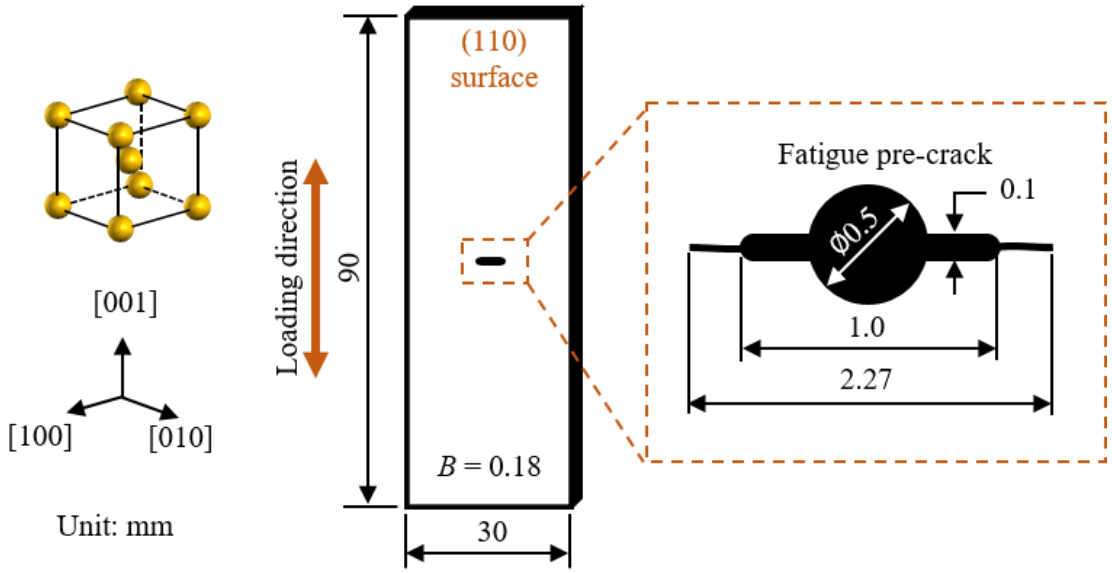

Fig. 2.1. Specimen geometry and crystallographic orientation. Configuration of the notch and fatigue pre-crack is illustrated in the dashed-line square. The fatigue pre-crack length ($2a$) was 2.27 mm. The specimen thickness (B) is 0.18 mm.

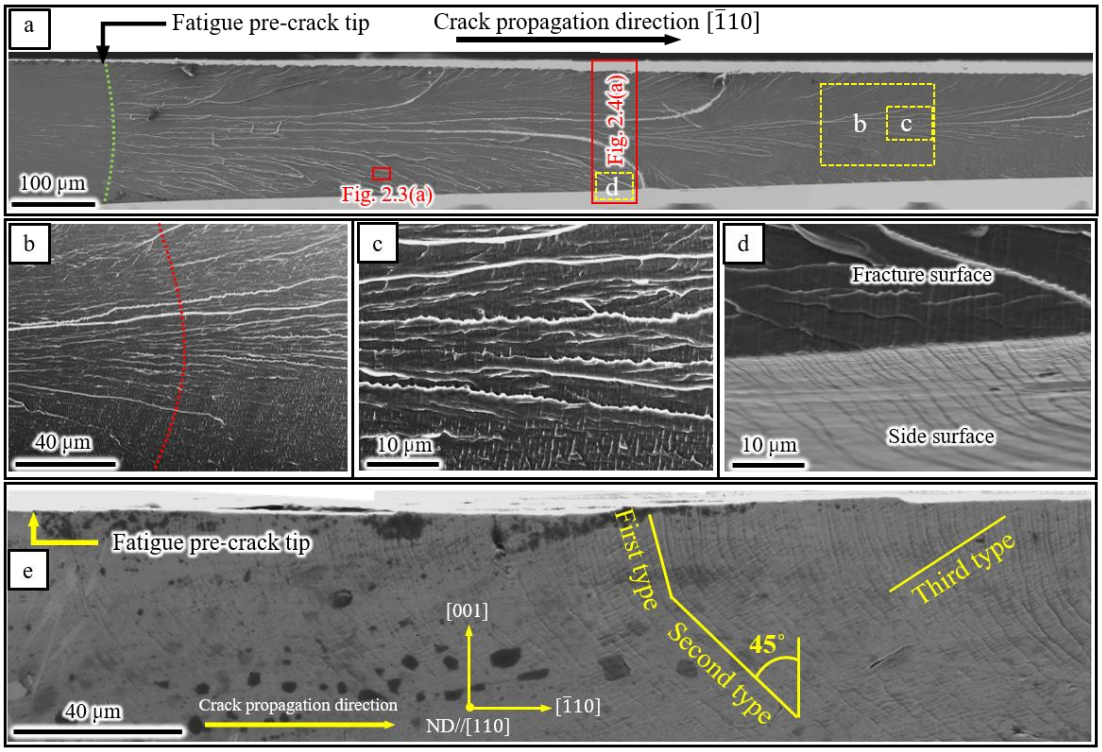

Fig. 2.2. SE images of the fracture surface and side surface of the specimen. (a) Overview of SE image of the fracture surface including the fatigue pre-crack; (b) higher magnification of the part (a) showing the traces of the crack propagation process (the crack length a = 2.0 mm, and the crack propagation rate $da/dt = 4.18 \times 10^{-8}$ m s^{-1}); (c) striations on the fracture surface; (d) the matching of the striations and slip lines on the specimen side surface (a = 1.75 mm, $da/dt = 1.11 \times 10^{-8}$ m s^{-1}); (e) an overview of SE image of the specimen side surface showing the slip lines. Note that the fatigue pre-crack length is 2.27 mm. The striation pattern is convex rightward, as indicated by the red dashed line in (b).

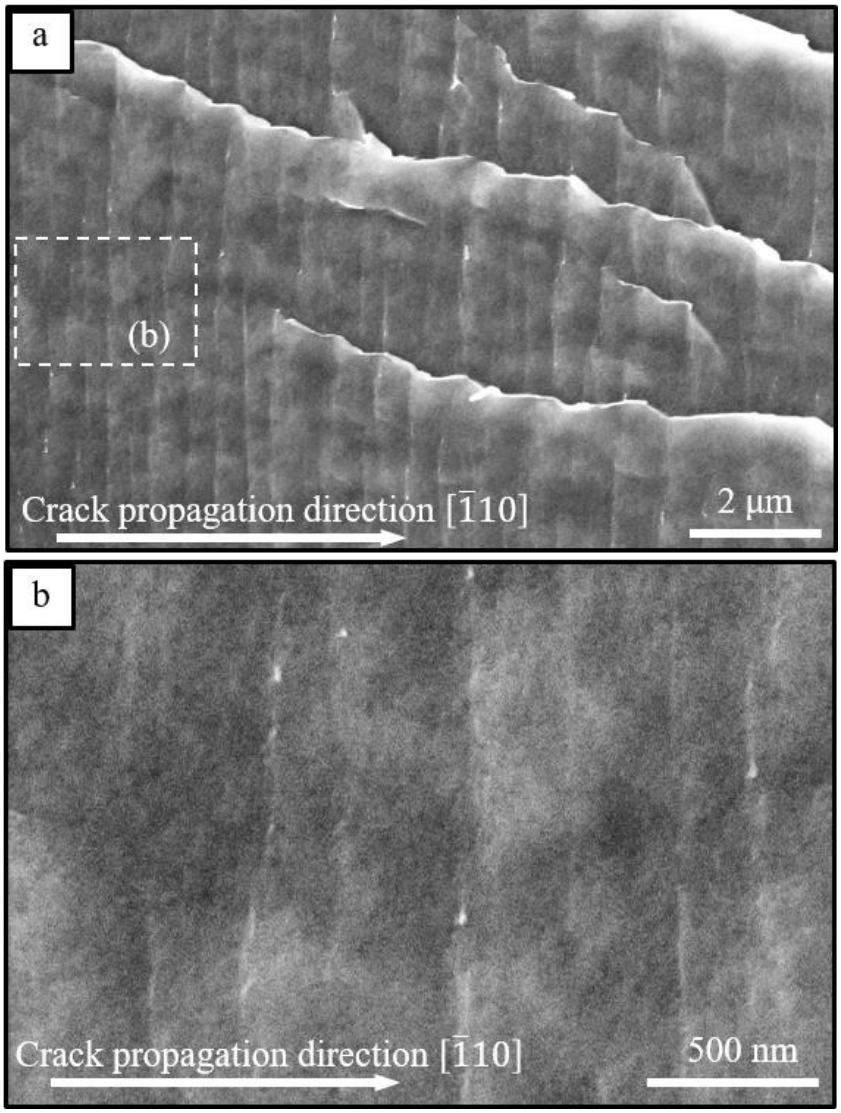

Fig. 2.3. SE images in high magnification levels showing apparent striations, which was taken by Takahashi et al. [52] (a = 1.49 mm, as highlighted in Fig. 2.2(a)). The facets between striations have a mottled contrast. Regarding previous studies that performed not only TEM to investigate dislocations beneath the fracture but also atomic force microscopy (AFM) along with high-resolution SEM to investigate the quasi-brittle fracture surfaces of HE in ferrite iron [75] and Fe-Si alloy [49], the mottled contrast indicates the appearance of either dimples [75] or slips (the ductile shear crack caused by the interaction between fine slips promoted by hydrogen) [49].

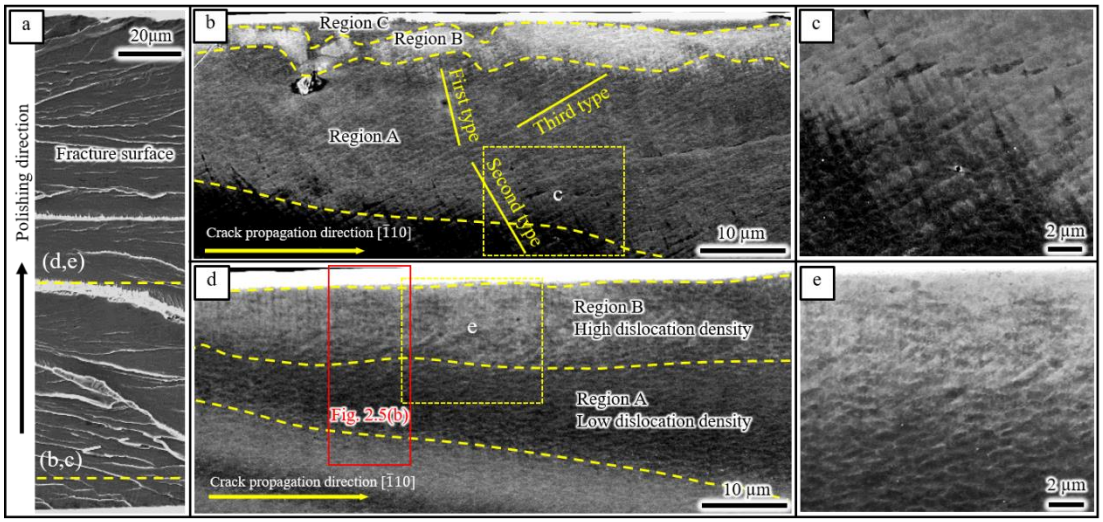

Fig. 2.4. (a) SE image showing a part of the fracture surface indicated in Fig. 2.2d (a = 1.75 mm, da/dt = 1.1 × 10^{-8} m s^{-1}). The lines labeled b–c (near the edge of the specimen) and d–e (near the center of the specimen) indicate the locations of the cross-sectional ECC images in (b, c), and (d, e), respectively, showing the dislocation patterns underneath the fracture surface. The surface orientation is optimized to Bragg's condition for the left down part in (b).

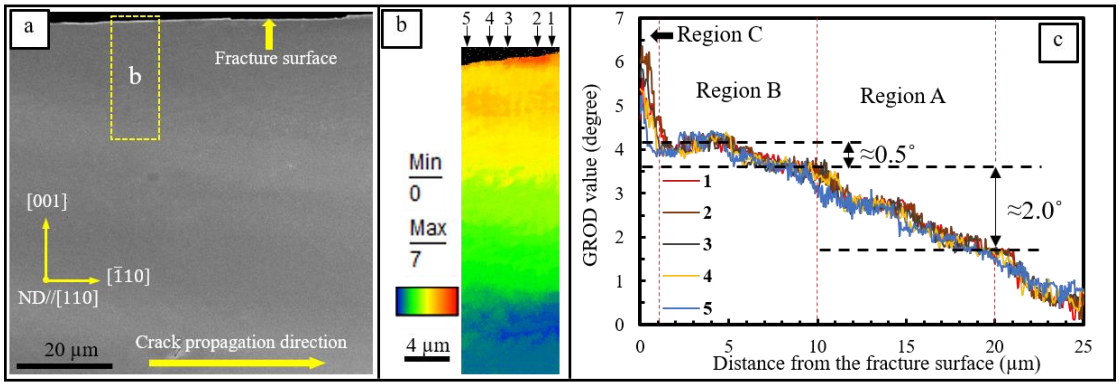

Fig. 2.5. (a) SE image of a polished cross-section along the center of the specimen (the same position as the line labeled d-e in Fig. 2.3(a); (b) GROD map of the region highlighted by yellow rectangle in (a); (c) Misorientation profile depicted from EBSD measurements along the loading direction [001] (indicated by the five arrows in (b)). GROD has been reported to have a correlation with plastic strain [79-81]. The width of Region B in (c) is identical with the width of Region B in Fig. 2.3(d).

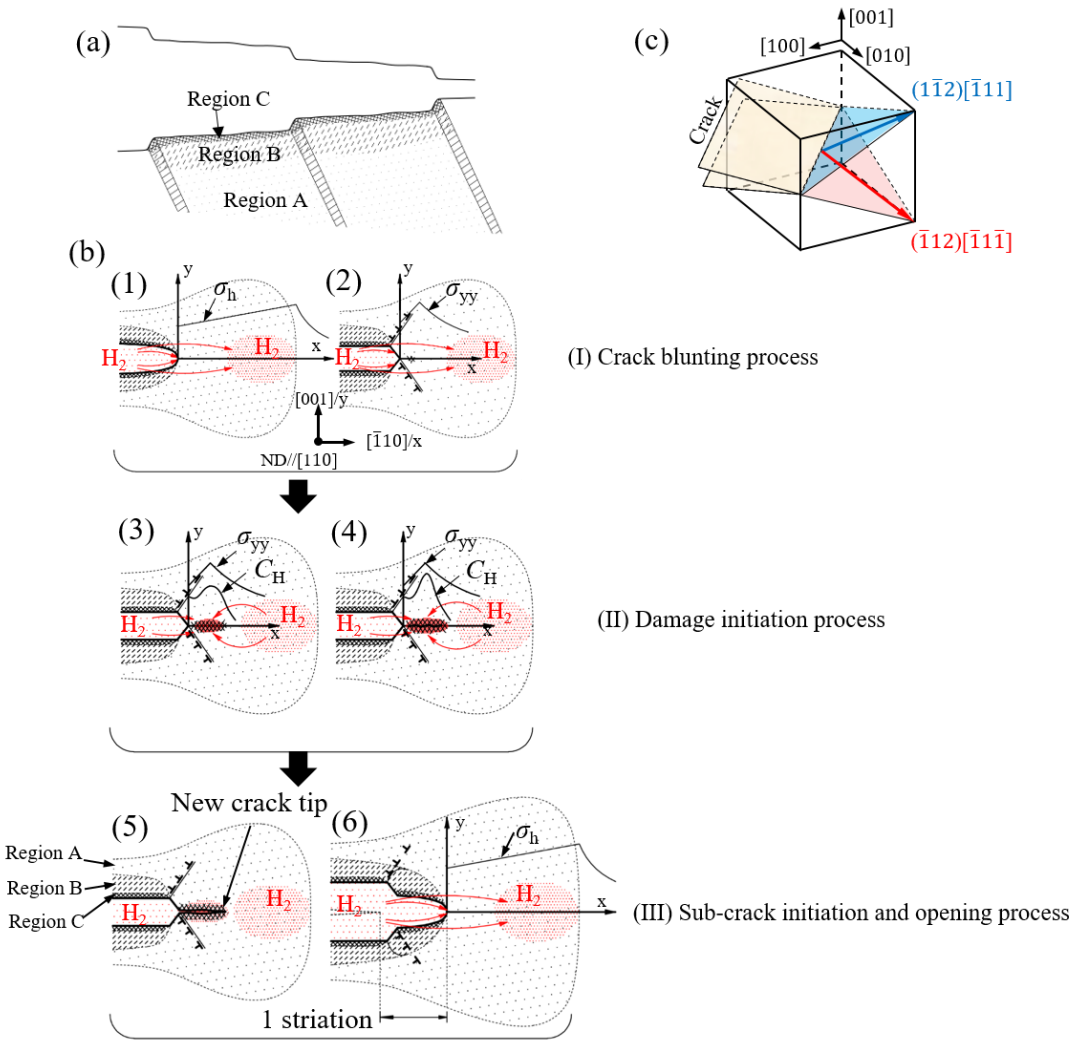

Fig. 2.6. (a) A schematic showing the plastic deformation and dislocation structure behind the fracture surface; Region A has an increasing plastic zone size, but relatively low strain level; Region B has a constant plastic zone size, high strain level, and high dislocation density; and Region C is the region has extremely high plastic strain; (b) a schematic illustrating the crack propagation process associated with the effect of hydrogen on the plastic deformation at the crack tip (I - III); σ_h is hydrostatic stress, σ_{yy} is normal stress in the tensile direction, C_H is hydrogen concentration; (c) the $(1\bar{1}2)[\bar{1}11]$ and $(\bar{1}12)[\bar{1}1\bar{1}]$ slip systems are corresponding to in-plane shear deformation.

CHAPTER 3. Roles of Hydrogen and Plastic Strain Distribution on Delayed Crack Propagation

3.1 Introduction

A sub-critical crack propagation of a cracked metallic material under sustained load in hydrogen environment is termed as hydrogen-induced delayed cracking or generally called HAC. A large number of studies have conducted experiments to investigate the macroscopic and microscopic properties of HAC, and several models related HAC have been proposed. In such studies, associated with the macroscopic property of HAC, hydrogen effected on the yield and flow strengths of metallic material [93]. Related to microscopic features of HAC, hydrogen caused localized slip at the crack tip [94], and hydrogen adsorption facilitated the nucleation of dislocation emission at crack tips [25, 95]. In the kinetic models of HAC, the defining factor was reported as the specific dislocation structure at the crack tip [72-74], and hydrogen diffusion and accumulation dominate the HAC process [41, 49, 51, 71]. Furthermore, several theories related to HAC have been proposed, such as HELP [21, 23, 96, 97], HEDE [12, 50, 73, 98], and AIDE [25].

However, most of the above studies were mainly performed with thick specimens. It is well known that state-of-stress effects play an essential role in HAC process, wherein HAC is typically predominated under plane strain conditions where highest stress tri-axiality exhibits ahead of the crack tip [50, 71]. Significantly reducing

specimen thickness can reduce the stress tri-axiality ahead of the crack tip. Hence, this can cause increase local plastic strain around the crack tip as well as reduce the amount of hydrogen enrichment near the crack tip. Therefore, this may have significant effects on the HAC process. Takahashi et al. [52] investigated the macroscopic property of HAC in a thin sheet of single-crystalline Fe-Si alloy (the specimen thickness is about 0.2 mm), particular findings in thin specimens were summarized in the introduction section of Chapter 2. However, these findings are briefly introduced again as follows: (1) the crack opening displacement (COD) 200 μm behind the crack tip and the unit distance of crack propagation, striation spacing, were independent of both the crack length and the crack propagation rate (da/dt), (2) log(da/dt) is proportional to the crack length during the whole propagation process, and (3) the crack tip plastic zone linearly increases in size with the crack length. It is suggested that the plastic deformation around the crack tip affects the rate-limiting process. In the later, in Chapter 2, the microscopic features of hydrogen-induced delayed crack propagation in a thin specimen of single-crystalline Fe-Si alloy were investigated. The results showed that during the crack propagation, the crack tip plastic deformation associated with hydrogen effect left three adjacent regions beneath the fracture surface in which each region has different plastic strain gradients and dislocation densities. Besides, the mechanism of hydrogen-induced delayed crack propagation in a thin sheet of single-crystalline Fe-Si alloy has been proposed. The results revealed the effects of plastic deformation and hydrogen-dislocation interaction closed to the crack tip on the rate-limiting process.

However, there is no detailed discussion about the relation between macroscopic and microscopic properties of hydrogen-induced delayed crack propagation in thin specimens. Also, the above two studies [52, 99] have no comparison between hydrogen and hydrogen-free. In this study, first, the macroscopic and microscopic properties of a thin sheet of single-crystalline Fe-Si alloy tested in air and hydrogen environments are first investigated and compared. Secondly, the relation between macroscopic and microscopic properties is discussed. Namely, roles of hydrogen and plastic strain distribution on delayed crack propagation are emphasized.

3.2 Experimental procedure

The examined material was a single-crystalline Fe-3wt%Si alloy with a (110) surface. The specimen geometry and crystallographic orientation used in present study are the same as those presented in Chapter 2 (Fig. 2.1). A rectangular specimen (90 × 30 mm) with a thickness of 0.18 mm was cut from a mother plate. A through-notch was introduced along $[\bar{1}10]$ direction at the center of the specimen, in which the hole and the notch were respectively introduced by the micro-drilling machine and electrical discharge machining (EDM) machine (see the enlarged image of Fig. 3.1). A fatigue pre-crack was then introduced on the (001) plane from the notch root. The fatigue pre-crack was introduced by stress control, and the stress waveform was a sine wave (maximum stress: σ_{max}= 200 MPa (the load per the area of the cross-section that is parallel to the (001) plane without the notch and pre-crack); stress ratio: R = 0.05, and frequency: 1 Hz). The yield strength (σ_Y) of this material in the [001] direction was measured as 290 MPa. The result of the tensile test (the engineering stress-strain curve) for a smooth specimen is shown in Fig. 3.2. The specimen dimensions and

crystallographic orientation of a smooth specimen are the same as those shown in Fig. 3.1; however, it has no notch and pre-crack. The crack propagation tests were conducted in an air environment at room temperature. A specimen with the fatigue pre-crack length $2a$ = 1970 μm was used to perform a tensile test under displacement control by using an electro-hydraulic testing machine (the cross-head displacement movement speed is 0.0017 mm/second). The plot of cross-head displacement versus the load of the specimen contained a pre-crack is shown in Fig. 3.3. The crack length and CTOA were observed by an optical microscope.

After the test, the topologies of the fracture surfaces and the side surfaces of the specimens were observed by field emission scanning electron microscopy (SEM) at an accelerating voltage of 15 kV. In order to investigate the plastic strain distribution and dislocation structure in the middle of the specimen thickness, the cracked specimens were first mounted in the resin. Secondly, the material in a half thickness was removed by mechanically grinding with silicon carbide grinding paper P1500 and P4000. Mechanical polishing with 9 μm and 3 μm monocrystalline diamond is then followed. Finally, mechanical polishing was performed using 50 nm colloidal silica. Subsequently, the plastic strain distribution was analyzed by electron backscattering diffraction (EBSD) measurements at 15 kV with the beam step size of 100 nm, and the dislocation structures were investigated by electron channeling contrast imaging (ECCI) at an accelerating voltage of 30 kV. In order to compare the material behaviors between air and hydrogen, more in-detail analyses of a broken specimen in hydrogen, which was presented in Chapter 2, were performed again.

3.3 Results

3.3.1 Crack propagation behavior

Fig. 3.4 shows the plot of half crack length with time. The crack propagation is stable in both air and hydrogen environments. In an air environment, under constant displacement speed, *a* linearly increases with time. In a hydrogen environment, *a* slowly increases before reached a value of 2 mm. Subsequently, it then rapidly increases until it reached a value of 3.7 mm where unstable crack growth occurred. Figs. 3.5(a) and (b) show optical images of the necked zones during the crack propagation in air and hydrogen environments [19], respectively. In these images, the dark regions around the crack wake, where the reflection of light illumination was scarce due to specimen necking (i.e. out-of-plane shear deformation), can be seen. Fig. 3.5(c) shows the CTOA as a function of *a* of the specimens tested in air and hydrogen environments. Here, the application of stress intensity factor, *K*, is not valid because the whole crack propagation process occurred under the large-scale yielding condition. However, in order to compare with other studies, the corresponding *K* values are shown below *a*. Note that CTOA in air shown here corresponds to the amount of mode I crack propagation; the corresponding fracture surface is shown in Fig. 3.6(a). COTA is approximately constant in a hydrogen environment; however, it slightly increases in an air environment. Notably, the present values of CTOA hydrogen environments are contradictory to the fracture mechanics concept, where CTOA should increase as *a* or stress intensity increases [89].

3.3.2 Investigation of the fracture surfaces and the side surface of the specimens

Fig. 3.6 and Fig. 3.7 show secondary electron (SE) images in low and high magnification levels of the fracture surfaces in an air environment and a hydrogen environment, respectively. The crack propagation in the $[\bar{1}10]$ direction along the (001) plane was stable in both air and hydrogen environments. In an air environment, Fig. 3.6(a) shows the early stage of crack propagation corresponding to the amount of mode I crack propagation (flat fracture surface in the central region, about 500 μm from the fatigue pre-crack); the later stage of crack propagation was totally about 45° shear fracture, as shown in Figs. 3.6(b) and (c). Fig. 3.7(a) shows an overview of a SE image of the whole fracture surface of the specimen tested in a hydrogen environment. Both environments, as shown in Figs. 3.6(a) and 3.7(a), the overall appearance of the mode I fracture surfaces is as river-like markings and is similar to that found in thicker specimens, which were used the same orientation, as reported in [50, 51, 69]. The specimen thickness of the regions near the fracture surface becomes thinner along with the crack propagation path (from right to left in Fig. 3.6(a) and Fig. 3.7(a)). It is supposed that, during the crack propagation, the regions near the crack tip side surfaces are predominately under plane stress conditions, necking (out-of-plane shear deformation) hence occurs owing to the absence of the thickness constraint. Moreover, near the sides of the fracture surface, shear slips were observed, as outlined by the red dashed lines in Figs. 3.6(a) 3. 7(a). However, in a hydrogen environment, owing to the subcritical crack propagation occurred associated with hydrogen-induced delayed crack propagation, the regions of shear slips are thinner than that of the specimen tested in an air environment. Also, a significant reduction of the specimen thickness of

regions near the fracture surface is observed in an air environment. This is due to crack propagation in an air environment under higher K compared to that in a hydrogen environment; hence, significant necking was observed in an air environment, which is shown in Figs. 3.5(a) and (b). Moreover, a closer observation of the fracture surfaces, the striation pattern can be seen, as shown in Figs. 3.6(d, e, and f) and Figs. 3.8(b, c, and d). The striations are taken as evidence that the propagation is discontinuous. The striation spacing is almost constant, irrespective of the crack length. However, the striation spacing in a hydrogen environment is about 0.4 μm and is shorter than that in an air environment (about 0.65 μm). Fig. 3.7 shows SEM images in high magnification levels of the fracture surfaces of specimens tested in air, in which nano-dimples can be seen in Figs. 3.7(c) and (d). On the other hand, high magnification SEM images of the fracture surfaces of the specimens tested in hydrogen showed facets between striations; the facets have a mottled contrast, which indicated the appearance of dimples of slips, as presented in Fig. 2.3 in Chapter 2. The striation lines have a convex shape toward the crack propagation direction, as outlined by red dashed lines in Figs. 3.9(a) and (c) and as reported in other studies [51, 73, 99], which indicates that the crack front propagated predominately in the center region of the specimen compared to near the side. Besides, striation lines are also observed in the shear slip regions (near the side) of the fracture surface to accommodate the crack front during the crack propagation, as shown in Figs. 3.9(b) and (d).

Furthermore, the slip traces on the specimen side surfaces, which correspond to the early stage of crack propagation, of the specimens tested in air and hydrogen environments can be observed and are shown in Figs. 3.10(a) and (c), respectively.

These slip traces were also observed previously [25, 51, 69, 76, 100]. Slip traces indicate the occurrence of out-of-plane plastic shear deformation and demonstrate that extensive plastic deformation was during crack propagation. Extensive slip traces are observed on the side surfaces of the specimens tested in air environment. This is consistent with a larger necked zone in air environment, as shown in Fig. 3.5(a). Three types of slip traces were observed on the specimen side surfaces. The first type was relatively straight slip lines; it was connected entirely to the edge of the fracture surface. The second type was curved further towards the crack propagation direction in the regions away from the fracture surface. The third type inclines over 90˚ to the crack propagation direction. These slip formations were discussed in detail in Chapter 2 [99]; however, it is briefly introduced as follows. The striation indicates the occurrence of in-plane shear deformation at the crack tip during the crack propagation. With the present crystallographic orientation condition, it is speculated that only $\{112\}\langle 111\rangle$ slip system allows in-plane shear and out-of-plane shear that contributes to crack propagation, as reported in previous studies [76, 100, 101]. The $\{112\}\langle 111\rangle$ slips obviously require out-of-plane shear, which creates the surface reliefs (the first type of slip traces) on the specimen side surface. Since the plane stress conditions dominate deformation in the regions near the crack tip side surface and the region away from the crack tip, the slip traces (the second type of slip traces) thus curved further towards the crack propagation direction.

3.3.3 Plastic strain investigation

For the specimens tested in an air environment, Fig. 3.11 shows the sets of EBSD analyses. Corresponding to the crack length of a = 1.13 mm, 1.23 mm, 1.37 mm, and

1.49 mm, four regions, which have the same area, were selected for investigating EBSD. These different crack lengths were indicated in Fig. 3.6(a). In each region, a set of EBSD analyses, such as GROD and KAM, is sequentially shown from left to right in Fig. 3.11(a). Note that GROD has been reported to correlate with the plastic strain [79-81]. Fig. 3.11(b) shows the misorientation profile depicted from GROD maps along the loading direction [001], which are indicated by eight arrows in Fig. 3.11(a). It can be seen that the magnitude of plastic strain slightly increases as the crack length increases. Notably, the distribution of plastic strain beneath the fracture surfaces can be divided into three adjacent regions, which are denoted as A, B, and C. In the vicinity of the fracture surface, Region C has an extremely high plastic strain and has the steepest plastic strain gradient while Region B adjacent to Region C has a high plastic stain but has lowest plastic strain gradient. Away from the fracture surface, plastic strain in region A is lower than that in Regions B and C; however, the plastic strain gradient in Region A is higher than that in Region B but lower than that in Region C.

For the specimens tested in a hydrogen environment, Fig. 3.12 shows a set of EBSD analysis. The arrangement of maps (GROD and KAM) and the misorientation profile, is the same as those of Fig. 3.11. The regions corresponding to the crack length of a = 1.30 mm, 1.50 mm, and a = 1.70 mm were selected for investigating EBSD. These different crack lengths were indicated in Fig. 3.8(a). It is very interesting that the trend of the plastic strain distribution underneath the fracture surface of the specimen tested in a hydrogen environment exhibits quite similar to that of the specimen tested in air

environment; namely, three distinguishes regions that have different plastic strain gradient are observed, as shown in Fig. 3.12(b).

Furthermore, a comparison of the plastic strain beneath the fracture surfaces has been conducted, as shown in Fig. 3.13. To perform this, in each sample, a region that has the same area illustrated in Figs. 3.11(a) and 3.12(a) was selected to investigate by EBSD (in air: a = 1.4 mm, K = 20.8 MPam$^{1/2}$; in hydrogen: a = 1.5 mm K = 17.2 MPam$^{1/2}$). The misorientation profile depicted from EBSD along the loading direction [001] was conducted. Figs. 3.13(a) and (b) show IPF and GROD maps conducted from EBSD analysis in air and hydrogen environments, respectively. As mentioned above that three adjacent regions (Regions A, B, and C) which have different plastic strain gradients can be seen. However, the magnitude of the plastic strain of each region observed in an air environment is larger than that in a hydrogen environment. Also, the width size of Regions B and C in the air is larger than that in the hydrogen. Meanwhile, the plastic strain gradient observed in Region C in a hydrogen environment is more significant than that in an air environment; the other regions (Regions A and B) are quite similar. The difference in sizes, the magnitude of plastic strain, and strain gradients of the corresponding region in air and hydrogen environment will be discussed later.

3.3.4 Dislocation structure observation

Figs. 3.14(a) and (d) shows cross-sectional SE images observed in the middle of the specimen thickness in air (at a = 1.4 mm) and hydrogen (at a = 1.5 mm) environment, respectively. In these images, the areas selected for investigating EBSD (as shown in Figs. 3.13(a) and (b)) are indicated. Corresponding to these SE images, ECC images

are shown in Figs. 3.14(b) and (e). In these ECC images, the bright contrast is caused by the plastic strain evolution, which is due to the orientation gradient associated with the presence of dislocations. The white bands in the vicinity of the fracture surface near the top of Fig. 14(b) and (e) is constant in width size (about 2 μm in width), which is denoted as Region C. Note that this region corresponds to Region C observed in Fig. 3.11(b), Fig. 3.12(b), and Fig. 3.13.(c) owing to the edge of the surface has various types of edge effects during EBSD and ECCI analyses. Region C does not represent the dislocation structure in the vicinity of the fracture surface. In adjacent to Region C, a wider region labeled as region B has a dense density of dislocations. Interestingly, the width size of Region B is almost constant, despite the crack length increases. In an air environment, dislocations in Region B appeared as “criss-cross” bands, and it seems that it has a higher orientation gradient and dense dislocation between bands compared to the others, as shown in Fig. 3.14(c). Meanwhile, dislocation cells with a cell size of 1 μm are observed in a hydrogen environment, as shown in Fig. 3.14(f). Surprisingly, in each environment, Region B showed in Fig. 3.13(b) and Region B showed in Figs. 3.14(b) and (e) are constant in size and are observed near the fracture surfaces. Away from the fracture surfaces, a region has a lower density of dislocations can be observed, which is labeled as Region A. Coupled with the linearly increasing in size of the necked zones seen in Figs. 3.5(a) and (b), Region A is postulated that it increases in size with increasing crack length. Finally, it is concluding that the presence of two types of plastic zone is intrinsic, irrespective of the position within the specimen. In Fig. 3.14(e), there is a large region that has high brightness contrast. The dislocation structure cannot be seen clearly. However, a corresponding ECC image of

this region is shown in Fig. 3.14(g). It can seem that this region has a lower dislocation density compared to that of Region B.

3.4 Discussion

3.4.1 The role of plastic strain distribution in stable crack propagation

Based on the fractography investigation and the microscopic features of EBSD and ECCI analyses, the crack tip plastic deformation during the crack propagation left three adjacent regions beneath the fracture surface, where different plastic strain gradient and dislocation densities were observed. Also, it is considered that the sequence of the crack propagation is similar in both hydrogen and air environments, which is briefly presented as the following three stages: (I) crack tip blunting by dislocation emission from the crack tip; (II) voids initiation ahead of the crack tip; (III) sub-crack initiation and opening process. In a hydrogen environment, in Chapter 2, a model that demonstrates the crack propagation, the effect of hydrogen on the plastic deformation at the crack tip, and the formation mechanism of Regions A, B, and C was proposed [99]. In an air environment, the mechanism of crack propagation is briefly discussed as follows. Dislocations first emit from one side of the crack plane as loading increases. Large back stress thus shields crack tip on this side. Secondly, dislocation emission from the other side of the crack plane occurs. Note that not only dislocations emitted from the crack tip but also numerous dislocation sources ahead of the crack tip are activated. The dislocations emitted at the crack tip contribute to crack advance but in a small amount, while the dislocations activated ahead of the crack tip contribute to either open the crack tip or to generate strain ahead of the crack tip. To support this, as presented by Takahashi et al. [53], the dislocation emission from the crack tip during

the crack tip opening in fatigue using single-crystalline Fe-Si alloy in a helium environment was investigated by transmission electron microscopy (TEM), they found that slip band emitted from the crack tip and extended about 30 μm away from the crack tip and the slip bands were observed that those were symmetrical about the crack plane. Subsequently, multiple dislocations play a major role ahead of the crack tip, which causes the nucleation of voids [25]. Sub-crack will be initiated by voids growth and coalescence. As a result, the crack propagates by coalescence of sub-crack and main crack. This seems to be identical with the mechanisms of ductile crack propagation in inert environments proposed by Lynch [25].

Moreover, the novel strain distribution along the loading direction was observed, which is indicated by Regions A, B, and C shown in Fig. 3.11(b), Fig. 3.12(b), and Fig.3.13(c). These regions are described as follows. In the context of fracture mechanic [36], in ductile crack propagation, the material behind the newly cracked surface of the growing crack tip has unloaded elastically, which can cause the material in these regions to reload plastically in the reverse sense. Besides, as described in Chapter 2, a numerical investigation and three-dimensional modeling of crack growth under steady-state and quasi-static conditions was performed [90, 91]. The results of these studies revealed that the material behind the crack tip undergoes further yielding due to the tensile stresses (σ_{xx}) in the crack propagation direction. Namely, σ_{xx} reached a yielding strength of the material resulting in increasing of plastic strain in the x-direction (crack propagation direction $[\bar{1}10]$) which caused a decrease of the plastic strain in the y-direction (loading direction $[001]$) due to the Poisson effect. These phenomena are hereafter called the reverse plastic deformation. Hence, it is

speculated that the reverse plastic deformation alters the plastic strain gradient of the region near the fracture surface and leads to form Region B. Besides, the region in the vicinity of the fracture surface, where voids initiate, is considered as Region C.

When the crack propagation is stable in elastic-plastic materials, the yielding region (plastic zone) is not small, and the reverse plastic deformation occurs behind the crack tip. The application of the linear fracture mechanics and elastic-plastic fracture parameters based on plastic deformation theory is thus invalid [36]. CTOA, which reflects the local slope of cracked faces near the crack tip, was found that it is to be approximately constant during stable crack propagation [102, 103]. Also, CTOA is independent of in-plane geometry if the crack length and ligament size are larger than 4 times the specimen thickness [104]. Hence, it was used to modeling and predict stable crack propagation of thin wall structures [104-106]. Several efforts have been made to calculate CTOA from the crack growth resistance curve [107] and consider CTOA corresponding stationary crack opening profiles minus plastic wake profiles [108]. However, these studies did not consider the reverse plastic deformation effect. Note that when the reverse plastic deformation occurs, the materials continue to yield but in the reverse sense [36, 90, 91, 109, 110]. If the reverse plastic deformation is insignificant behind the growing crack tip, it seems that it has no effects on CTOA and the geometry of the growing crack tip. Notably, in the present study, the reverse plastic deformation is significant, which are shown as Region B. Hence, it is essential to speculate that it has significant effects on the value of the present CTOA and the geometry of the growing crack tip, which is discussed below.

Fig. 3.15(a) shows the tendency of the plastic strain distribution shown in Fig. 3.11(b) and Fig. 3.12(b). Also, the triangle-dotted region represents the "evaporated" plastic deformation (the plastic strain decreased) due to the reverse plastic deformation mentioned above, which is here called the "evaporated" region. Fig. 3.15(b) shows the result of measurement of these "evaporated" regions at different crack lengths in air and hydrogen environments. The area of these regions seems to be independent of the crack length. As mentioned above, the reverse plastic deformation occurs during crack propagation, which alters the plastic strain gradient in Region B. Hence, the reverse plastic strain in Region B is speculated that it is caused by the "evaporated" regions. As shown in Fig. 3.15(c), when the sub-crack initiation and coalescence of sub-crack and the main crack. Note that voids were considered in nanoscale, the sub-crack tip thus seems to be sharpened. If the reverse plastic strain does not occur, the sharp crack tip maintains until an external load acts, as shown in (c-1). However, the reverse plastic strain occurs behind the growing crack tip; this contributes to not only enlarge CTOA but also slightly blunt the crack tip, as shown in (c-2). Obviously, this results in a lower crack tip stress due to crack tip blunt compared to that of a sharp crack tip.

3.4.1 The role of hydrogen in plastic strain distribution

As described in Fig. 3.13(c), the plastic strain distributions beneath the fracture surface in air and hydrogen environments were compared. Here, the differences in the magnitude of plastic strain, strain gradients, and the size of the corresponding region in air and hydrogen environment will be discussed in detail. First, note that the subcritical crack propagation was observed in hydrogen, which is represented by that higher load is required to propagate the crack in air compared to in hydrogen, as shown

in Fig. 3.2. Hence, corresponding to the areas analyzed by EBSD (in air: a = 1.4 mm; in hydrogen: a = 1.5 mm) the value of K in an air environment is larger than that in a hydrogen environment (in air: K = 20.8 MPam$^{1/2}$; in hydrogen: K = 17.2 MPam$^{1/2}$), which results in higher crack tip stresses and strains in an air environment. This explains that a higher magnitude of plastic strain was observed in an air environment. Secondly, it is clearly seen that the size of Region C in a hydrogen environment is narrow than that in an air environment. Region C is in the vicinity of the fracture surfaces. In a hydrogen environment, the highest stress acted ahead and near the crack tip due to hydrogen-induced dislocation emission from the crack tip [46, 72, 84, 95]. Hydrogen then concentrates on the maximum stress field [73]; the plastic deformation is localized in this field as a result of solute hydrogen facilitating dislocation activity, which is postulated as HELP mechanism [21, 22, 111]. Hence, it is speculated that the plastic strain of Region C is localized close to the fracture surfaces in a hydrogen environment.

Furthermore, as shown in Fig. 11(b) and Fig. 3.12(b), the size of Region B is independent of crack length (or magnitude of plastic strain). However, a narrower size of Region B is observed in a hydrogen environment, as shown in Fig. 3.13(c). On the other hand, crack propagation should consider the dynamic crack growth effect, where the velocity of crack growth and inertia play an essential role. However, the present crack propagation is stable accompany extensive plasticity; the effects of dynamic crack growth seem to be insignificant [89]. Hence, the role of hydrogen should be considered that it plays an essential role effected on the size of Region B. During the crack propagation, a high density of dislocations is observed near the fracture surface,

as shown in Fig. 3.14(c). Dislocations are considered as the hydrogen-trapped sites [112]. If the reverse plastic deformation occurs due to unloading and/or the tensile stresses (σ_{xx}) in the crack propagation direction reached the yielding strength of the material, as described the formation of Region B above, hydrogen at the trapped sites plays a role as HELP mechanism [22, 113]. Hence, reverse plastic deformation will occur in the region close to the fracture surface in a hydrogen environment.

3.5 Conclusions

Effects of hydrogen on macroscopic and microscopic features of crack propagation are investigated using a thin sheet of single-crystalline Fe-Si alloy. The centered-cracked specimens are tested under a sustained load in a hydrogen environment while under continuous stretching in an air environment. The results found the following:

- Despite significant reducing the specimen thickness, the crack growth mode of a thin specimen in air and hydrogen environments the same as that in thick specimens.
- The crack propagation is stable accompany extensive plasticity. The sequence of the crack propagation is similar in hydrogen and air environments and is presented as the following three stages: (1) crack tip blunting by dislocation emission from the crack tip; (2) micro-voids initiation ahead of the crack tip; (3) sub-crack initiation and opening process.
- The similarity was observed in the deformation microstructures beneath the fracture surface. Both microstructures were composed of three distinct

layers characterized by plastic strain gradients and dislocation densities. However, the characteristics of plastic strain and strain gradient in these regions are different, three layers were significantly affected by the environments, in which AIDE and HELP mechanisms are believed to be relevant.

- Unloading occurs during crack propagation, which causes reverse plastic strain in the regions behind the fracture surface. This contributes to not only enlarge CTOA but also slightly blunt the crack tip.

3.6 Figures

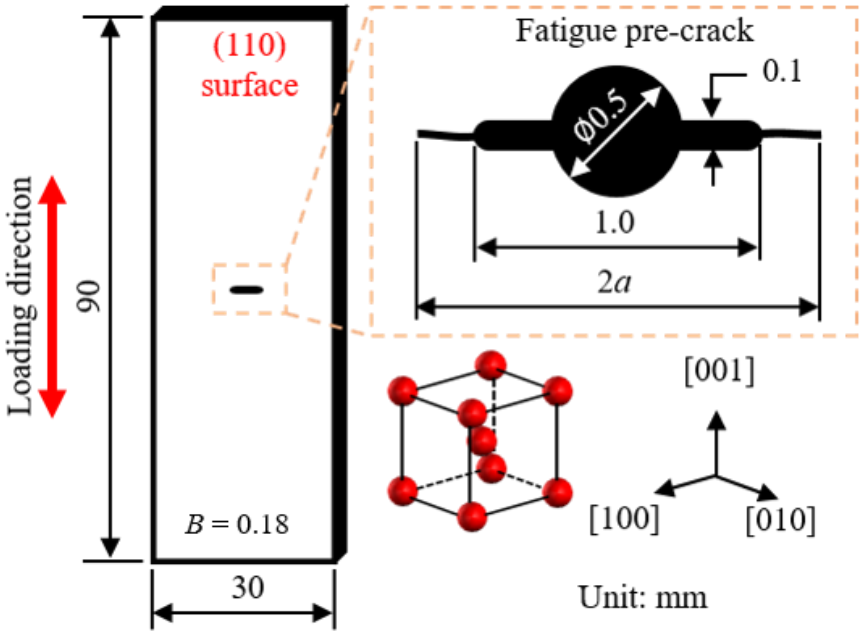

Fig. 3.1 Specimen geometry and crystallographic orientation. Configuration of the notch and fatigue pre-crack is indicated in the broken-line square. The fatigue pre-crack length (2a) was 2274 μm and 1970 μm for the specimens for hydrogen and air environment, respectively. The specimen thickness (*B*) is 0.18 mm.

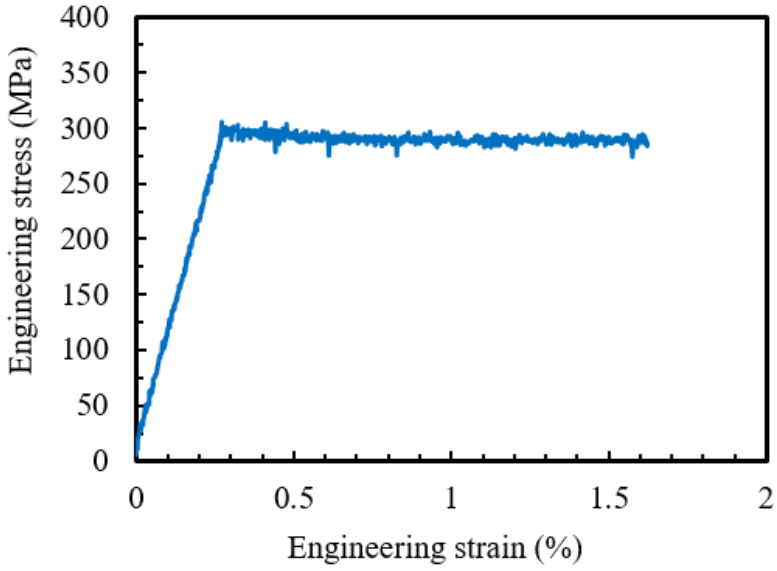

Fig. 3.2 Tensile test results for smooth specimen [52]. The specimen dimensions and crystallographic orientation which is used to conduct a tensile test are the same as those shown in Fig. 3.1; however, it has no notch.

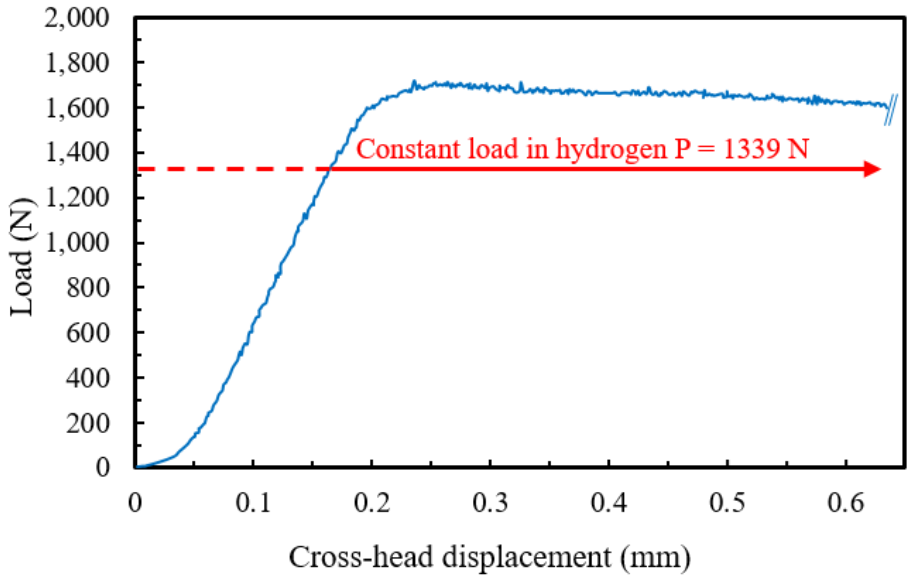

Fig. 3.3 A plot of the cross-head displacement versus the load in air environment; however, the constant load P = 1339 N in hydrogen environment (red color) is shown here for comparison.

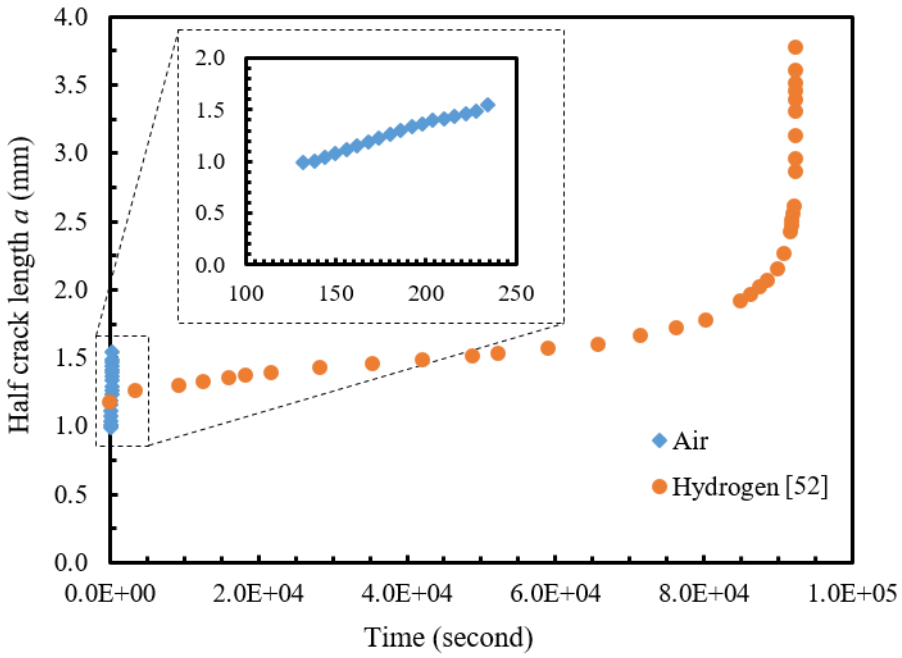

Fig. 3.4 Half crack length *a* as a function of time in air and hydrogen environments.

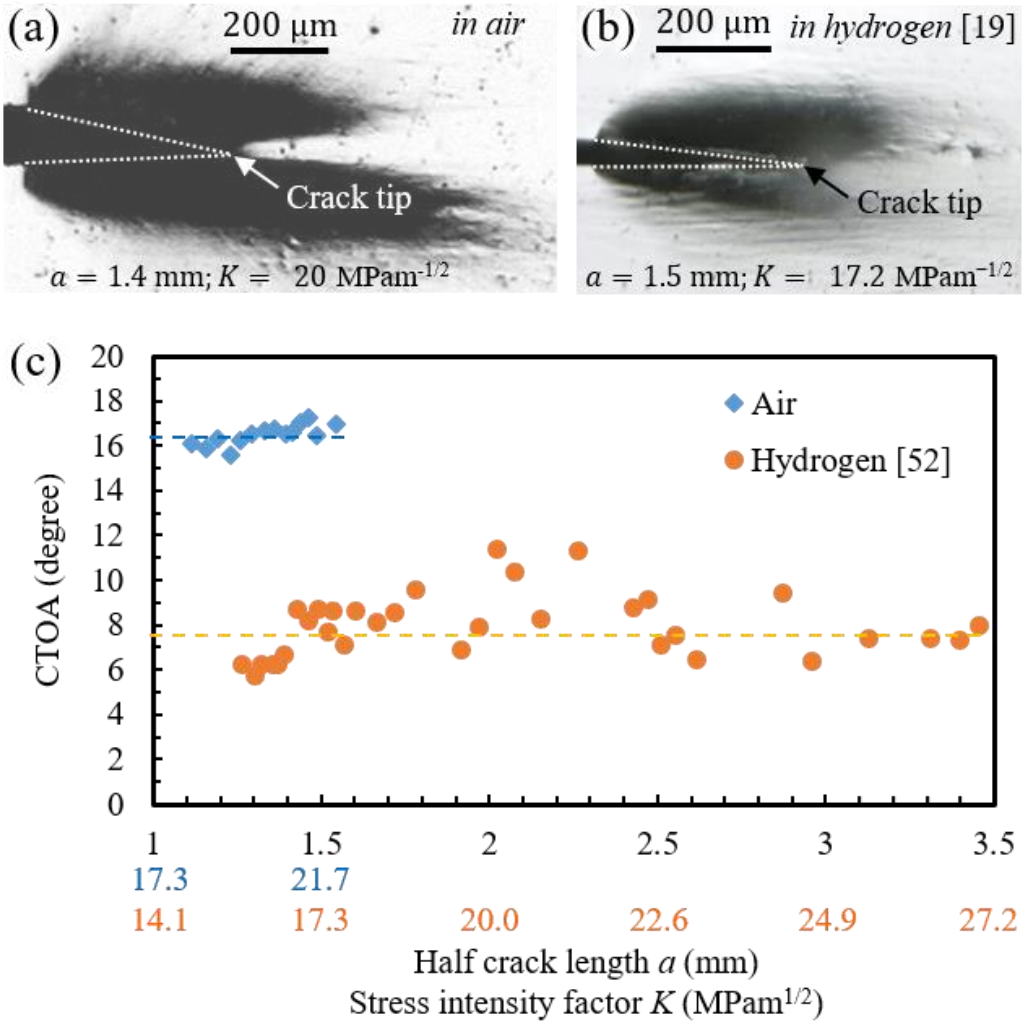

Fig. 3.5 (a) and (b) respectively show optical images of the crack propagation process in air and hydrogen environments. In these images, the dark regions around the crack wake, where the reflection of light illumination was scarce due to specimen necking (i.e. out-of-plane shear deformation), can be seen. Significant necking is observed in air. (c) shows a plot of CTOA versus half crack length a.

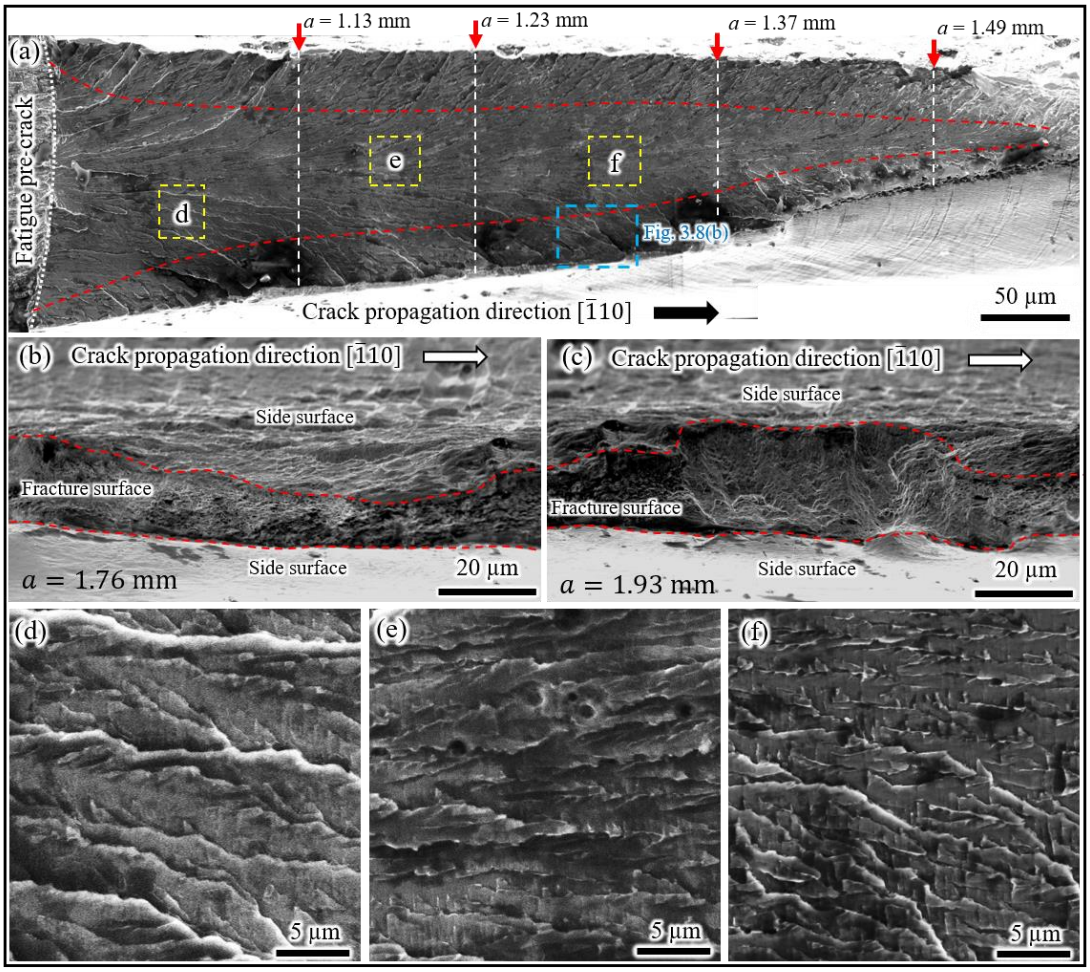

Fig. 3.6 SEM images of the fracture surfaces in an air environment; (a) early stage of the crack propagation; (b) and (c) later stage of crack propagation showing shear fracture surface; (d), (e), and (f) magnification observation of rectangle areas of (a) showing apparent striations. EBSD analysis will be performed in the middle of the specimen thickness at different crack lengths which are indicated by the red arrows.

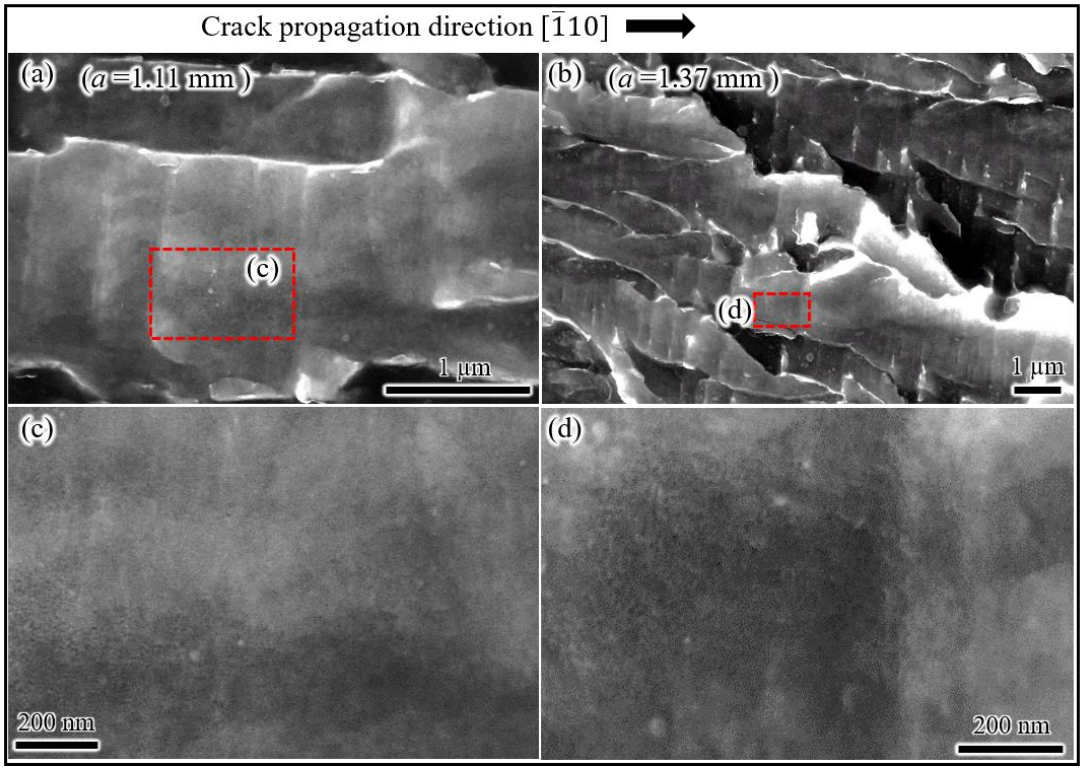

Fig. 3.7 SEM images in high magnification levels of the fracture surfaces in air showing facets between striations. Nano-dimples can be seen in (c) and (d). The SEM images in high magnification levels of the fracture surfaces in hydrogen was shown in Fig. 2.3 in Chapter 2.

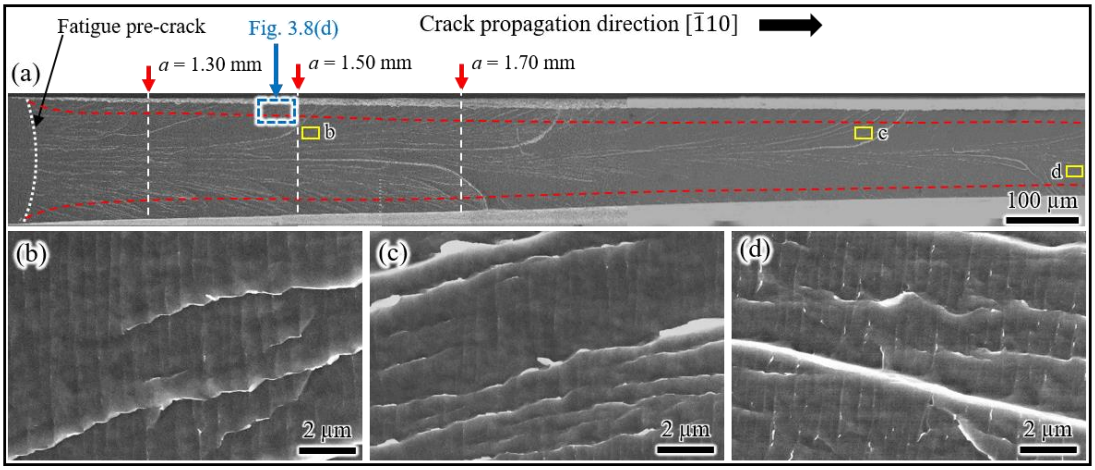

Fig. 3.8 SEM images of the fracture surfaces in a hydrogen environment; (b), (c), and (d) magnification observation of rectangle areas of (a) showing apparent striations. EBSD analysis will be performed in the middle of the specimen thickness at different crack lengths which are indicated by the red arrows.

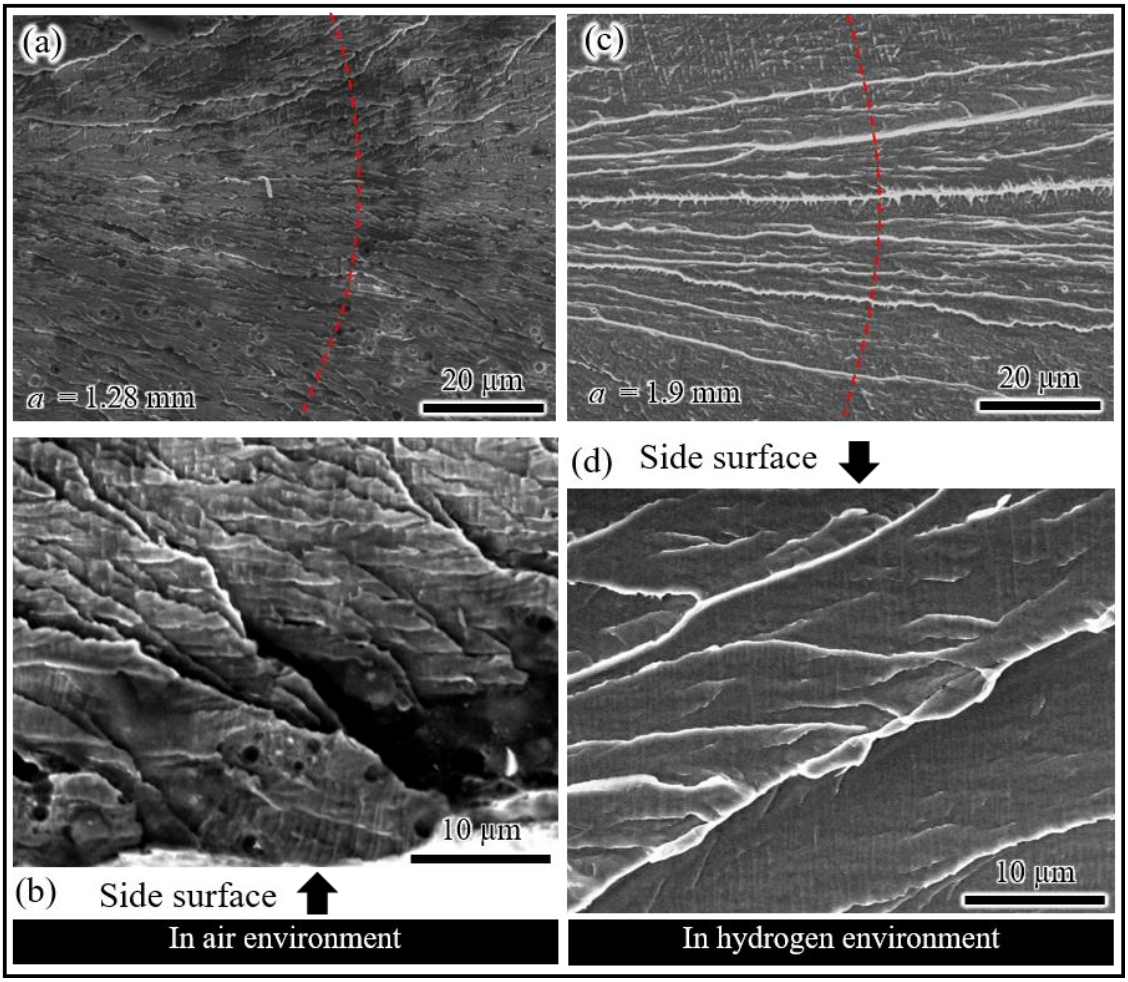

Fig. 3.9 SEM images showing the traces of the crack propagation process in (a) air and (c) hydrogen environment; striations on the shear slip regions of the fracture surfaces (near the side surface) in (b) air and (d) hydrogen environment.

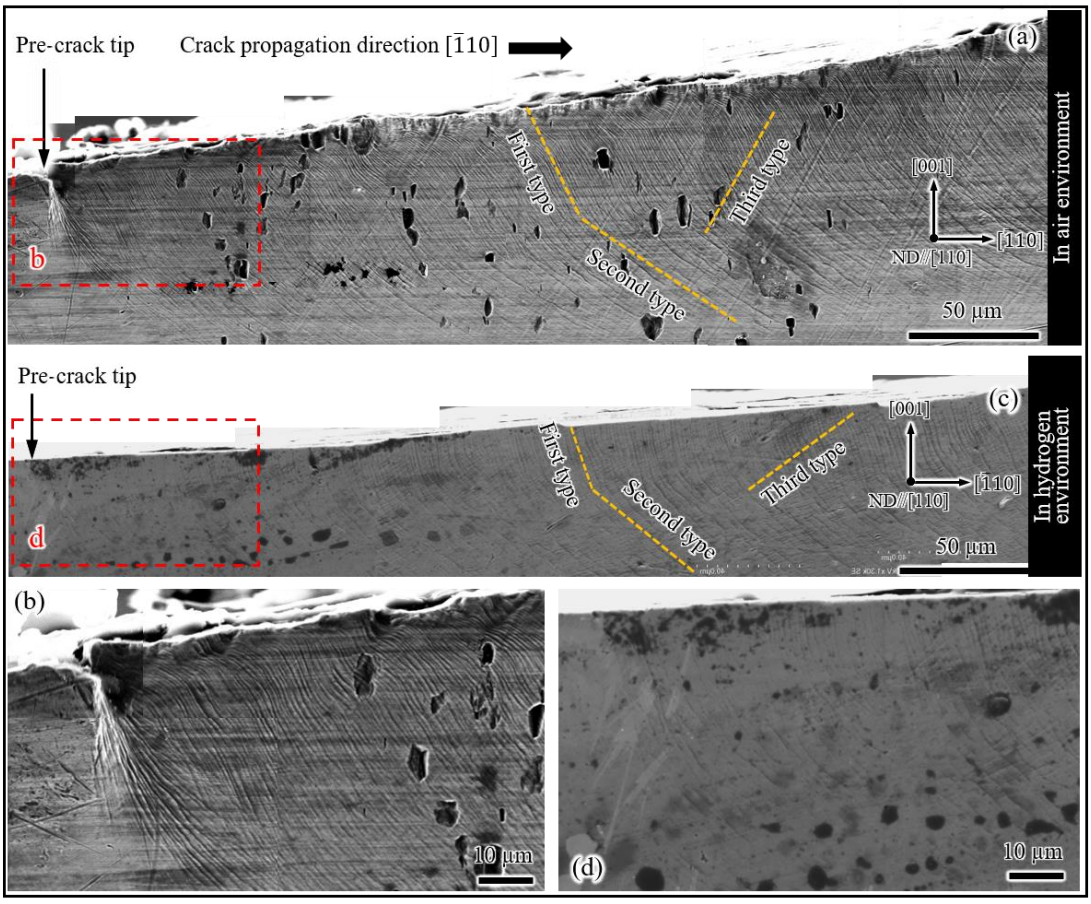

Fig. 3.10 SEM images of the side surfaces show slips (out-of-plane shear deformation) and the initial crack tip of the specimens tested in air (a, b) and hydrogen (c, d) environments. Slip traces near the edge of the fracture surfaces in (a) have a wave shape instead of a straight line which is the common shape of slip lines. It is speculated that significant lattice rotation occurs due to the extensive plastic deformation near the crack tip side surfaces during the crack propagation in air. Also, cross slip is speculated to be relevant when the screw component of dislocations propagates to the side surfaces, which results in the wave shape of slip lines.

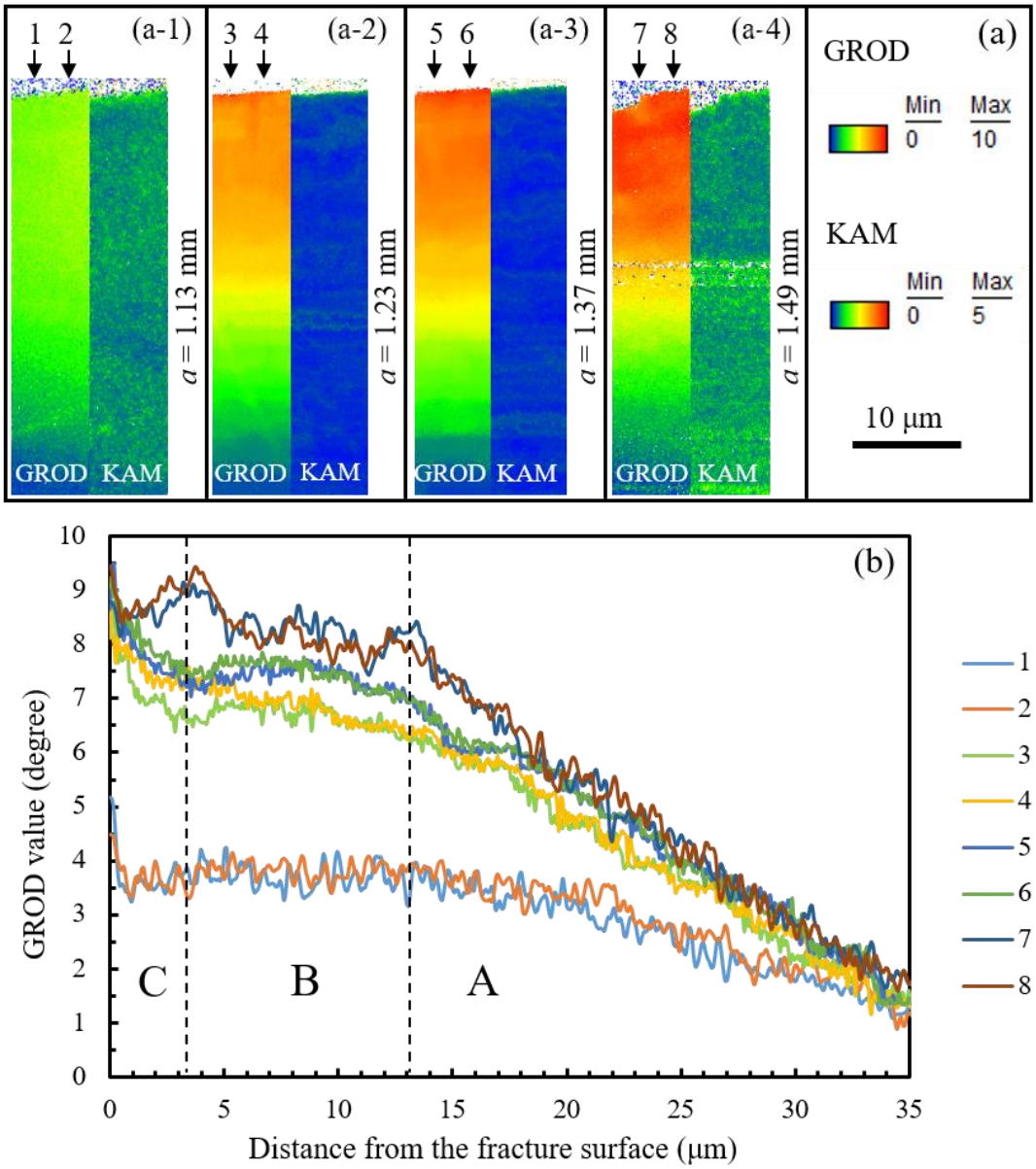

Fig. 3.11 (a) GROD and KAM maps investigated at different crack lengths of the specimen tested in air; (b) Misorientation profile depicted from EBSD measurements along the loading direction [001], which is indicated by arrows in (a).

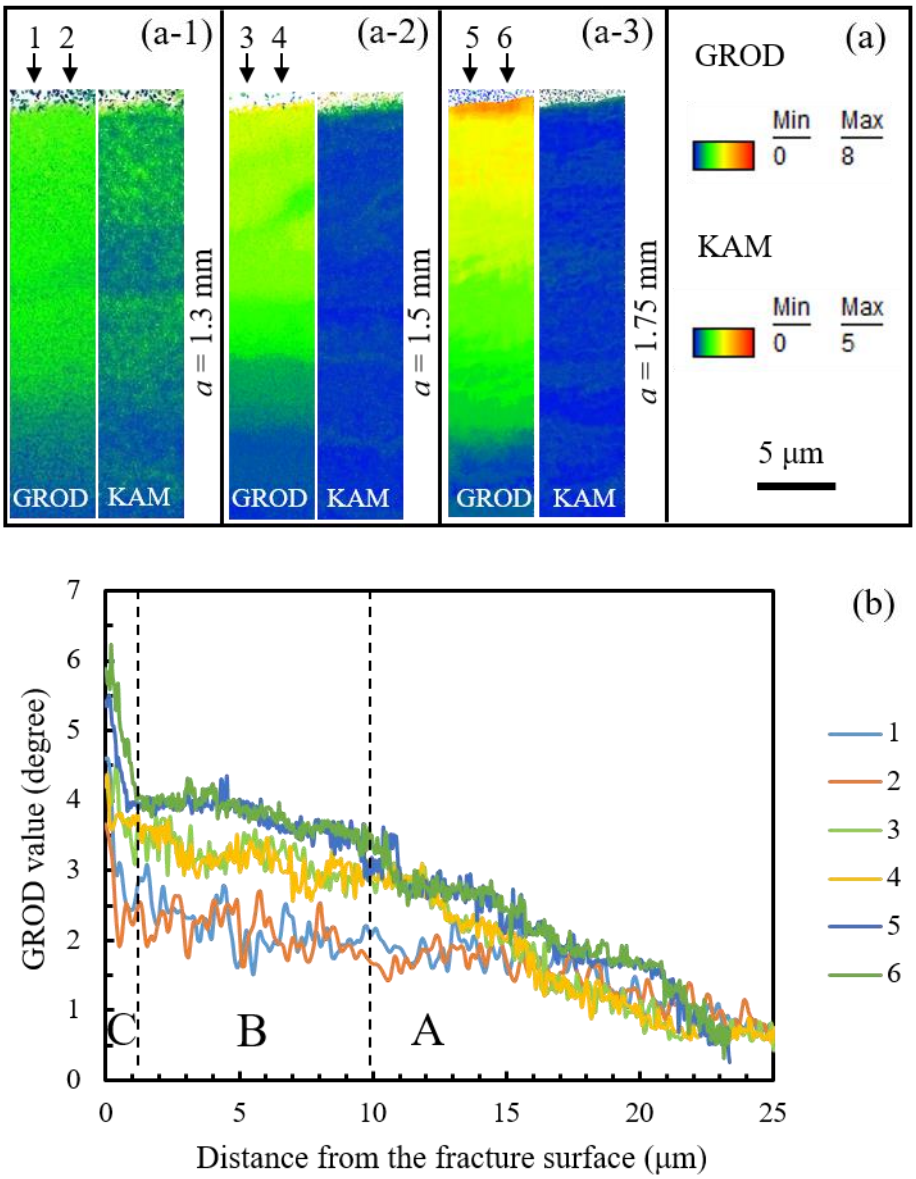

Fig. 3.12 (a) GROD and KAM maps investigated at different crack lengths of the specimen tested in hydrogen; (b) Misorientation profile depicted from EBSD measurements along the loading direction [001], which is indicated by arrows in (a).

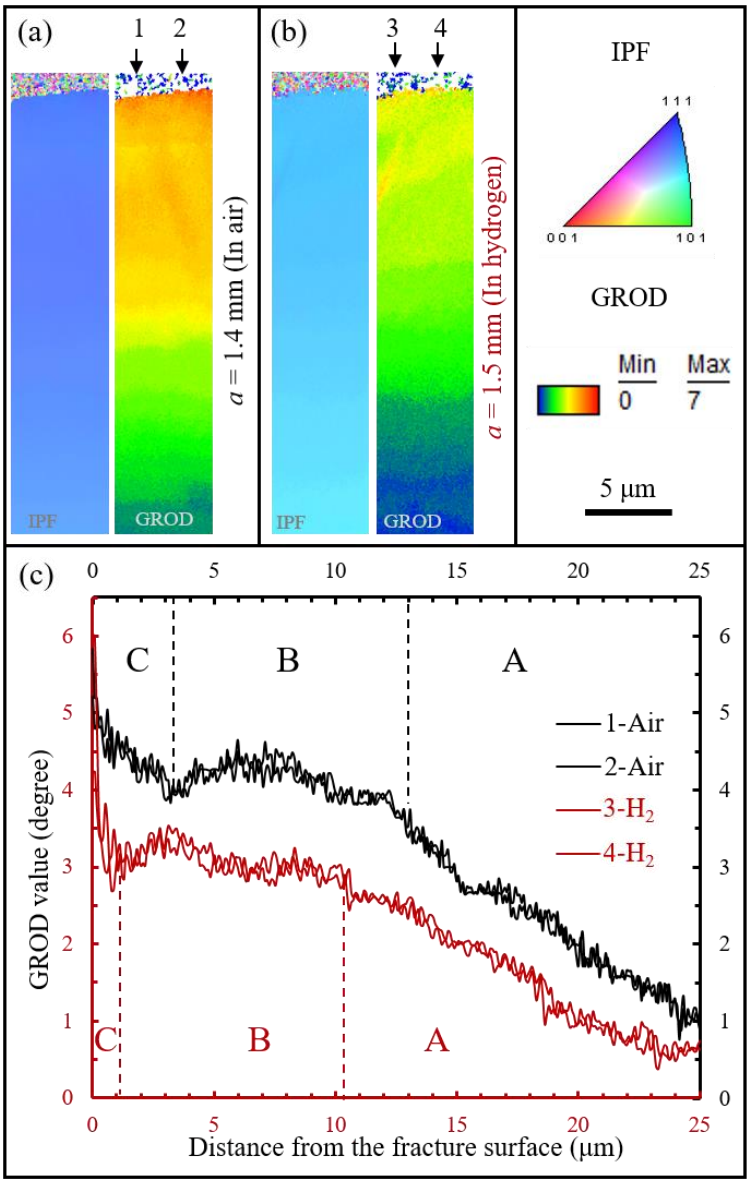

Fig. 3.13 (a) and (b) show IPF and GROD maps investigated at a relative same crack length in air and hydrogen, respectively (in air: a = 1.4 mm, K = 20.8 MPam$^{1/2}$; in hydrogen: a = 1.5 mm K = 17.2 MPam$^{1/2}$); (c) Misorientation profile depicted from EBSD measurements along the loading direction [001], which is indicated by arrows in (a) and (b).

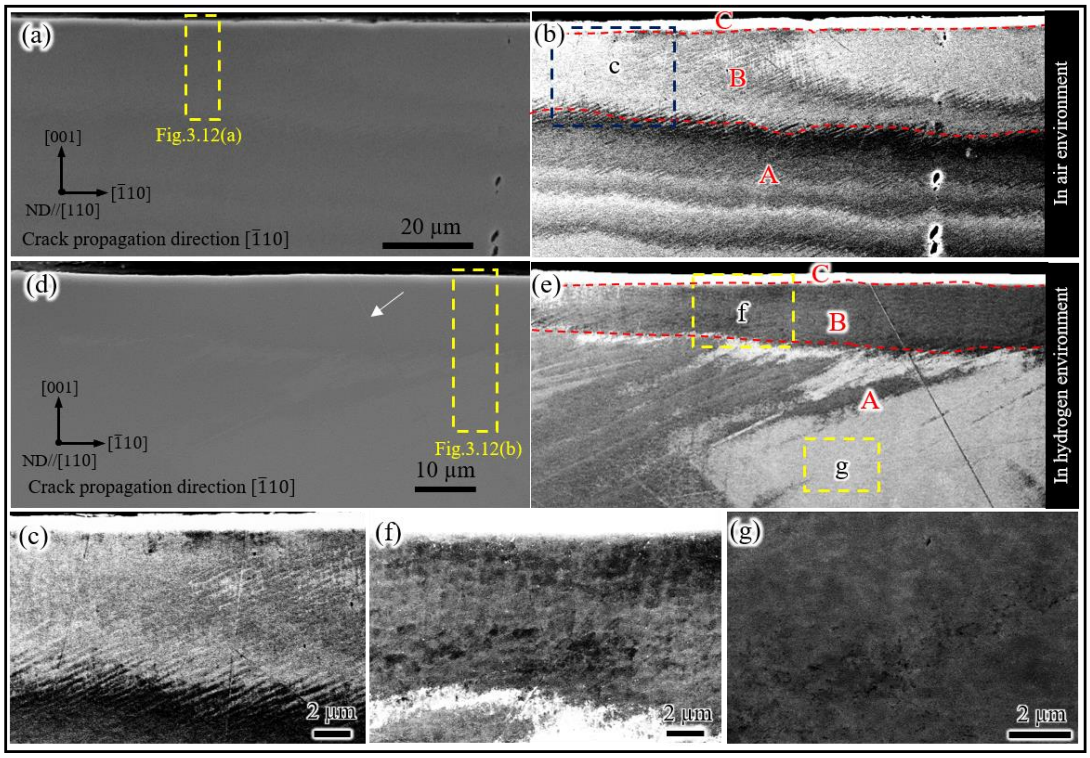

Fig. 3.14 The cross-sectional SE and ECC images showing the polished surfaces and the dislocation patterns in the middle of the specimen thickness in air (a, b, c) and hydrogen (d, e, f, g) environments.

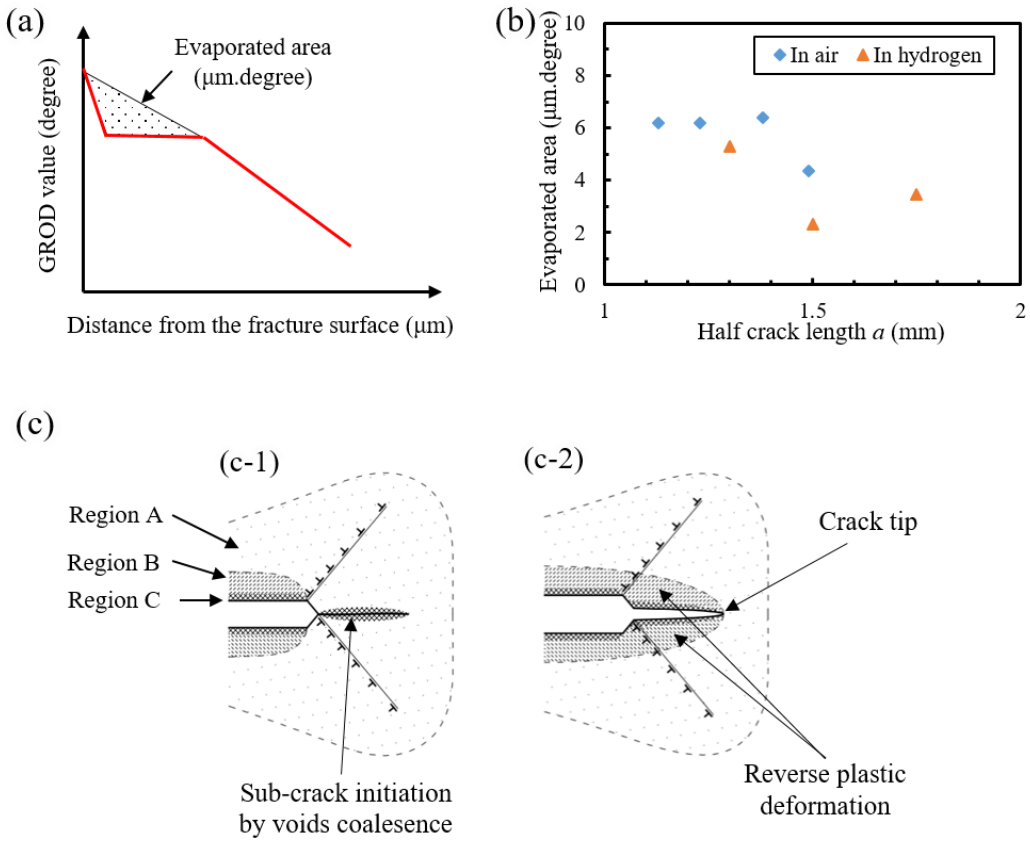

Fig. 3.15 (a) A schematic illustrating the tendency of plastic strain gradients underneath the fracture surface and showing a triangle-dotted region represented the "evaporated" area due to the reverse plastic deformation; (b) the measurements of "evaporated" areas at different crack lengths in air and hydrogen environments; (c) a schematic illustrating effect of the reverse plastic deformation on the CTOA and crack tip geometry; (c-1) sub-crack initiation; (c-2) coalescence of sub-crack and main crack, and the crack tip is slightly blunted by the reverse plastic deformation.

CHAPTER 4. Striation Spacing Characteristics and Role of Time

4.1 Introduction

The cracked bodies of iron-based alloys subject to a sustained load (the remote stress is far below yielding strength of materials) in an air environment; only crack blunting was observed [50]. In contrast, under the sustained load, crack growth was observed in a hydrogen environment, as reported in previous studies [16, 51, 67, 69, 74, 114]. Surprisingly, in most of these studies, despite the crack growth process is brittle or ductile, the crack grows discontinuously. The discontinuous crack growth was demonstrated by acoustic emission detection [68, 72], and fractographic observations [25, 115]. Related fractographic observations, the crack propagation left striations on the fracture surfaces, in which striations represent the traces of crack growth and arrest during propagation. Surprisingly, striation spacing was constant [25, 50-52, 67-69, 114].

Most of the above studies performed experiments using thick specimen (from 1.6 mm to 12.7 mm). Hence, hydrogen effects would have occurred predominantly under plane strain conditions [50, 71]. Presently, as shown in Chapters 2 and 3, despite significantly reducing specimen thickness, sub-critical crack propagation still occurred. It is well known that reducing the specimen thickness can decrease the stress tri-axiality ahead of the crack tip. This not only increases crack tip plastic strain but also

decrease hydrogen concentration ahead of the crack tip. Hence, this can affect the hydrogen embrittlement process. Also, discontinuous crack propagation occurred even testing conditions are under increasing load in an air environment. Comparing to continuous crack growth, the discontinuous crack growth results in a lower crack growth rate. Hence, it takes a longer time for the crack to reach a critical length where the unstable rupture occurs. On the other hand, as presented in Chapter 3, when the crack arrests extensive slips emitted from the crack tip in the air, which not only causes shielding effects on the crack tip [51, 116] but also absorbs more energy. In other words, this creates a rising crack-growth resistance curve. Moreover, the crack tip stresses and strains increase during the crack propagation, the amount of crack propagation should be increased as crack length increases. However, as presented in previous studies and Chapters 2 and 3, the amount of crack propagation (striations) is independent of the crack length, which is contrary to the concept of fracture mechanics. Hence, these motivate us to find out aspects that related discontinuous crack propagation and the crack-length independence of the crack propagation amount.

In this chapter, the microscopic feature of crack propagation in air and hydrogen in single-crystalline Fe-Si alloy was first investigated by ECCI and EBSD. These analyses were also aided by SEM fractography. Also, the dislocation structure of specimens, which are a short distance of crack propagation and stationary crack specimens, is investigated by ECCI in detail. The aspects that related to the discontinuous crack propagation, constant striation spacing, and the effects of HE on these phenomena will be then elucidated. Furthermore, the role of time in delayed crack propagation and sources of hydrogen are discussed.

4.1 Experimental procedure

Four specimens that have the same geometry and crystallographic orientation are used to conduct a sustained load in hydrogen and under continuous stretching in an air environment are shown in Table 1. The crack propagation tests in hydrogen (specimen 1) and in air (specimen 2) were introduced in Chapters 2 and 3, respectively.

For specimens 3 ($2a$ = 1.60 mm) and 4 ($2a$ = 1.64 mm), the testing condition is the same as that of specimen 2 (section 3.2 Experimental procedure in Chapter 3). Specimen 3 is used to conduct a short crack propagation, in which the cross-head displacement stops at 0.2 mm (P = 1752 N, $2a$ = 1.90 mm, K = 17.9 MPam$^{1/2}$), and then unload. Specimen 4 is subjected to a load of P = 1615 N, $2a$ = 1.64 mm, K = 15.3 MPam$^{1/2}$), and then unload (a small amount of crack growth by blunting is observed). The plot of cross-head displacement versus the load of the four specimens is shown in Fig. 4.1. Noted that the unloading process of specimen 3 did not record, which is a misses.

After the test, the topologies of the fracture surfaces and the side surfaces of the specimens were observed in detail by field emission scanning electron microscopy (SEM) at an accelerating voltage of 15 kV and 30kV. In order to investigate the plastic strain distribution and dislocation structure inside of specimens, the specimens were first mounted in the resin. Secondly, the material is removed step by step by mechanically grinding with silicon carbide grinding paper P1500 and P4000. Mechanical polishing with 9 μm and 3 μm monocrystalline diamond is then followed. Finally, mechanical polishing was performed using 50 nm colloidal silica. Subsequently, the plastic strain distribution was analyzed by EBSD measurements at

15 kV with the beam step size of 100 nm, and the dislocation structures were investigated by ECCI at an accelerating voltage of 30 kV.

4.3 Results

4.3.1 Fractographic investigation

It is noted that this section shows the results of the fractographic observation of the fracture surfaces on the right-hand side of the notch of specimens 1 and 2.

Overview of the whole fracture surfaces of specimens 2 (in air) and 1 (in hydrogen) is shown in Fig. 4.2. Note that the magnified SE images of the fracture surfaces, which are outlined by the yellow rectangles in Fig. 4.2, are shown in Fig. 4.3. The crack propagated in the $[\bar{1}10]$ direction along the (001) plane accompany extensive plasticity in both air and hydrogen environments. In air environment, the crack propagation which corresponds to mode I crack propagation is observed in the early stage of crack propagation (flat fracture surface in the central region and shear fracture near the specimen side surfaces), while the shear fracture is observed in the later stage, as shown in Fig. 4.2(a). In contrast, the stage that shear fracture occurred on the whole fracture surface is not observed in hydrogen, the model I crack propagates until unstable crack growth occurred. Corresponding to the mode I crack propagation, overall of the fracture surfaces in air and hydrogen environments is as river-like markings and is apparently continuous, which is similar to that found in thicker specimens with the same orientation, as reported in previous studies [50, 51, 69]. Also, the thickness of the regions near the fracture surfaces becomes thinner along the crack propagation path (from right to left); however, a significant reduction of the region

near the fracture surfaces is observed in an air environment. This can be explained as follows. Plane stress conditions dominate regions near the crack tip side surfaces, out-of-plane shear deformation (necking) thus occurs. Also, during the crack propagation, the crack tip stress and strain increase as the crack length increases. This results in increasing the degree of necking during crack propagates. Furthermore, the subcritical crack propagation was observed in hydrogen, which is represented by that higher load is required to propagate the crack (at the same crack length) in air compared to in hydrogen, as shown in Fig. 4.1. Hence, at the same crack length, significant necking was observed in air.

In a higher magnification level, Fig. 4.3(a) and (b) show striation patterns the fracture surfaces at different crack lengths in air and hydrogen, respectively. The striation lines are perpendicular to the crack propagation direction $[\bar{1}10]$. The striation spacing is constant during the crack propagation. However, the wider striation spacing is observed in air. The striation spacing is about 0.65 μm in air and about 0.40 μm in hydrogen. The striation patterns, constant striation spacing, and crack propagation direction in the present study are the same as those observed in thick specimens in previous studies [50, 51, 69, 94, 114, 115], where the same material and crack orientation were used to conduct the delayed crack propagation tests in a hydrogen environment. Moreover, the SE images taken in the shear fracture regions (near the side surface) are shown in Fig. 4.4. Interestingly, striation patterns can be seen in those images. Striations seem to stretches from one side to the other and have a convex shape toward the crack propagation direction as outlined by red dashed lines in Fig. 4.5. Therefore, the striations observed in the shear fracture regions are to accommodate the

crack front during the crack propagation. However, local striation lines were perpendicular to $[\bar{1}10]$ directions in both center parts and near side surfaces. Surprisingly, the striation spacing observed near side surfaces is larger than that observed in the center parts in hydrogen, while it is almost identical in those parts of the fracture surface in air. In hydrogen, the striation spacing observed near the side surfaces is about 0.6 - 1 μm, which is two or three times larger than the spacing in the center parts.

Based on the fractographic investigation, the characteristics of striation lines on the fracture surfaces in air and hydrogen environments are schematically shown in Fig. 4.6(a) and (b), respectively. Also, the striation morphology is also illustrated, as shown in Fig. 4.6(c), which were also reported by Takahashi et al. [52].

4.3.2 Observation of slip traces on the specimen side surfaces

Fig. 4.7(a) and (b) shows SE images of the side surfaces of the specimen 2 and 1, respectively. These images are observed on the right-hand side of the notch. Note that corresponding to the mode I fracture on the fracture surfaces, as shown in Fig. 4.2, these types of slip traces can be observed on the side surfaces. At first sight, slip lines can be seen clearly on the side surfaces, which indicate the occurrence of out-of-plane shear deformation and have been observed in the previous studies [51, 69, 73, 76]. Furthermore, extensive slip traces are seen in air. This again demonstrates that significant necking was observed in air (considerable reduction of the regions near the fracture surfaces in air, as shown in Fig. 4.2). Three types of slip traces are observed. These traces are indicated by dashed lines that are painted in different colors. Higher magnified SE images of the side surface, as shown Fig. 4.8, which were taken in the

outlined regions in Fig. 4.7, show clearer slip traces. These slip traces are the same as those presented in Fig. 3.9 in Chapter 3, which were observed on the left-hand side of the notch.

Furthermore, slip traces on the side surface of the specimen 3 are shown in Fig. 4.9. Note that the specimen 3 was used to conduct a short crack propagation in an air environment. Fig. 4.9(a) shows crack on the right-hand side of the notch, which the loading was stopped at the crack length of $2a$ = 1.90 mm and K = 17.9 MPam$^{1/2}$. Types 1 and 2 of slip traces can be observed in this figure. Anyhow, these traces are created by in-plane and out-of-plane deformation during crack propagation. Further investigation, such as ECCI and EBSD, needs to be performed to identify which states of stress contribute to creating each type of slip traces. The ECCI and EBSD observations will be presented in the latter parts.

4.3.3 Observation of dislocation structure

Before describing the dislocation structure observed inside the specimens (from Fig. 4.10 to Fig. 4.14), slip bands are represented by broken lines in different colors. In these figures, lines have the same color indicates the same slip band direction. Also, when comparing between slip bands (from Fig. 4.10 to Fig. 4.14) and slip traces on the specimen side surfaces (Fig. 4.7, Fig. 4.8, and Fig. 4.9), it is speculated that there is a consistency between them (lines have the same type and color). Moreover, some of the ECC images presented in Chapters 2 and 3 are also showed and described here. The average values of the spacing between slip bands shown from Figs. 4.11 – 4.14 are shown in Table 2.

4.3.3.1 Specimen 3

Fig. 4.10 shows a set of ECC images and EBSD analysis of the cross-sectioned surface after removing about 60 μm of material from the side surface. First, in Fig. 4.10(a), the surface orientation seems to be optimized to Bragg's condition in the center right-hand region, which is in dark contrast. The bright contrast in the other regions is caused by plastic strain evolution, owing to the orientation gradient associated with the presence of dislocations. At first sight, an overview of the dislocation structure shows the slipped and unslipped regions, which are indicated by the dark-broken lines, as shown in Fig. 4.10(a). It seems that the slip bands have been emitted from the crack tip and consistent with two directions $[\bar{1}11]$ and $[\bar{1}1\bar{1}]$, which are symmetrical about the crack plane, as shown in Fig. 4.10(b). This is confirmed by EBSD analysis that all $\langle 111 \rangle$ direction types are shown in Fig 4.10(c). These slip lines seem that it is consistent with Types 2 and 3 of slip traces, as shown in Figs 4.7, and Fig. 4.8. The possible slip systems corresponding to plane strain conditions and these slip directions are shown in Fig. 4.15, which are $\{112\}\langle 111 \rangle$ and $\{110\}\langle 111 \rangle$ slips. These slip systems are symmetrical about the crack plane. Interestingly, in the areas above (but far away) and below the crack plane, the appearance of "crossing lines" of dislocation structures can be seen. It seems that the intersection between slip bands, which are in $[\bar{1}11]$ and $[\bar{1}1\bar{1}]$ directions. This appearance can be seen clearly in the region below the crack plane shown in Fig. 4.10(d). A closer look into the "crossing lines" regions, Fig. 4.10(e) shows evidence of parallel bands ($[\bar{1}1\bar{1}]$ direction). It seems that the spacing between bands is approximately constant. Further observation in the unslipped regions below the crack plane, as outlined by the broken box in Fig. 4.10(b), the slip

bands which consists of $[\bar{1}11]$ slip direction (indicated by a blue-broken line) can be seen, while the slip bands consisted of $[\bar{1}1\bar{1}]$ slip direction cannot be observed, as shown in Figs. 4.10(f) and (g). Thus, the question arises whether these slips that the spacing between them is the same as those observed in the "crossing lines" regions (Fig. 4.10(d)), and whether these are activated ahead of the crack tip. This probably needs further discussion and evidence.

Furthermore, Fig. 4.11 shows a set of ECC images of the cross-sectioned surface in the same area of Fig. 4.10 after further removing (about 20 μm) material in the thickness direction. The slip bands emitted into two directions $[\bar{1}11]$ and $[\bar{1}1\bar{1}]$ are obviously observed, which are the same as those shown in Fig. 4.10(a). Also, the "crossing lines" regions can be observed in the areas above and below the crack plane. However, it is clearer than those shown in Fig. 4.10(a). A closer look into the "crossing lines" region near the fracture surface, Fig. 4.11(e) shows slip bands emitted from the crack tip in the region near the fracture surfaces and indicated by the red arrows. Interestingly, if the spacing between these bands takes into account, it is the same as the striation spacing observed on the fracture surface, as shown in Figs. 4.3(a) and 4.4(a). The spacing between bands, as shown in the solid-white box in Fig. 4.11(a), is measured; it is about 0.57 μm for Type 1 (red-broken line) and about 0.61 μm for Type 3 (blue-broken line). Further, the dislocation structure ahead of the crack tip is very turbid; it seems that high dislocation density is present, as shown in Fig. 4.11(b). However, it is speculated that it is probably contributed by plastic relax when the load is interrupted and slowly unload. Meanwhile, the cell structure can be seen in the region away from the crack tip, as shown in Figs 4.11(c) and (d).

4.3.3.2 Specimen 4

Fig. 4.12(a) shows slip traces at the crack tip side surface of the specimen 4. Types 2 and 3 of slip traces can be observed. Notably, Type 3 can be seen ahead of the crack tip, which cannot be found in specimen 3 (Fig. 4.9(a)). The vertical traces at the crack tip are the same as shown in Fig. 4.9(a), where considerable plastic strain occurs before crack propagation. The corresponding ECC images were taken after removing an amount of material (about 50 μm) from the side surface, which is shown in Fig. 4.12(b). The slip bands which are emitted in $[\bar{1}11]$ and $[\bar{1}1\bar{1}]$ directions are not observed. Only slip bands consistent with slip traces on the side surfaces are seen. Interestingly, as shown in Fig. 4.12(c), cell structure can be observed ahead of the crack tip, in which red arrows indicate some of the cells. Again, it is surprising that if the distance between these cells takes into account, it is equivalent to that of striation spacing.

4.3.3.3 Specimen 2

Fig. 4.13(a) shows the striation pattern on the fracture surface (a = 1.4 mm) on the left-hand side of the notch. The striation spacing is about 0.65 μm. Corresponding to this crack length, Figs. 4.13(b) and (c) show the ECC image taken in the middle of the specimen thickness. Note that these ECC images are the same as those shown in Fig. 3.13(b) (Chapter 3). There are some scratches indicated by red arrows in these images. First, “crossing lines” regions can be observed, as shown in Fig. 4.13(c). This region has a higher brightness contrast, which indicates a higher orientation gradient and dense dislocation between bands compared to the others. Two slip directions

indicated by red and blue dashed lines can be observed. These lines are probably the same as Type 1 and 3 mentioned in Figs. 4.9 to 4.12. However, Type 1 cannot be seen clearly. In contrast, Type 3 can be seen clearly and has constant spacing between bands. In the enlarged images of Fig. 4.13(b), the spacing between bands (blue-broken line) is about 0.72 μm. Hence, the spacing of striations and slip bands seems to be identical.

4.3.3.4 Specimen 1

Figs. 4.14(a) and (b) show striations in the middle and near the side surfaces (at the crack length a = 1.75 mm, left-hand side of the notch), respectively. Fig. 4.14(b) is the same as Fig. 2.2(d) in Chapter 2. In these images, striation spacing is about 0.4 μm in the center part, while it is larger (about 0.7 μm to 1.2 μm) near the side surfaces. Corresponding to this crack length, Figs. 4.14(c) and (d) show the ECC image taken near the side surface and in the middle of the specimen thickness. Figs. 4.14(c) and (d) are respectively the same as Figs. 2.3(b) and (d) in Chapter 2. ECC images near the side surface are shown in Fig. 4.14(c); the "crossing-lines" regions, which are the intersection between two different directions of slip bands are seen. The slip directions are also drawn in these images. In Fig. 4.14(c), The average spacing between bands (red-broken line) in the enlarged image is 0.66 μm, and the average spacing between bands (blue-broken line) in the red box is 0.71 μm. ECC images taken in the middle of the thickness are shown in Fig. 4.14(d); the "crossing-lines" regions cannot be seen near the fracture surface but can be seen in the region away from the fracture surface. Note that parallel lines near the fracture surfaces are caused by polishing. The similarities between these two images are that the spacing between slip bands and band

directions seem identical. Especially, the spacing between slip bands observed in the enlarged image of Fig. 4.14(c) is similar to the striation spacing shown in Fig. 4.14(b).

4.4 Discussion

4.4.1 Activated slips that contributed to the crack propagation

As the SEM images of fracture surfaces shown from Figs. 4.2 to 4.5, the crack macroscopically propagated in $[\bar{1}10]$ direction. This was presented in most of the studies that used the same material and crack orientation [50, 51, 69, 72, 114, 115]. Furthermore, even some studies [50, 51, 69, 72, 115] designed that crack propagates in [010] direction on (001) plane. The crack propagated macroscopically in [010] direction, but the local crack front and striation lines were perpendicular to two orthogonal [110] and $[\bar{1}10]$ directions, as shown in Fig. 4.16 [117]. Those studies were also analyzed slip systems that activated and contributed to crack propagation under plane strain conditions by experiments [49, 69, 100] and simulations [101], which used the same material and orientation and had tested in air and hydrogen. They reported that emission dislocations from the crack tip is on the $\{112\}\langle 111\rangle$ and/or $\{110\}\langle 111\rangle$ slip systems [49, 100, 101]. The proposed $\{112\}\langle 111\rangle$ and $\{110\}\langle 111\rangle$ slip systems are shown in Fig. 4.15. These slip systems are symmetrical about the crack plane. Note that the striation is formed by extensive slip at the crack tip. It is interesting that the traces of intersection between the slip plans of $(1\bar{1}2)[\bar{1}11]$ and $(\bar{1}12)[\bar{1}1\bar{1}]$ (shown in Fig. 4.15(a)) and the crack plane (001) lie in the [110] direction. Meanwhile, the traces of intersection between the slip plans of $(0\bar{1}1)$ $[\bar{1}11]$, (101) $[\bar{1}11]$, $(\bar{1}01)[\bar{1}1\bar{1}]$, and $(011)[\bar{1}1\bar{1}]$ slip systems (shown in Fig. 4.15(b)) and the crack plane (001) lie in the

[100] and [010] directions. Also, corresponding to [001] loading direction, Schmid factor (m) of $(1\bar{1}2)[\bar{1}11]$ and $(\bar{1}12)[\bar{1}1\bar{1}]$ slip systems (m = 0.471) is higher than that of $(0\bar{1}1)$ $[\bar{1}11]$, (101) $[\bar{1}11]$, $(\bar{1}01)[\bar{1}1\bar{1}]$, and $(011)[\bar{1}1\bar{1}]$ slip systems (m = 0.408). Coupled with the clear "crossing-lines" regions described above, it is hence suggesting that the $(1\bar{1}2)[\bar{1}11]$ and $(\bar{1}12)[\bar{1}1\bar{1}]$ slip systems mainly contribute to crack propagation in plane strain conditions. The "crossing-lines" regions were also observed by Tetelman et al. [118], and the $\{112\}\langle111\rangle$ slip systems were proposed that correlate with crack growth.

4.4.1 Proposed mechanism of discontinuous crack propagation

Based on microscopic observations of the fracture surfaces and side surfaces as well as observation of dislocation structure inside specimens, a model that demonstrates the discontinuous crack propagation in an air environment is proposed. The discontinuous crack propagation in a hydrogen environment is then discussed. Note that the mechanism of crack propagation in the air has been discussed in Chapter 3. In this section, why crack propagates discontinuously (propagation and arrest), and why the striation spacing is constant and independent of crack length are considered. The model is schematically presented as Fig. 4.17, and is explained as follows. As shown in Fig. 4.17(a), dislocations first emit from one side of the crack plane as loading increases, which is on $(1\bar{1}2)[\bar{1}11]$ slip. Large back stress thus shields crack tip on this side. Secondly, dislocation emission from the other side of the crack plane occurs, which is on $(\bar{1}12)[\bar{1}1\bar{1}]$ slip. Note that not only dislocations emitted from the crack tip but also numerous dislocation sources ahead of the crack tip are activated. The dislocations emitted at the crack tip contribute to crack advance but in a small

amount. In contrast, the dislocations activated ahead of the crack tip contribute to either open the crack tip or to generate strain ahead of the crack tip. Subsequently, multiple dislocations play a major role ahead of the crack tip, which causes the nucleation of voids [25]. The $(1\bar{1}2)[\bar{1}11]$ and $(\bar{1}12)[\bar{1}1\bar{1}]$ slip bands or dislocation cells form ahead of the crack tip. When sub-crack coalescence with the main crack, the new crack may propagate further due to the external load that continues to increase. The crack then meets slip bands or cell walls which were formed ahead of the crack tip. Note that numerous dislocations exist within slip bands or cell walls. Work hardening hence occurs within slip bands or cell walls; crack tip plastic deformation becomes difficult. As a result, the crack propagation is obstructed and the external load has to increase further to deform the crack tip and then propagate the crack. These cycles repeat and result in crack propagation. The results presented in previous studies are reported as follows. Rice [109] performed an asymptotic analysis of the crack tip stress and deformation field in plane-strain conditions. The material model is elastic-ideally plastic single crystals, and the crystals were assumed to have a limited set of possible slip systems. Each slip system has a critical resolved shear stress for plastic flow. The crystal orientation was the same as that in the present specimen. The results showed that specific $(1\bar{1}2)[\bar{1}11]$ and $(\bar{1}12)[\bar{1}1\bar{1}]$ slip systems acts ahead of the crack tip. As presented by Lii et al. [117], they investigated slip traces and dislocation structure ahead of the crack in Fe-Si samples, which were subjected to sustained load in hydrogen. The crack propagation process has been confirmed by the acoustic emission technique to be brittle. The striation, which has constant spacing (1 μm), was observed on the fracture surfaces. They found that clear slip traces were formed in front of the crack tip at an early stage of deformation (before crack starts to propagate).

Also, regular 1 μm size of cells, which are so-called low-energy dislocation structure [119, 120], formed about 20 μm ahead of the crack tip. Hence, they hypothesized that the crack initiation, arrest, and striation spacing were involved in these cells.

In a hydrogen environment, the discontinuous crack propagation is discussed as follows. It is known that higher hydrostatic stress acts (and/or maximum stress acts ahead of the crack tip due to dislocation emission) in the center region, hydrogen therefore accumulates and facilitated the crack propagation as a model presented in Chapter 2. However, the striation spacing observed in hydrogen is also constant. During the crack propagation, crack tip stresses and strains increase as the crack length increases. Thus, hydrogen facilitates crack propagation in a constant amount is unreasonable. Lunarska et al. [121, 122] conducted the tensile test of both single-crystalline and polycrystalline iron specimens (charged and uncharged hydrogen). They reported that the spacing between slip bands was also affected by hydrogen, in which a shorter spacing was observed in charged specimens. As the observation of dislocation structure in the middle of the specimen thickness shown in Fig. 4.14(d), the “crossing-lines” region cannot be observed near the fracture surfaces. Hence, it is considered that hydrogen effects on slip behavior in the specimen interior. In hydrogen, finer slip bands and narrower spacing between them compared to those of the specimen tested in the air are formed ahead of the crack tip. The discontinuous crack propagation and the constant striation spacing can be explained the same as those in air.

In contrast, plane stress conditions act near the side surfaces. Hence, the role of hydrogen that induced crack propagation as in the specimen interior is insignificant

due to the lack of high hydrogen concentration [50]. Coupled with the investigation of the fracture surfaces, side surfaces, and dislocation structure underneath the fracture surfaces, as well as the comparison of those in air and hydrogen environments, the crack propagation near the side surfaces of specimens tested in hydrogen is identical to that in air. However, there is an interaction between discontinuous crack propagation near side surfaces and in the center part. Under the present sustained load, if hydrogen does not present, the crack will not propagate. Only crack tip blunting can be observed [50]. However, hydrogen existed and induced subcritical crack propagation as proposed in Chapter 2. It seems that the crack propagation in the center part is about several cycles while near the side surface lagged behind. Then the effective stresses near the side surfaces increase due to increasing crack length in the center part. Thus, the effective stresses are sufficient to propagate the crack in one cycle near the side surfaces. On the other hand, the slower propagation of the crack near the side surface shields crack tip stresses in the center part. The shielding effect is more pronounced if the crack propagation is much faster in the center part, and can be seen clearly in thicker specimens [50, 51]. In microscopic observation, more number of cycles of the crack propagation, but the shorter spacing of striations is observed in the center part compared to those near the side surfaces. Hence, the overall crack propagation rate in these regions seems identical.

Moreover, in the present material and orientation, the slip bands/cells formed ahead of the crack tip are characterized by that the spacing between them is constant irrespective of crack length. In conjunction with the mechanism of discontinuous crack propagation presented above, it is reasonable to explain the constant striation spacing

was observed. However, the reason for explaining why the spacing between slip bands/cells is constant despite the crack tip stresses and strains increase needs to study further.

4.4.3 Hydrogen sources and importance of time in delayed crack propagation

In hydrogen-induced delayed crack propagation, time is necessary for hydrogen accumulated and reached a significant amount at the crack tip to facilitate crack propagation [51]. As mentioned in Chapter 2, log (da/dt) linearly increases with the crack tip plastic zone [52]. Also, the striation spacing (da) is constant and independent of crack length. Hence, it is concluded that the velocity of hydrogen enrichment at the crack tip increases. During the crack propagation, the crack tip stress and strain increase. Hence, it is speculated that not only the stress-driven diffusion but also the role of dislocations such as dislocation transport [92] probably accelerated the accumulation of hydrogen to the crack tip. Regarding to dislocation transport [92], the newly created dislocations at/ahead of the crack tips play as hydrogen traps; dislocations (especially, mobile dislocations) subsequently accumulate hydrogen in the near-surface region and carry it further into the deforming regions.

It is well known that hydrostatic stress is a controlling factor related to stress-driven diffusion [41]. Basically, hydrostatic stress contributes to volume change (volumetric expansion), where it acts. Hydrogen will diffuse to and accumulate at the high hydrostatic stress region. Ahead of the crack tip, the peak of hydrostatic stress at the elastic-plastic boundary [41, 42]. However, when dislocations emit from the crack tip due to AIDE, the crack tip stresses redistribute. For instance, the maximum stress acts at a distance of about 30 nm ahead of the crack tip due to dislocation emission

[72]. Hence, there are two peaks of hydrostatic stress ahead of the crack tip. The first is in the vicinity of the crack tip, and the second is at the elastic-plastic boundary, in which the first one plays a major role in facilitating crack/void formation ahead of the crack tip. Furthermore, there are two important sources of hydrogen, which come from the crack tip and the second peak of hydrostatic stress. Note that a region, which has high hydrogen concentration driven by the second peak of hydrostatic stress, always exists ahead of the crack tip during the crack propagation. The crack goes through this region when it propagates. Hence, hydrogen at the second peak of hydrostatic stress is considered that it significantly contributes to accelerating hydrogen accumulation in the first peak.

4.5 Conclusions

The microscopic feature of crack propagation in air and hydrogen in single-crystalline Fe-Si alloy was investigated by ECCI and EBSD. These analyses were also aided by SEM fractography. The centered-cracked specimens are tested under a sustained load in a hydrogen environment while under continuous stretching in an air environment. The results explicitly revealed the following:

- Striation is formed by extensive slips emitted from the crack tip, which are mainly contribution of specific $(1\bar{1}2)[\bar{1}11]$ and $(\bar{1}12)[\bar{1}1\bar{1}]$ slip systems. Discontinuous crack propagation is mainly caused by the interaction of the crack and $(1\bar{1}2)[\bar{1}11]$ and $(\bar{1}12)[\bar{1}1\bar{1}]$ slip bands/cell walls formed ahead of the crack tip. These slip bands/cells are characterized that the spacing between slip bands is constant and independent of crack length. Hence,

striation spacing is the same as that of slip bands/cells ahead of the crack tip.

- During the crack propagation, hydrogen diffuses to and accumulates at the maximum stress field ahead of the crack tip to facilitated damage initiation. Stress-driven diffusion and dislocation transport are leading factors that contribute to accelerating the diffusion speed of hydrogen. Hydrogen existed in the second peak of hydrostatic stress is postulated that it is the primary source of hydrogen, which contributes to accelerating hydrogen accumulation in the first peak.
- Hydrogen is speculated that it affects slip behavior, in which it induces a shorter spacing between slip bands ahead of the crack tip.

4.6 Tables and Figures

Table 4.1 Pre-crack lengths of specimens and the testing purposes

Specimen No.	**Pre-crack length 2*a* (mm)**	**Purposes of tests**	**Note**
1 [52]	2.27	Delayed crack propagation test (tested in hydrogen)	Presented in chapters 2 and 3
2	1.98	Crack propagation test (tested in air)	Presented in chapter 3
3	1.60	Unloading at crosshead displacement of 0.2 mm (tested in air)	Small amount of crack growth (Δa = 150 μm) (P = 1752 N, K =17.9 MPam$^{1/2}$)
4	1.64	Unloading at P = 1615 N (tested in air)	No crack growth (K = 15.3 MPam$^{1/2}$)

Table 4.2 The average spacing between slip bands

Figures	Type of slip lines	Average spacing
4.11	Type 1 (red-broken line)	0.57 μm
	Type 4 (blue-broken line)	0.61 μm
4.12	Type 4 (blue-broken line)	0.72 μm
4.13	Type 1 (red-broken line)	0.66 μm
	Type 4 (blue-broken line)	0.71 μm

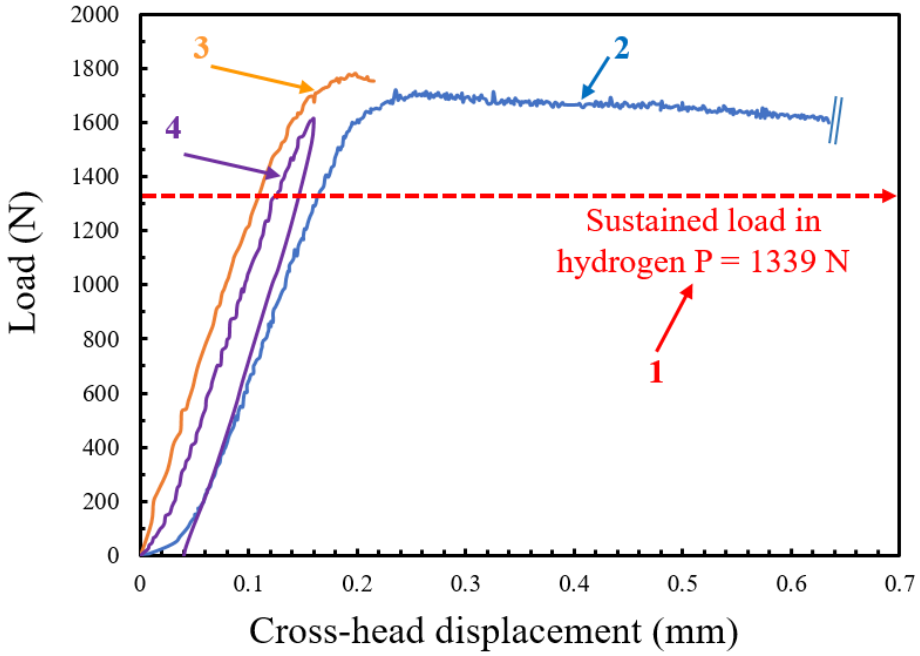

Fig. 4.1 Plots of crosshead displacement and the load of the specimens tested in air environment. Each color (text, lines, arrows) represents each specimen and its information (see Table 1). For a specimen 3, it is hard to identify crack initiation and crack length during crack propagation due to the effect of the painting layer on the specimen surface (DIC method is used for this specimen). Also, the unloading process of specimen 3 did not record, which is a misses.

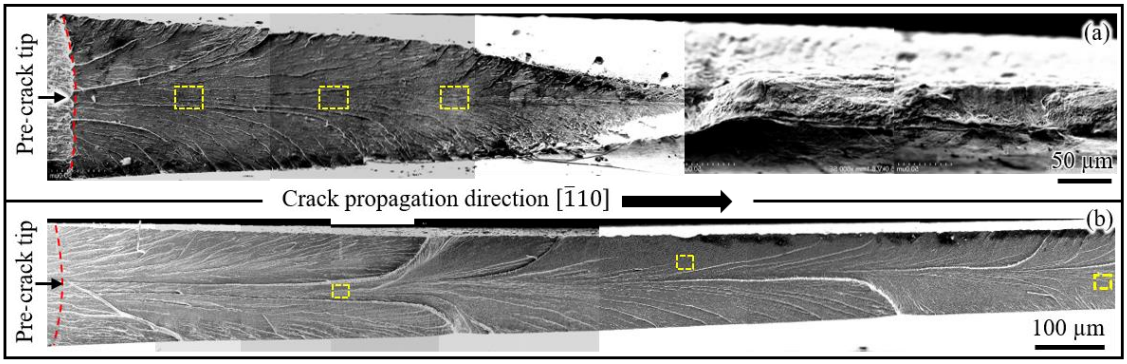

Fig. 4.2 Low-magnification SEM images of fracture surfaces on the right-hand side of the notch (a) in air (specimen 2) and (b) in hydrogen [52] (specimen 1). The yellow rectangles indicate the regions observed in higher magnification levels of fracture surfaces, which are shown in Fig. 4.3.

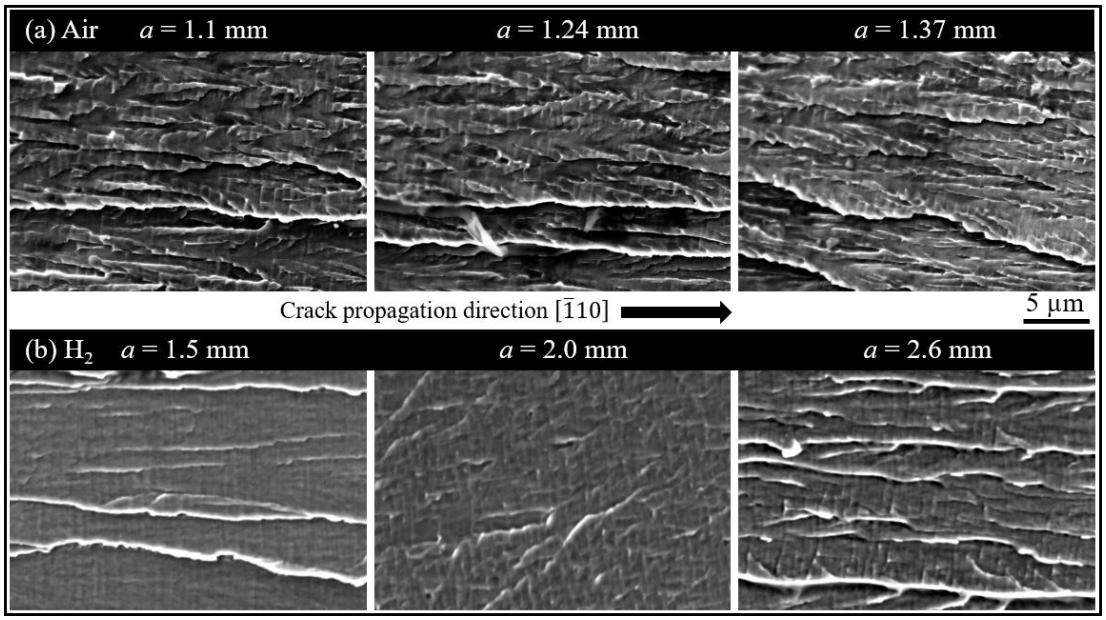

Fig. 4.3 High-magnification SEM images observed in the center of fracture surfaces (a) in air and (b) in hydrogen at different crack lengths show apparent striations. The observation areas were indicated in Fig. 4.2. Striation spacing is approximately constant; it is about 0.65 μm in air and 0.4 μm in hydrogen.

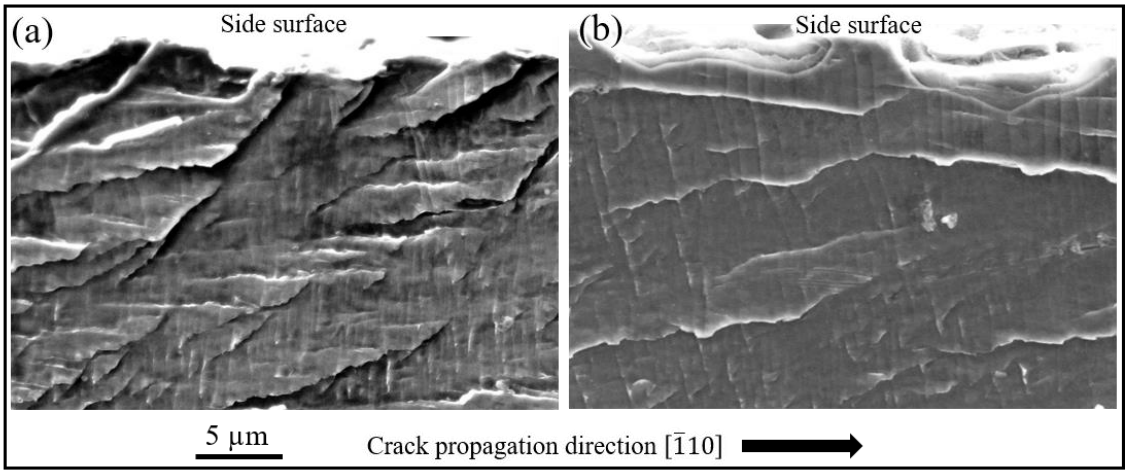

Fig. 4.4 High-magnification SEM images of the regions near the side surfaces of fracture surfaces (a) in air (specimen 2, Chapter 3) and (b) in hydrogen (specimen 1, Chapter 2). The striation spacing observed near the side surface and in the center of the fracture surface in air seems identical (about 0.65). However, in hydrogen, it is quite different when it is observed near the side surface (about 0.7 - 1 μm) and in the center of the fracture surface (about 0.4 μm).

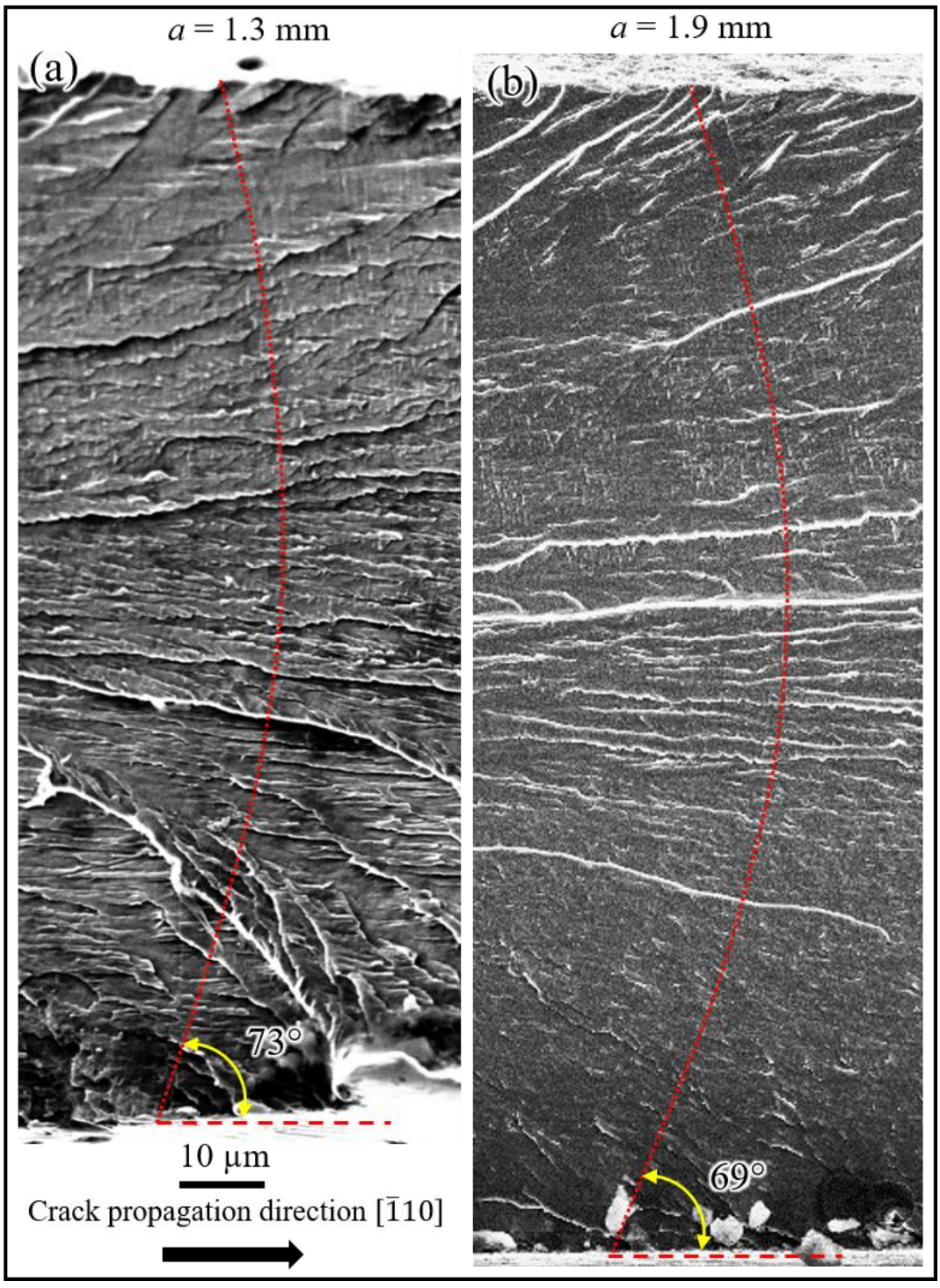

Fig. 4.5 SEM images showing crack front shape during propagation in (a) in air (specimen 2) and (b) in hydrogen (specimen 1)

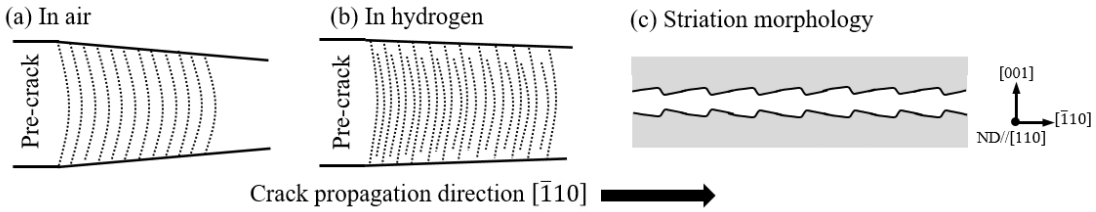

Fig. 4.6 Schematics showing characteristics of striation patterns on the fracture surfaces (a) in air, (b) in hydrogen, and (c) the striation morphology as presented in [52].

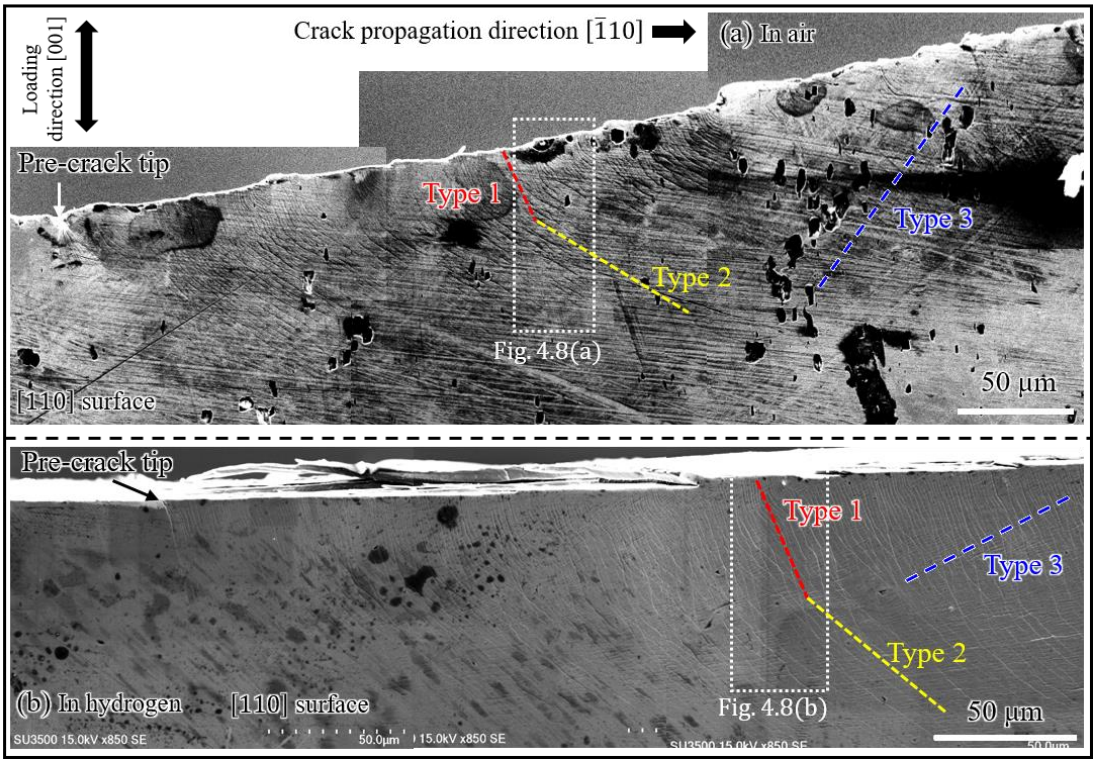

Fig. 4.7 SEM images of the specimen surfaces showing the slip lines (a) in air (specimen 2) and (b) in hydrogen (specimen 1). Each color of lines represents one type of slip traces.

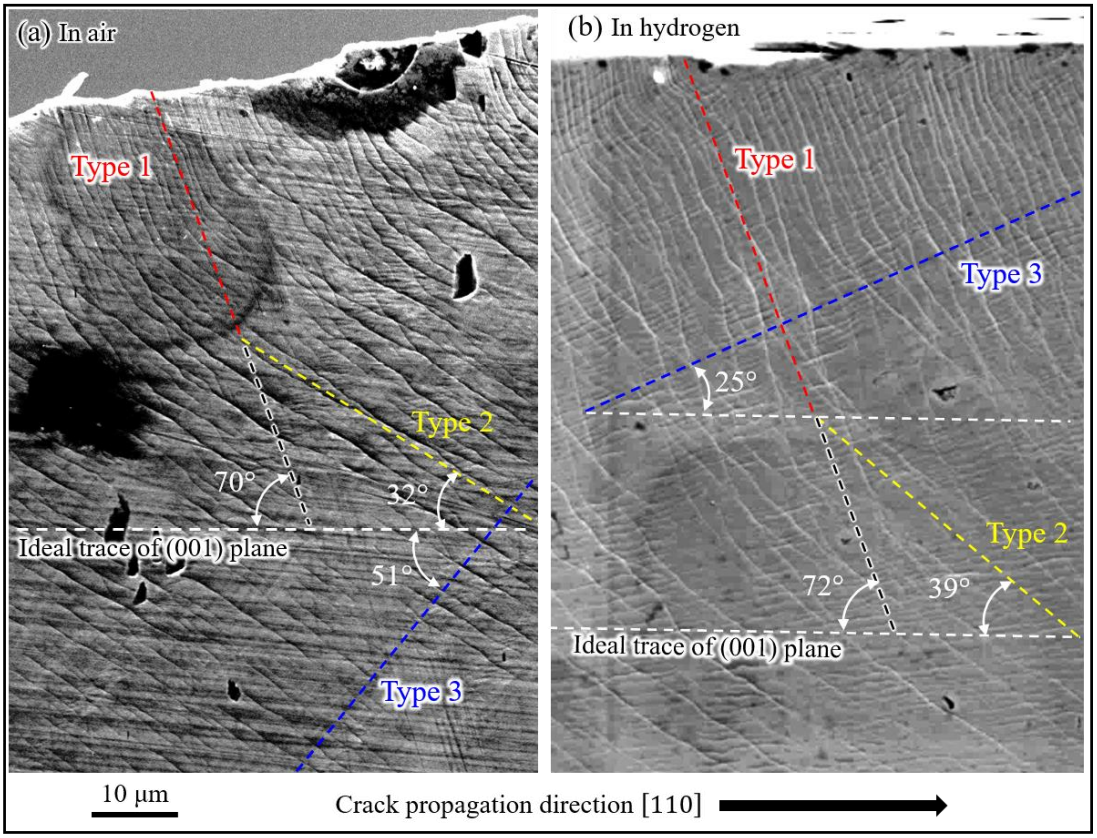

Fig. 4.8 Complementary SEM images of the specimen surfaces showing the clear slip lines (a) in air and (b) in hydrogen. These images are taken in the regions outlined in Fig. 4.7. Each color of lines represents one type of slip traces, which are the same as those of Fig. 4.7.

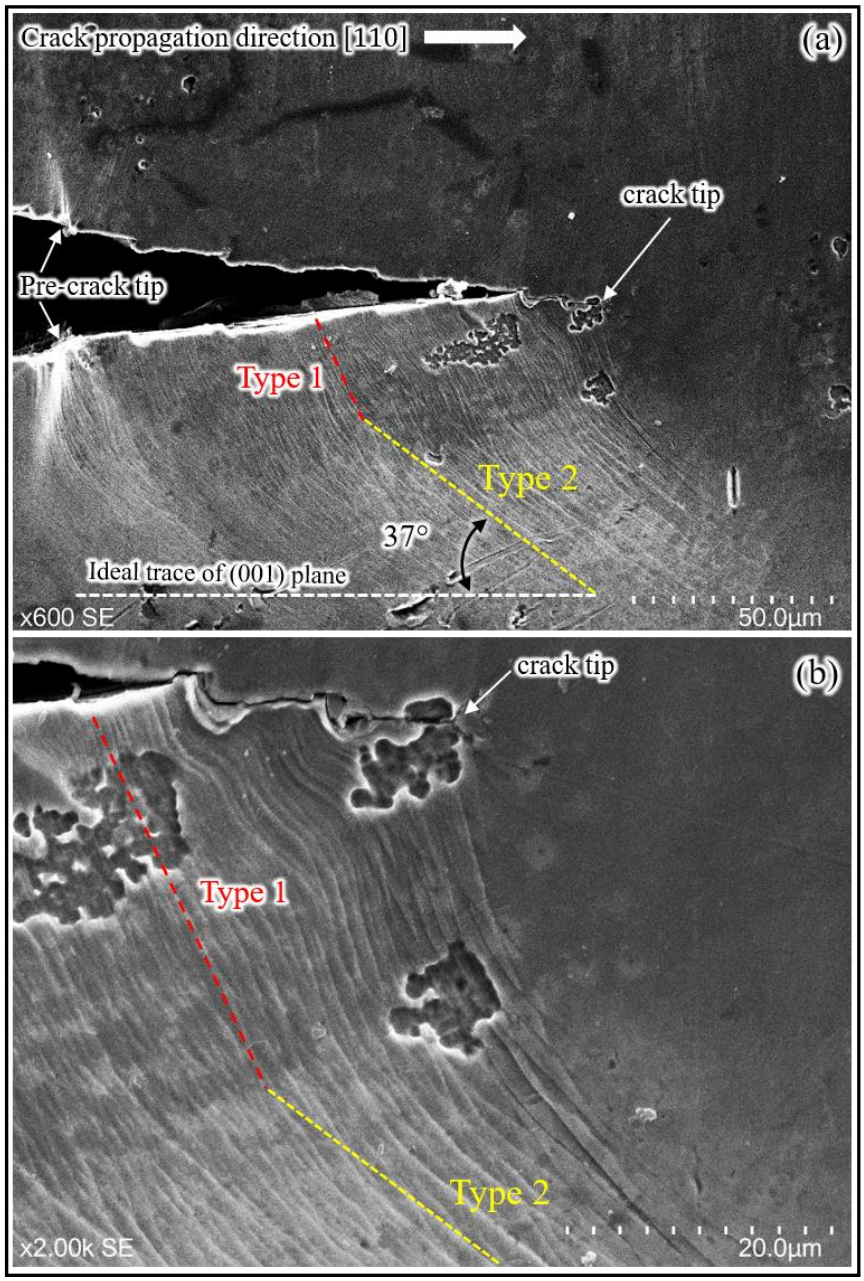

Fig. 4.9 SEM image of the specimen surfaces showing the clear slip lines of a specimen interrupted load at the crack length of a = 0.95 mm and unload (specimen 3). Each color of lines represents one type of slip traces, which are the same as those of Fig. 4.7. The specimen has slight buckling, which affects the electron reflection. This results in that the slip traces cannot be seen on the upper side of the crack.

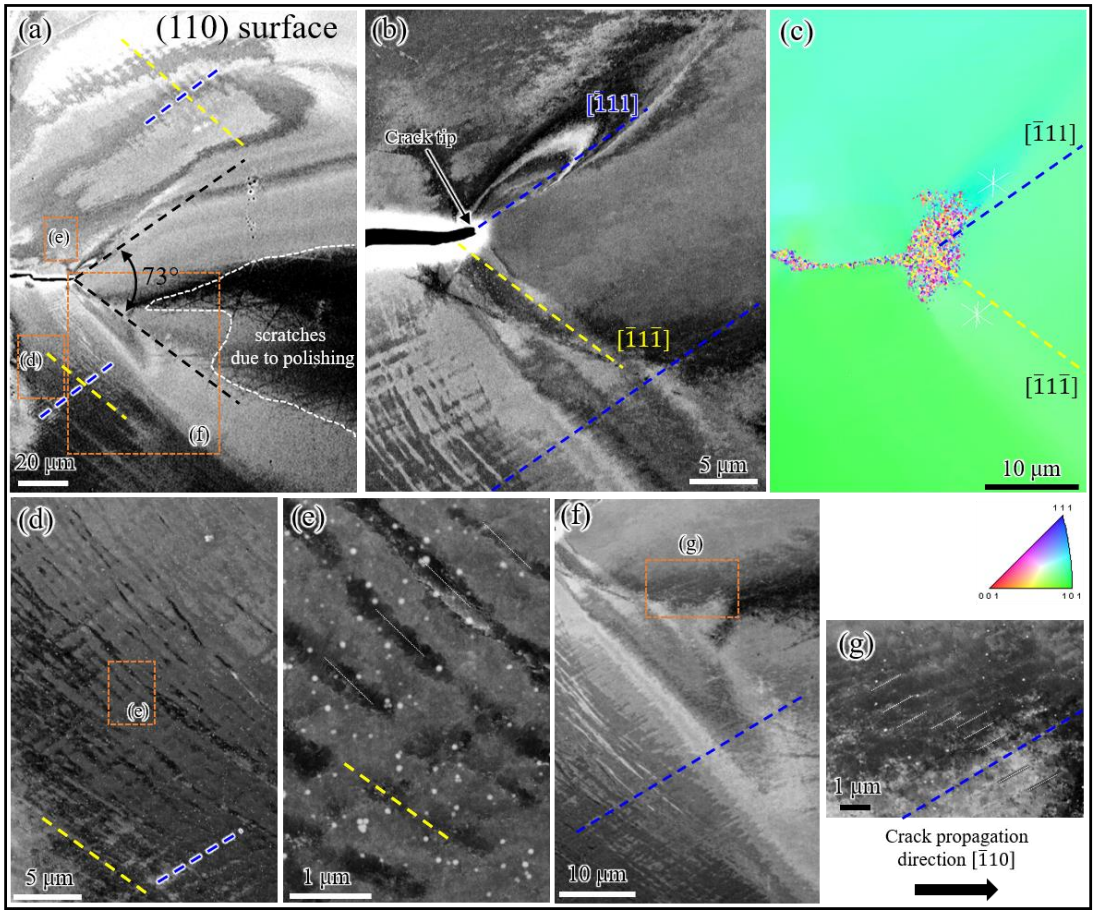

Fig. 4.10 A set of ECC images and EBSD analysis of the cross-sectioned surface after removing about 60 um of material from the side surface of specimen 3. In these images, except (c), are ECC images showing dislocation structure inside of the specimen. In the areas above (but far away) and below the crack plane shown in (a), the appearance of "crossing lines" of dislocation structures can be seen. The "crossing lines" are showed apparently in (d). It seems that the intersection between slip bands, which are in $[\bar{1}11]$ and $[\bar{1}1\bar{1}]$ directions.

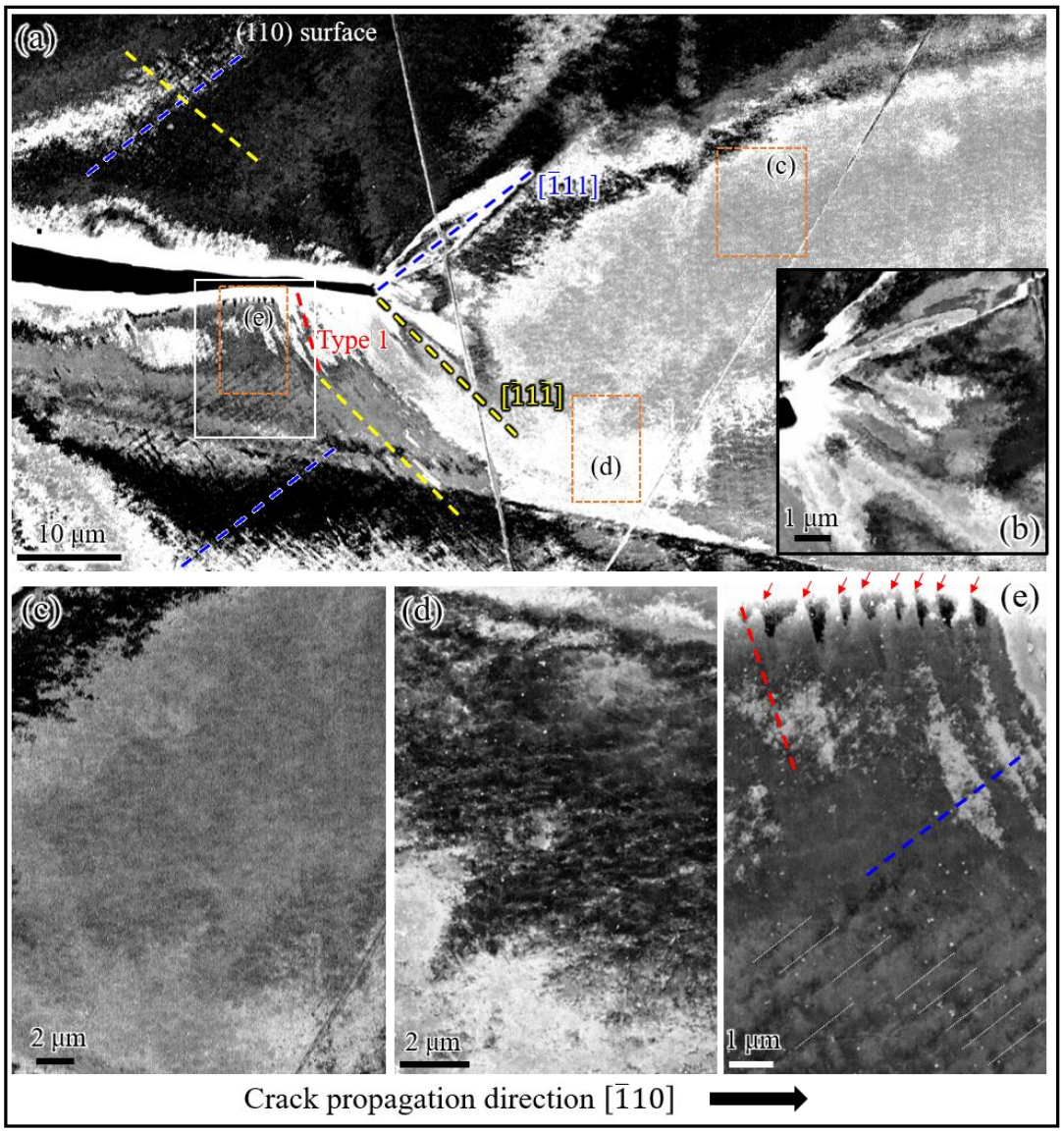

Fig. 4.11 ECC images showing dislocation structure in the same areas of Fig. 4.9 after further removing (around 30 μm) material in the thickness direction. Each color represents one type of slip directions. The average spacing between bands (red-broken line) and (blue-broken line) in a solid-white box in (a) is 0.57 μm and 0.61 μm. The "crossing lines" are showed apparently in (a). It seems that the intersection between slip bands, which are in [$\bar{1}$11] and [$\bar{1}1\bar{1}$] directions, as mentioned in Fig. 4.10.

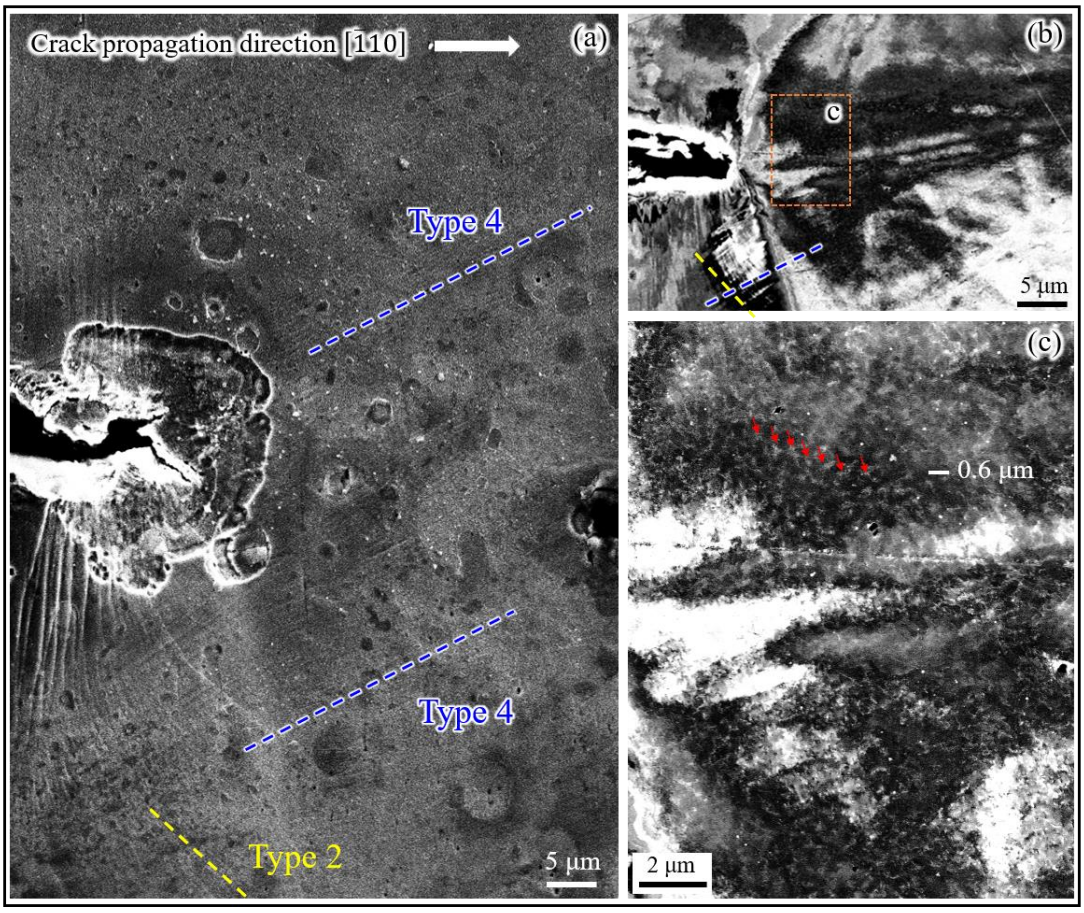

Fig. 4.12 SEM and ECC images showing slip traces on the side surface and corresponding dislocation structure inside of the specimen (near the middle of the specimen thickness) of specimen 4. The liquid that when applying the replica method (during introducing the fatigue pre-crack) or the humidity may cause some corrosion at the crack tip, as shown in (a).

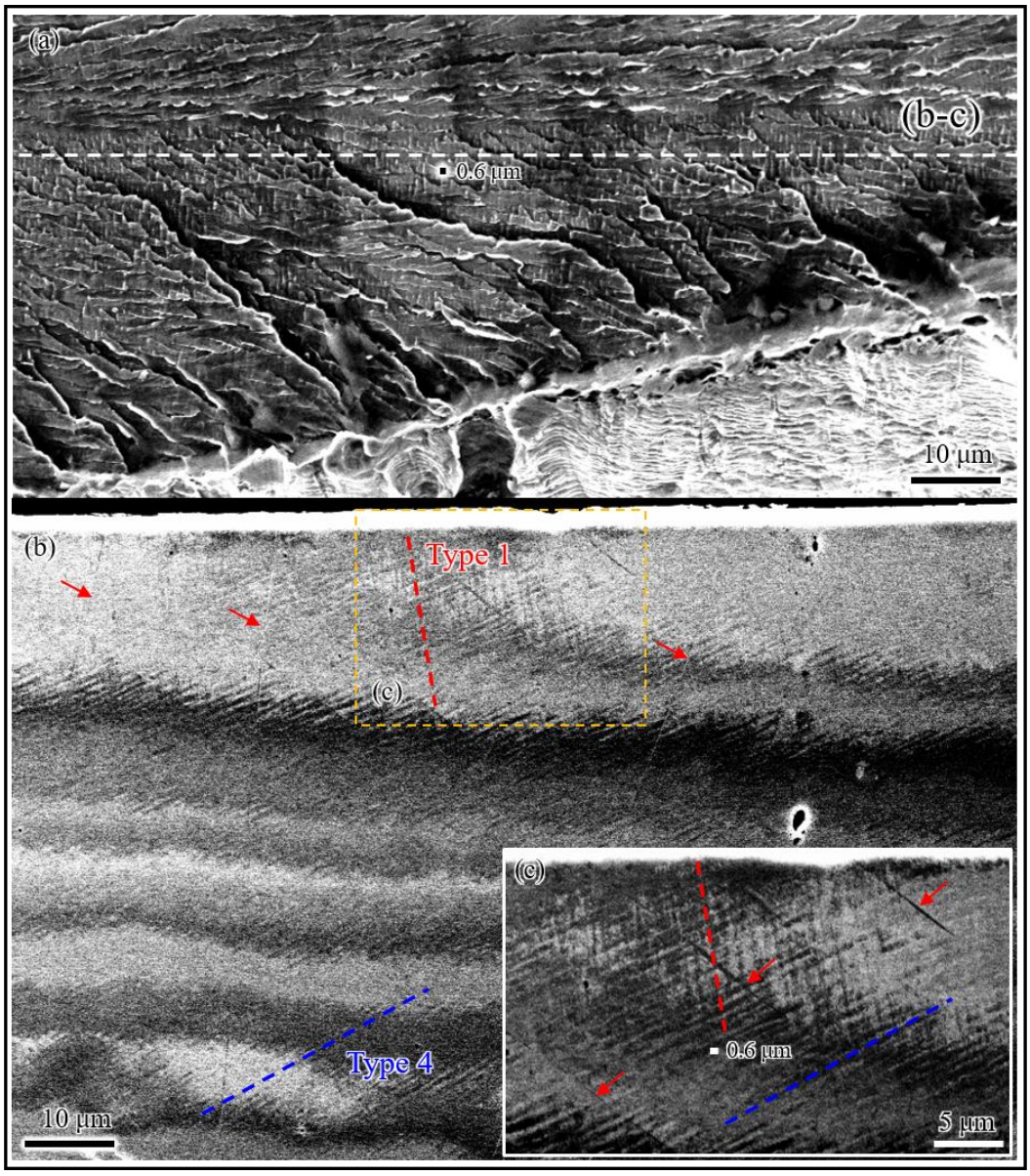

Fig. 4.13 (a) SEM image of the fracture surface taken at a = 1.4 mm on the left-hand side of the notch of specimen 2, the broken line indicates the locations of the cross-sectional ECC images in (b) and (c). ECC images showing dislocation structure inside of the specimen; these ECC images are the same as ECC images shown in Figs. 3.13(b) and (c) of Chapter 3. The average spacing between bands (Type 4) in (c) is about 0.72 μm.

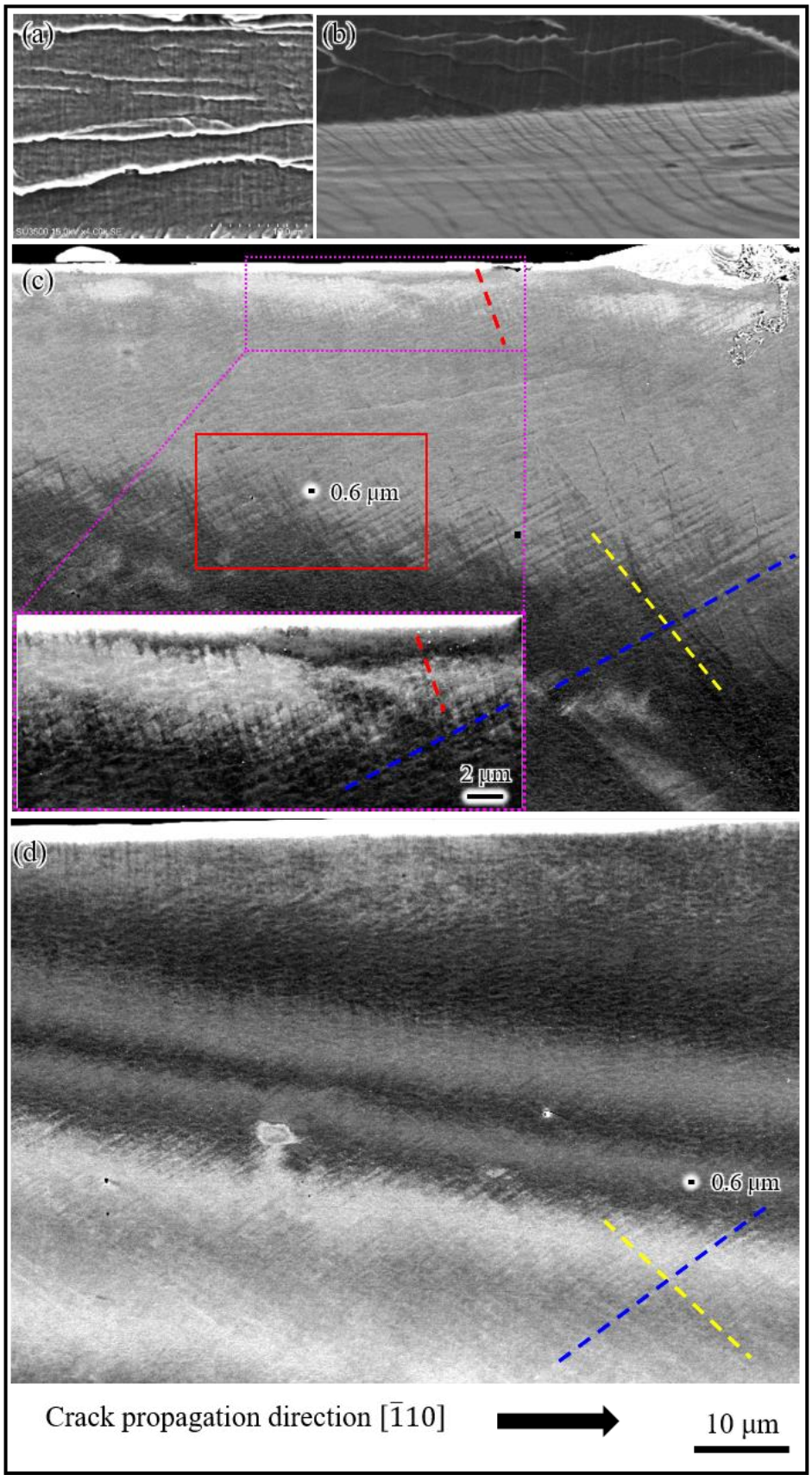
(a)
(b)
(c)
0.6 μm
2 μm
(d)
0.6 μm
Crack propagation direction [$\bar{1}$10]
10 μm

Fig. 4.14 (a) SEM images showing striations (a) in the center part and (b) near the side surface of the fracture surfaces (taken at a = 1.75 mm on the left-hand side of the notch of specimen 1). The striation spacing in the middle of the thickness is about 0.4 um, while it is about 0.6-0.8 um near the side surfaces; Dislocation structures near the side surface and in the middle of the specimen thickness are shown by ECC images in (c) and (d), respectively. These ECC images are the same as ECC images shown in Figs. 2.3(b) and (d) of Chapter 2. The average spacing between bands (red-broken line) in an enlarged image of (c) is 0.66 μm. The average spacing between bands (blue-broken line) in the red box in (c) is 0.71 μm.

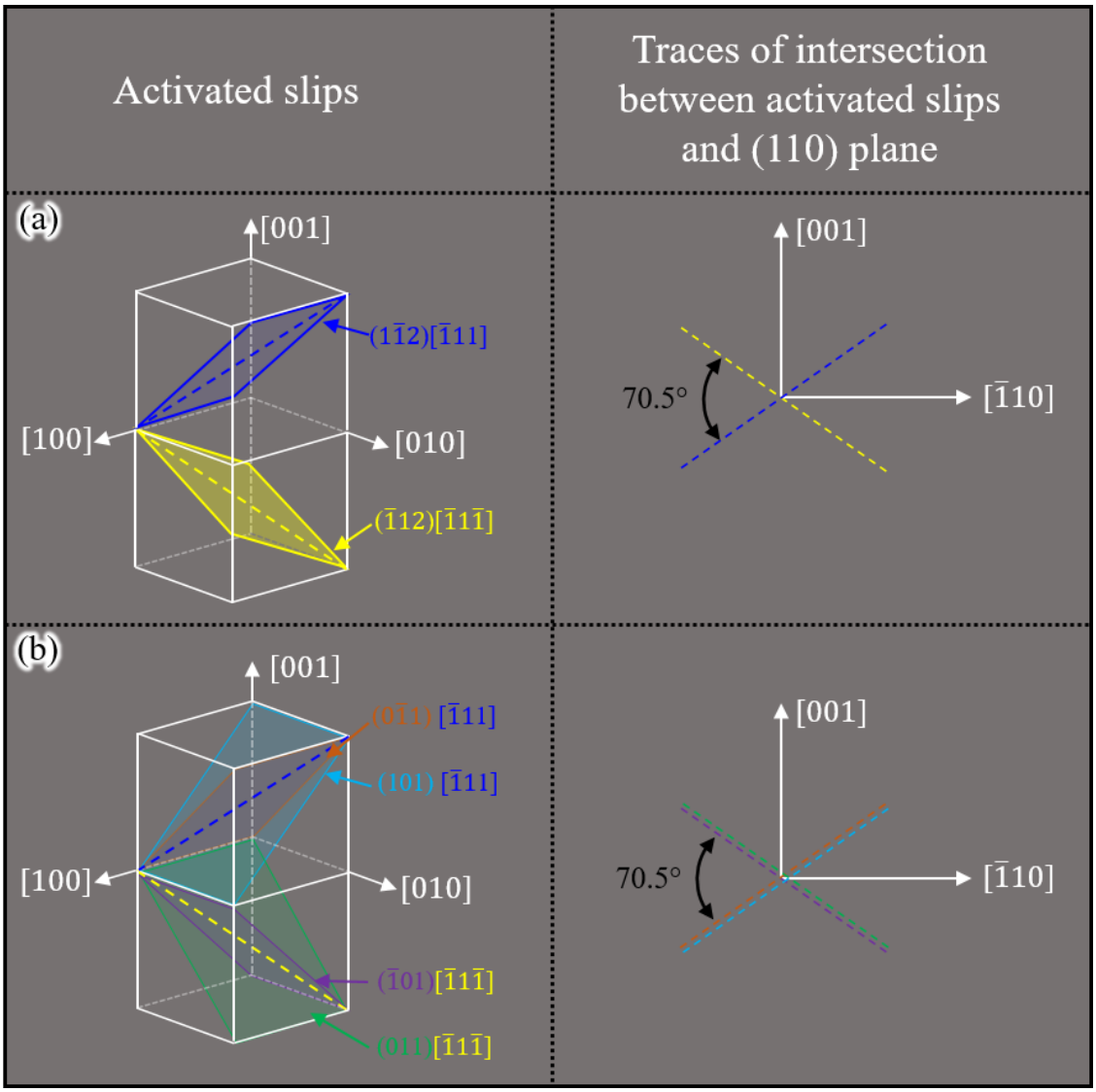

Fig. 4.15 A schematic illustration of the (a) (112)[111] and (b) (110)[111] slip systems which correspond to the slip traces associated with a (001)[$\bar{1}$10] (crack plane and crack propagation direction) crack propagation under plane strain conditions. Note that the same color indicates identical slip planes and directions.

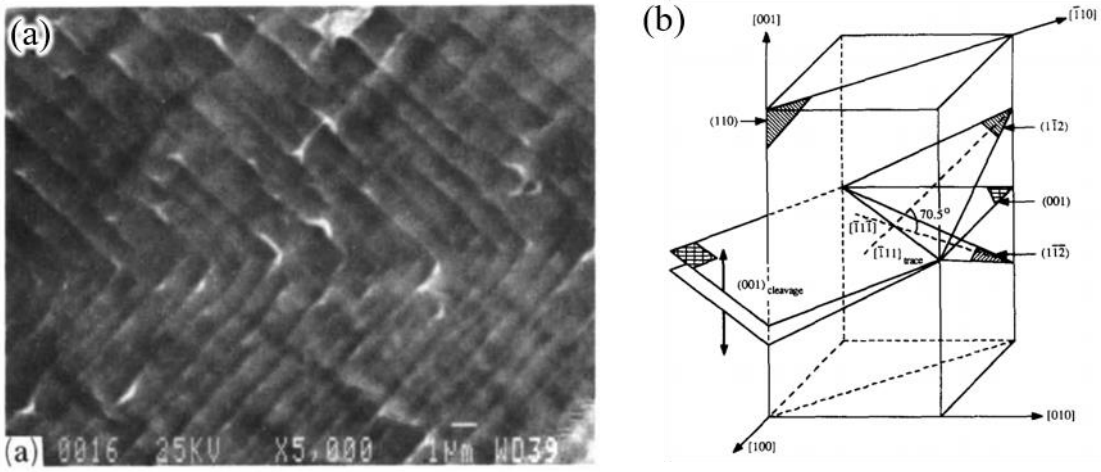

Fig. 4.16 (a) SEM image the fracture surface show striations. Crack propagated in [010] direction; however, its propagation direction localized in [$\bar{1}$10] direction; (b) {112}⟨111⟩ slip systems associated plane strain crack growth. These images were presented by Gerberich et al. [117].

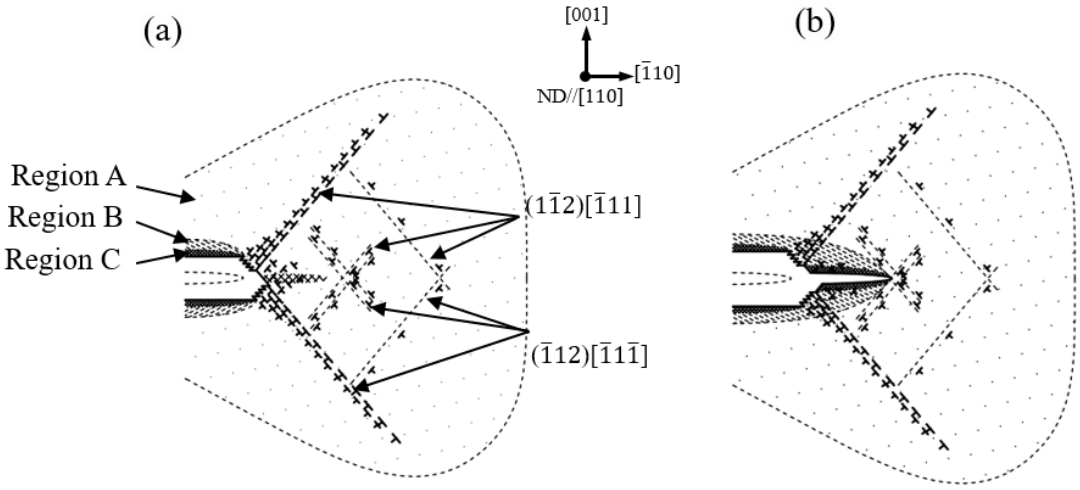

Fig. 4.17 A schematic illustrating mechanism of discontinuous crack propagation in air; (a) sub-crack initiation process; slip bands or cells formation ahead of the crack tip; (b) crack propagation by coalescence of sub-crack and main crack, and the crack propagation is then stopped by the intersection of crack and slip band/cell wall. Regions A, B, and C were mentioned in Chapters 2 and 3.

CHAPTER 5. Conclusions

5.1 Concluding remarks

The effects of hydrogen on macroscopic and microscopic features of crack propagation are investigated using a thin sheet of Fe-Si alloy. Single-crystalline Fe-Si alloy was selected to conduct the tests due to single crystals play a major role that presents a clearer picture of a material's intrinsic properties and has free boundary effects. The center-cracked specimens are tested under a sustained load in a hydrogen environment while under continuous stretching in an air environment. A comparison between these features is made to elucidate the role of hydrogen on the hydrogen-induced delayed crack propagation. The results reveal essential aspects of HE during the crack propagation in the present material. Particularly,

1. Considerable necking was observed in the present thin specimen; however, the necking (out-of-plane shear deformation) has no significant effect on the in-plane shear deformation. Hence, in-plane shear deformation in a thin specimen is the same as that in thick specimens, which results in the same crack growth mode in thin and thick specimens.
2. The crack propagation accompanies extensive plasticity. Surprisingly, the sequence of the crack propagation is similar in both air and hydrogen and presented as the following three stages: (1) crack tip blunting by dislocation emission from the crack tip; (2) damage (voids/shear cracks) initiation ahead of the crack tip; (3) sub-crack initiation and opening process. Hence, it is

suggested that the microscopic mechanism of hydrogen-induced delayed crack propagation in the present crystal orientation and material is the same as ductile crack propagation (the crack propagation tests are conducted in the air environment, in which the crack propagation is associated with micro-void initiation, growth, and coalescence ahead of the crack tip).

3. The similarity was observed in the deformation microstructures beneath the fracture surface. Both microstructures were composed of three distinct layers characterized by plastic strain gradients and dislocation densities. However, the characteristics of plastic strain and strain gradient in these regions are different; three layers were significantly affected by the environments. AIDE [94] model is postulated to be the main mechanism of crack propagation in a hydrogen environment. Moreover, HELP [22, 113] mechanism is speculated that it affects the reverse plastic strain in unloading regions.
4. During the crack propagation, hydrogen diffuses to and accumulates at the maximum stress field ahead of the crack tip to facilitated damage initiation. Stress-driven diffusion and dislocation transport are the main factors that contribute to accelerating the diffusion speed of hydrogen. On the other hand, hydrogen existed in the second peak of hydrostatic stress is postulated that it is the primary source of hydrogen, which contributes to accelerating hydrogen accumulation in the first peak.
5. The reverse plastic deformation occurs in the regions behind the fracture surface during the crack propagation. This contributes to not only enlarge CTOA but also slightly blunt the crack tip, which contributes to increasing crack growth resistance.

6. Discontinuous crack propagation is mainly caused by the interaction of the crack and $(1\bar{1}2)[\bar{1}11]$ and $(\bar{1}12)[\bar{1}1\bar{1}]$ slip bands/cell walls formed ahead of the crack tip. Work hardening occurs within slip bands/cell walls; crack tip plastic deformation hence becomes difficult. As a result, the crack propagation will stop, and the external load has to increase further to propagate the crack. This can be proposed as one of the possible mechanisms to explain that ductile crack growth creates a rising crack-growth resistance curve.
7. Hydrogen is speculated that it affects slip behavior, in which it induces a shorter spacing between slip bands ahead of the crack tip.

5.2 Future work

The spacing between slip bands in the present study is constant despite the crack-tip plastic strain increase. A reasonable explanation for this problem has not been figured out. Hydrogen is one of the factors that affect the spacing between slip bands. However, further studies need to be performed to figure out the other factors.

Single-crystalline materials are anisotropic material. The material properties, such as material strength, toughness depend on crystallographic orientation. HE sensitivity of the present material is also crystallographic orientation dependence. As presented by Takahashi et al. [53], they have conducted delayed crack growth tests using the same material; however, the loading direction and crack growth direction are $[1\bar{1}0]$ and $[001]$. The delayed crack propagation did not occur. Hence, it is necessary to investigate the HE resistance of this crystallographic orientation. It is helpful for

material researchers to study and manufacture materials that have a high resistance to HE.

HE is a new concept in Vietnam. Further studying HE sensitivity of metallic materials can contribute to developing The Vietnam Society of Mechanical Engineering, as well as teaching mechanical engineering students.

References

[1] P. Blanchard, A. Troiano, Embrittlement of metals by hydrogen. Influence of the crystallographic and electronic structure, Mem. Sci. Rev. Met. 57 (1960).

[2] R. Gest, A. Troiano, Stress corrosion and hydrogen embrittlement in an aluminum alloy, Corrosion 30(8) (1974) 274-279.

[3] G.C. Kennedy, Evidence of hydrogen embrittlement of tungsten carbide, American Institute of Physics Volume 49 Issue 2 (1978) 263.

[4] H.G. Nelson, D.P. Williams, J.E. Stein, Environmental hydrogen embrittlement of an α-β titanium alloy: effect of microstructure, Metallurgical and Materials Transactions B 3(2) (1972) 473-479.

[5] R.E. Buxbaum, A.B. Kinney, Hydrogen transport through tubular membranes of palladium-coated tantalum and niobium, Industrial & Engineering Chemistry Research 35(2) (1996) 530-537.

[6] H. Yukawa, T. Nambu, Y. Matsumoto, N. Watanabe, G. Zhang, M. Morinaga, Alloy design of Nb-based hydrogen permeable membrane with strong resistance to hydrogen embrittlement, Materials transactions (2008) 0806230453-0806230453.

[7] R. Latanision, H. Opperhauser, The intergranular embrittlement of nickel by hydrogen: the effect of grain boundary segregation, Metallurgical Transactions 5(2) (1974) 483-492.

[8] H. Birnbaum, H. Wadley, Hydrogen embrittlement of molybdenum, Scripta metallurgica 9(10) (1975) 1113-1116.

[9] F. Yunchang, D. Koss, The influence of multiaxial states of stress on the hydrogen embrittlement of zirconium alloy sheet, Metallurgical Transactions A 16(4) (1985) 675-681.

[10] C. Beevers, G. Newman, Hydrogen embrittlement in uranium, Journal of Nuclear Materials 23(1) (1967) 10-18.

[11] L.B. Pfeil, The effect of occluded hydrogen on the tensile strength of iron, Proceedings of the Royal Society of London. Series A, Containing Papers of a Mathematical and Physical Character 112(760) (1926) 182-195.

[12] A.R. Troiano, The role of hydrogen and other interstitials in the mechanical behavior of metals, trans. ASM 52 (1960) 54-80.

[13] R. Oriani, A mechanistic theory of hydrogen embrittlement of steels, Berichte der Bunsengesellschaft für physikalische Chemie 76(8) (1972) 848-857.

[14] R.P. Gangloff, Hydrogen assisted cracking of high strength alloys, Aluminum Co of America Alcoa Center Pa Alcoa Technical Center, 2003.

[15] R. Gangloff, Diffusion control of hydrogen environment embrittlement in high strength alloys, Hydrogen effects on material behavior and corrosion deformation interactions (2003) 477-497.

[16] W. Gerberich, S. Chen, Environment-induced cracking of metals, fundamental processes: micromechanics, Environment-Induced Cracking of Metals, eds. RP Gangloff, MB Ives (Houston, TX: NACE, 1990) (1990) 167.

[17] W. Gerberich, P. Marsh, J. Hoehn, Hydrogen induced cracking mechanisms-are there critical experiments?, Proceedings of the 1994 5th International Conference on the Effect of Hydrogen on the Behavior of Materials, Minerals, Metals & Materials Soc (TMS), 1996, pp. 539-551.

[18] C. McMahon Jr, Hydrogen-induced intergranular fracture of steels, Engineering Fracture Mechanics 68(6) (2001) 773-788.

[19] S. Lynch, Mechanisms of hydrogen assisted cracking-a review, Hydrogen effects on material behaviour and corrosion deformation interactions (2003) 449-466.

[20] C. Beachem, A new model for hydrogen-assisted cracking (hydrogen "embrittlement"), Metallurgical and Materials Transactions B 3(2) (1972) 441-455.

[21] H.K. Birnbaum, P. Sofronis, Hydrogen-enhanced localized plasticity—a mechanism for hydrogen-related fracture, Materials Science and Engineering: A 176(1-2) (1994) 191-202.

[22] P. Sofronis, Y. Liang, N. Aravas, Hydrogen induced shear localization of the plastic flow in metals and alloys, European Journal of Mechanics-A/Solids 20(6) (2001) 857-872.

[23] I. Robertson, The effect of hydrogen on dislocation dynamics, Engineering fracture mechanics 68(6) (2001) 671-692.

[24] S. Lynch, L. SP, Mechanisms of hydrogen-assisted cracking, ISSN 0160-7952 Vol 2 (1979) 189-200.

[25] S. Lynch, Environmentally assisted cracking: overview of evidence for an adsorption-induced localised-slip process, Acta Metallurgica 36(10) (1988) 2639-2661.

[26] S. Lynch, Metallographic contributions to understanding mechanisms of environmentally assisted cracking, Metallography 23(2) (1989) 147-171.

[27] S. Lynch, Comments on "A unified model of environment-assisted cracking", Scripta Materialia 61(3) (2009) 331-334.

[28] W.F. Hosford, Mechanical behavior of materials, Cambridge university press 2010.

[29] P.R. Dawson, D.E. Boyce, J.-S. Park, E. Wielewski, M.P. Miller, Determining the strengths of HCP slip systems using harmonic analyses of lattice strain distributions, Acta Materialia 144 (2018) 92-106.

[30] D. Curry, P. Pratt, The role of second phase particles in the ductile fracture of higher carbon steels, Materials Science and Engineering 37(3) (1979) 223-235.

[31] M. Shabrov, C. Briant, A. Needleman, S. Kim, E. Sylven, D. Sherman, L. Chuzhoy, Void nucleation by inclusion cracking, Metallurgical and Materials Transactions A 35(6) (2004) 1745-1755.

[32] A. Argon, J. Im, R. Safoglu, Cavity formation from inclusions in ductile fracture, Metallurgical transactions A 6(4) (1975) 825-837.

[33] F. Beremin, Cavity formation from inclusions in ductile fracture of A508 steel, Metallurgical Transactions A 12(5) (1981) 723-731.

[34] L. Brown, W. Stobbs, The work-hardening of copper-silica v. equilibrium plastic relaxation by secondary dislocations, Philosophical Magazine 34(3) (1976) 351-372.

[35] S. Goods, L. Brown, Overview No. 1: The nucleation of cavities by plastic deformation, Acta metallurgica 27(1) (1979) 1-15.

[36] T.L. Anderson, Fracture mechanics-fundamentals and applications, NASA STI/Recon Technical Report A 92 (1991).

[37] R. McMeeking, D. Parks, On criteria for J-dominance of crack-tip fields in large-scale yielding, Elastic-plastic fracture, ASTM International 1979.

[38] H. Johnson, J. Morlet, A. Troiano, Hydrogen, crack initiation, and delayed failure in steel, Trans. Met. Soc. AIME 212 (1958) 57-262.

[39] A. Tetelman, W. Robertson, The mechanism of hydrogen embrittlement observed in iron-silicon single crystals, Trans. TMS-AIME 224 (1962) 775-783.

[40] J. Morlet, A new concept of hydrogen embrittlement in steel, Journal of the Iron and Steel Institute 189 (1958) 37-44.

[41] P. Doig, G. Jones, A model for the initiation of hydrogen embrittlement cracking at notches in gaseous hydrogen environments, Metallurgical Transactions A 8(12) (1977) 1993-1998.

[42] A.T. Yokobori Jr, T. Nemoto, K. Satoh, T. Yamada, Numerical analysis on hydrogen diffusion and concentration in solid with emission around the crack tip, Engineering Fracture Mechanics 55(1) (1996) 47-60.

[43] W.W. Gerberich, R. Oriani, M.-J. Lji, X. Chen, T. Foecke, The necessity of both plasticity and brittleness in the fracture thresholds of iron, Philosophical Magazine A 63(2) (1991) 363-376.

[44] E. Martínez-Pañeda, S. del Busto, C.F. Niordson, C. Betegón, Strain gradient plasticity modeling of hydrogen diffusion to the crack tip, international journal of hydrogen energy 41(24) (2016) 10265-10274.

[45] P. Sofronis, R.M. McMeeking, Numerical analysis of hydrogen transport near a blunting crack tip, Journal of the Mechanics and Physics of Solids 37(3) (1989) 317-350.

[46] S. Lynch, Hydrogen embrittlement and liquid-metal embrittlement in nickel single crystals, Scripta Metallurgica 13(11) (1979) 1051-1056.

[47] S. Roberts, A. Booth, P. Hirsch, Dislocation activity and brittle-ductile transitions in single crystals, Materials Science and Engineering: A 176(1-2) (1994) 91-98.

[48] F. Sorbello, P. Flewitt, G. Smith, A. Crocker, The role of deformation twins in brittle crack propagation in iron–silicon steel, Acta materialia 57(9) (2009) 2646-2656.

[49] T. Marrow, M. Aindow, P. Prangnell, M. Strangwood, J. Knott, Hydrogen-assisted stable crack growth in iron-3 wt% silicon steel, Acta materialia 44(8) (1996) 3125-3140.

[50] X. Chen, T. Foecke, M. Lii, Y. Katz, W. Gerberich, The role of stress state on hydrogen cracking in Fe-Si single crystals, Engineering Fracture Mechanics 35(6) (1990) 997-1017.

[51] X. Chen, W. Gerberich, The kinetics and micromechanics of hydrogen assisted cracking in Fe-3 pct Si single crystals, Metallurgical Transactions A 22(1) (1991) 59-70.

[52] Y. Takahashi, K. Yamaguchi, M. Tanaka, K. Higashida, H. Noguchi, On the micromechanism of hydrogen-assisted cracking in a single-crystalline iron–silicon alloy thin sheet, Scripta Materialia 64(6) (2011) 537-540.

[53] Y. Takahashi, M. Tanaka, K. Higashida, K. Yamaguchi, H. Noguchi, An intrinsic effect of hydrogen on cyclic slip deformation around a {1 1 0} fatigue crack in Fe–3.2 wt.% Si alloy, Acta Materialia 58(6) (2010) 1972-1981.

[54] Y. Takahashi, M. Tanaka, K. Higashida, H. Noguchi, Hydrogen-induced slip localization around a quasi-brittle fatigue crack observed by high-voltage electron microscopy, Scripta Materialia 61(2) (2009) 145-148.

[55] H. Gough, The behaviour of a single crystal of α-iron subjected to alternating torsional stresses, Proceedings of the Royal Society of London. Series A, Containing Papers of a Mathematical and Physical Character 118(780) (1928) 498-534.

[56] C. Barrett, G. Ansel, R. Mehl, Preferred Orientations in Iron-silicon Alloys, Trans. AIME 25 (1937) 516-530.

[57] B. Šesták, S. Libovický, Dislocations in plastically deformed Fe-3% Si alloy single crystals, Cechoslovackij fiziceskij zurnal B 12(2) (1962) 131-139.

[58] W.A. Henning, J. Mercer, Ductile Iron Handbook, Ed. AFS, Des Plaines, USA, American Foundrymen's Society 1992.

[59] W. Fairhurst, K. Rohrig, High-silicon nodular irons, Foundry Trade Journal 146(3159) (1979) 657-681.

[60] A. Kimura, H. Kimura, Hydrogen embrittlement in high purity iron single crystals, Materials Science and Engineering 77 (1986) 75-83.

[61] S. Hinotani, F. Terasaki, F. Nakasato, Fractographic approach to the hydrogen-embrittled fracture in iron and steels, Hydrogen in Metals (1979) 421-424.

[62] F. Nakasato, I. Bernstein, Crystallographic and fractographic studies of hydrogen-induced cracking in purified iron and iron-silicon alloys, Metallurgical Transactions A 9(9) (1978) 1317-1326.

[63] H. Vehoff, P. Neumann, Crack propagation and cleavage initiation in Fe-2.6%-Si single crystals under controlled plastic crack tip opening rate in various gaseous environments, Acta Metallurgica 28(3) (1980) 265-272.

[64] H. Vehoff, W. Rothe, P. Neumann, Hydrogen Assisted Crack Growth in High Purity Low Pressure Hydrogen Gas, Atomistics of Fracture, Springer 1983, pp. 829-834.

[65] H. Yamada, M. Tsurudome, N. Miura, K. Horikawa, N. Ogasawara, Ductility loss of 7075 aluminum alloys affected by interaction of hydrogen, fatigue deformation, and strain rate, Materials Science and Engineering: A 642 (2015) 194-203.

[66] H. Lü, M. Li, T. Zhang, W. Chu, Hydrogen-enhanced dislocation emission, motion and nucleation of hydrogen-induced cracking for steel, Science in China Series E: Technological Sciences 40(5) (1997) 530-538.

[67] X. Chen, J. Kozubowski, W.W. Gerberich, Hydrogen-induced sustained load cracking in single crystal Fe-3wt.% Si, Scripta metallurgica 22(2) (1988) 245-248.

[68] X. Chen, W.W. Gerberich, Evidence for 1μm size instabilities in hydrogen-assisted cracking of Fe3% Si crystals, Scripta metallurgica 22(9) (1988) 1499-1502.

[69] S. Chen, Y. Katz, W. Gerberich, Crack-tip strain fields and fracture microplasticity in hydrogen-induced cracking of Fe-3 wt% Si single crystals, Philosophical Magazine A 63(1) (1991) 131-155.

[70] T. Hajilou, Y. Deng, N. Kheradmand, A. Barnoush, Hydrogen enhanced cracking studies on Fe–3wt% Si single and bi-crystal microcantilevers, Philosophical Transactions of the Royal Society A: Mathematical, Physical and Engineering Sciences 375(2098) (2017) 20160410.

[71] W. Gerberich, Y. Chen, C.S. John, A short-time diffusion correlation for hydrogen-induced crack growth kinetics, Metallurgical Transactions A 6(8) (1975) 1485-1498.

[72] M.-J. Lii, X.-F. Chen, Y. Katz, W. Gerberich, Dislocation modeling and acoustic emission observation of alternating ductile/brittle events in Fe-3wt% Si crystals, Acta metallurgica et Materialia 38(12) (1990) 2435-2453.

[73] W. Gerberich, R. Oriani, M.-J. Lji, X. Chen, T. Foecke, The necessity of both plasticity and brittleness in the fracture thresholds of iron, Philosophical Magazine A 63(2) (1991) 363-376.

[74] W. Gerberich, H. Huang, W. Zielinski, P. Marsh, A dislocation shielding prediction of the toughness transition during cleavage of semibrittle crystals, Metallurgical Transactions A 24(3) (1993) 535-543.

[75] T. Neeraj, R. Srinivasan, J. Li, Hydrogen embrittlement of ferritic steels: observations on deformation microstructure, nanoscale dimples and failure by nanovoiding, Acta Materialia 60(13-14) (2012) 5160-5171.

[76] A. Spielmannova, M. Landa, A. Machova, P. Haušild, P. Lejček, Influence of crack orientation on the ductile–brittle behavior in Fe–3 wt.% Si single crystals, Materials Characterization 58(10) (2007) 892-900.

[77] J. Hutchinson, Plastic stress and strain fields at a crack tip, Journal of the Mechanics and Physics of Solids 16(5) (1968) 337-342.

[78] G.T. Hahn, A.R. Rosenfield, Local yielding and extension of a crack under plane stress, Acta Metallurgica 13(3) (1965) 293-306.

[79] M. Kamaya, Measurement of local plastic strain distribution of stainless steel by electron backscatter diffraction, Materials Characterization 60(2) (2009) 125-132.

[80] M. Kamaya, A.J. Wilkinson, J.M. Titchmarsh, Measurement of plastic strain of polycrystalline material by electron backscatter diffraction, Nuclear engineering and design 235(6) (2005) 713-725.

[81] M. Kamaya, A.J. Wilkinson, J.M. Titchmarsh, Quantification of plastic strain of stainless steel and nickel alloy by electron backscatter diffraction, Acta Materialia 54(2) (2006) 539-548.

[82] D.S. Dugdale, Yielding of steel sheets containing slits, Journal of the Mechanics and Physics of Solids 8(2) (1960) 100-104.

[83] S. Taketomi, R. Matsumoto, S. Matsumoto, N. Miyazaki, Hydrogen effect on dislocation emission from a crack tip in alpha iron, ICF12, Ottawa 2009.

[84] H. Huang, W. Gerberich, Crack-tip dislocation emission arrangements for equilibrium—II. Comparisons to analytical and computer simulation models, Acta metallurgica et materialia 40(11) (1992) 2873-2881.

[85] F. Terasaki, T. Kawakami, A. Yoshikawa, N. Takano, Mechanism of crack propagation due to hydrogen embrittlement in iron single crystals stressed along [001] axis, Revue de Métallurgie 95(12) (1998) 1519-1529.

[86] M. Nagumo, Hydrogen related failure of steels–a new aspect, Materials Science and Technology 20(8) (2004) 940-950.

[87] R.B. Sills, B. Boyce, Void growth by dislocation adsorption, Materials Research Letters 8(3) (2020) 103-109.

[88] J. Hutchinson, P. Paris, Stability analysis of J-controlled crack growth, Elastic-plastic fracture, ASTM International 1979.

[89] T.L. Anderson, T.L. Anderson, Fracture mechanics: fundamentals and applications, CRC press2005.

[90] A. Varias, C. Shih, Quasi-static crack advance under a range of constraints—steady-state fields based on a characteristic length, Journal of the Mechanics and Physics of Solids 41(5) (1993) 835-861.

[91] J. Sobotka, R. Dodds Jr, Steady crack growth in a thin, ductile plate under small-scale yielding conditions: Three-dimensional modeling, Engineering Fracture Mechanics 78(2) (2011) 343-363.

[92] J. Tien, A.W. Thompson, I. Bernstein, R.J. Richards, Hydrogen transport by dislocations, Metallurgical Transactions A 7(6) (1976) 821-829.

[93] H. Kimura, H. Matsui, Mechanism of hydrogen-induced softening and hardening in iron, Scripta metallurgica 21(3) (1987) 319-324.

[94] S. Lynch, Mechanisms of environmentally assisted cracking in Al□ Zn□ Mg single crystals, Corrosion Science 22(10) (1982) 925-937.

[95] S. Taketomi, R. Matsumoto, N. Miyazaki, Atomistic study of the effect of hydrogen on dislocation emission from a mode II crack tip in alpha iron, International Journal of Mechanical Sciences 52(2) (2010) 334-338.

[96] P. Sofronis, H.K. Birnbaum, Mechanics of the hydrogen-dislocation-impurity interactions - I. Increasing shear modulus, Journal of the Mechanics and Physics of Solids 43(1) (1995) 49-90.

[97] P.J. Ferreira, I. Robertson, H. Birnbaum, Hydrogen effects on the interaction between dislocations, Acta materialia 46(5) (1998) 1749-1757.

[98] R. Oriani, P. Josephic, Equilibrium aspects of hydrogen-induced cracking of steels, Acta metallurgica 22(9) (1974) 1065-1074.

[99] T.T. Huynh, M. Koyama, Y. Takahashi, S. Hamada, K. Tsuzaki, H. Noguchi, Plastic deformation sequence and strain gradient characteristics of hydrogen-induced delayed crack propagation in single-crystalline Fe–Si alloy, Scripta Materialia 178 (2020) 99-103.

[100] P. Marsh, W.Z. Huang, W. Gerberich, crack-tip dislocation emission arrangements for equilibrium-iii. Application to large, Acta metall mater. Vol 40(11) (1992) 2883-2894.

[101] M. Landa, A. Machová, Z. Převorovský, J. Červ, J. Adámek, Crack growth in single crystals of α-iron (3 wt.% Si), Czechoslovak journal of physics 48(12) (1998) 1589-1606.

[102] J. Newman Jr, M. James, U. Zerbst, A review of the CTOA/CTOD fracture criterion, Engineering Fracture Mechanics 70(3-4) (2003) 371-385.

[103] D. Dawicke, M. Sutton, J. Newman, C. Bigelow, Measurement and analysis of critical CTOA for an aluminum alloy sheet, Fracture Mechanics: 25th Volume, ASTM International 1995.

[104] J. Newman, J. Crews, C. Bigelow, D. Dawicke, Variations of a global constraint factor in cracked bodies under tension and bending loads, Constraint Effects in Fracture Theory and Applicatons: Second Volume, ASTM International 1995.

[105] J. Newman Jr, D. Dawicke, C. Bigelow, Finite-element analyses and fracture simulation in thin-sheet aluminum alloy, International Workshop on Structural Integrity of Aging Airplanes; March 31, 1992.

[106] D. Dawicke, J. Newman, Residual strength predictions for multiple site damage cracking using a three-dimensional finite element analysis and a CTOA criterion, Fatigue and Fracture Mechanics: 29th Volume, ASTM International 1999.

[107] L. Lu, S. Wang, Relationship between crack growth resistance curves and critical CTOA, Engineering Fracture Mechanics 173 (2017) 146-156.

[108] L. Lu, S. Wang, A simple model to explain transferability of crack tip opening angle, Engineering Fracture Mechanics 193 (2018) 197-213.

[109] J.R. Rice, Tensile crack tip fields in elastic-ideally plastic crystals, Mechanics of Materials 6(4) (1987) 317-335.

[110] K.J. Juul, K.L. Nielsen, C.F. Niordson, Steady-state crack growth in single crystals under Mode I loading, Journal of the Mechanics and Physics of Solids 101 (2017) 209-222.

[111] S. Lynch, Hydrogen embrittlement phenomena and mechanisms, Corrosion Reviews 30(3-4) (2012) 105-123.

[112] H.-J. Kim, H.-Y. Jung, T.-W. Kwon, Y.-D. Chung, Effect of Plastic Deformation on Hydrogen Diffusion Behavior of Martensitic Steel in Hydrogen Absorption Environment, Materials transactions 60(8) (2019) 1614-1623.

[113] H. Birnbaum, Hydrogen effects on deformation--relation between dislocation behavior and the macroscopic stress-strain behavior, Scripta Metallurgica et Materialia;(United States) 31(2) (1994).

[114] X. Chen, W. Gerberich, Evidence for 1μm size instabilities in hydrogen-assisted cracking of Fe3% Si crystals, Scripta metallurgica 22(9) (1988) 1499-1502.

[115] X. Chen, J. Kozubowski, W. Gerberich, Hydrogen-induced sustained load cracking in single crystal Fe-3wt.% Si, Scripta metallurgica 22(2) (1988) 245-248.

[116] F. Cleri, S. Yip, D. Wolf, S.R. Phillpot, Atomic-scale mechanism of crack-tip plasticity: dislocation nucleation and crack-tip shielding, Physical Review Letters 79(7) (1997) 1309.

[117] M. Lii, T. Foecke, X. Chen, W. Zielinski, W. Gerberich, The effect of low energy dislocation structures on crack growth onset in brittle crystals, Materials Science and Engineering: A 113 (1989) 327-338.

[118] A. Tetelman, W. Robertson, Direct observation and analysis of crack propagation in iron-3% silicon single crystals, Acta Metallurgica 11(5) (1963) 415-426.

[119] D. Kuhlmann-Wilsdorf, Energy minimization of dislocations in low-energy dislocation structures, Physica status solidi (a) 104(1) (1987) 121-144.

[120] D. Kuhlmann-Wilsdorf, LEDS: Properties and effects of low energy dislocation structures, Materials Science and Engineering 86 (1987) 53-66.

[121] E. Lunarska, Hydrogen-induced cracking of plastically twisted iron, Scripta Metallurgica 15(10) (1981) 1149-1152.

[122] E. Lunarska, V. Novak, N. Zarubova, S. Kadeckova, Effect of electrolytic hydrogen charging on flow stress and slip line pattern in iron single crystals, Scripta Metallurgica 17(6) (1983) 705-710.

Acknowledgment

First and foremost, I wish to express my gratitude to my supervisor Professor Hiroshi Noguchi, for his unconditional support and constant backing. He gave me opportunity to study in Solid Mechanics Laboratory, Department of Hydrogen Energy System, Kyushu University, Japan. He taught me how to study and think, and motivated me to overcome difficulties of research. I learned from him not only knowledge but also the teaching method.

I also appreciate the valuable advice from Professor Hiroyuki Toda, Professor Masaki Tanaka, and Associate Professor Shigeru Hamada for my Ph.D. thesis. Also, I am very grateful to Associate Professor Shigeru Hamada for his help and discussion of the experiments, as well as his comments during writing papers. I am also honored to receive guidance from Associate Professor Motomichi Koyama. Additionally, I would like to express many thanks to Professor Kaneaki Tsuzaki from Research Center for Structural Materials, National Institute for Materials Science, 1-2-1 Sengen, Tsukuba 305-0047, Japan, and Professor Yoshimasa Takahashi from Department of Mechanical Engineering, Kansai University for giving me comments about my papers. I also want to extend my thanks to Mrs. Masako Kadota, secretary of our lab, for the care and help.

Besides, I would especially thank my family for their encouragement, support, and understanding. I would like to sincerely thank my friends in the Solid Mechanics Laboratory for discussion and support. Finally, I acknowledge the financial support from the Can Tho University Improvement Project VN14-P6, supported by a Japanese ODA loan during the period of my Ph.D. study.

Huynh Thanh Thuong

Japan, August 2020